β-Detected NMR of ^{8}Li$^+$ in Spintronic Materials

by

Qun Song

B.Sc., Tianjin University, 2004
M.Sc., The University of British Columbia, 2006

A THESIS SUBMITTED IN PARTIAL FULFILLMENT OF
THE REQUIREMENTS FOR THE DEGREE OF

DOCTOR OF PHILOSOPHY

in

The Faculty of Graduate Studies

(Physics)

THE UNIVERSITY OF BRITISH COLUMBIA

(Vancouver)

November 2012

Abstract

β–detected Nuclear Magnetic Resonance (β-NMR) employs radioactive ^{8}Li$^+$ which is optically spin-polarized, as a local probe to study magnetism in materials via β decay. In this thesis, β-NMR is applied to spintronic materials, including GaAs, Ga$_{1-x}$Mn$_x$Asand Fe/GaAs heterostructures in a depth-controlled manner at TRIUMF.

High resolution β-NMR measurements were carried out on GaAs crystals (semi-insulating (SI-GaAs) and heavily doped n-type (n-GaAs)) as a control experiment for β-NMR on Fe/GaAs heterostructures. A small resonance shift was observed and found to be dependent on depth, temperature and doping. The depth dependence is only observed in SI-GaAs and not in n-GaAs. The resonance shift below 150 K in both GaAs is ~ 100 ppm, on the same order of some Knight shifts of ^{8}Li$^+$ in noble metals.

Ga$_{1-x}$Mn$_x$As is the first β-NMR study on a ferromagnetic material through the ferromagnetic transition. Both spin lattice relaxation (SLR) and resonance of ^{8}Li$^+$ were measured. Two resonances were clearly resolved from the nonmagnetic GaAs substrate and the magnetic Ga$_{1-x}$Mn$_x$As film. The latter one negatively shifts and is linearly proportional to the applied field. The hyperfine coupling constant A_{HF} of ^{8}Li$^+$ in Ga$_{1-x}$Mn$_x$As is found to be negative. The SLR rate λ does not follow Korringa's Law and its amplitude shows a weak temperature dependence through T_{C}. The behaviors of A_{HF} and λ suggest that the delocalized holes originate from a Mn derived impurity band. No evidence of magnetic phase separation is found.

^{8}Li$^+$ provides a new depth-dependent local probe to detect injected spin polarization. We measured the ^{8}Li$^+$ resonance in Fe/GaAs heterostructures with semi-insulating and heavily doped n-type substrates, with and without injected current. With zero current, no spin polarization at thermal equi-

Abstract

librium is found. A new current injection system was designed and setup to conduct current injection from the thin Fe layer into the n-GaAs substrate. We found effects of local Joule heating and a very small stray field caused by the injected current but no convincing evidence of injected spin polarization.

Preface

In this thesis, most of the results in Chapter 4 and some of the results in Chapter 3 have been published in journal articles and conference proceedings in which I am listed as first author. The co-authors either helped with data collection or provided the sample. The papers are listed chronologically as follows:

- Q. Song, K.H. Chow, R.I. Miller, I. Fan, M.D. Hossain, R.F. Kiefl, S.R. Kreitzman, C.D.P. Levy, T.J. Parolin, M.R. Pearson, Z. Salman, H. Saadaoui, M. Smadella, D. Wang, K.M. Yu, J.K. Furdyna and W.A. MacFarlane. Beta-detected NMR study of the local magnetic field in epitaxial GaAs:Mn. *Physica B 404:892, 2009*; which has a version of Section 4.3. I carried out all the data analysis. I drafted the manuscript, prepared and presented the associated poster on the 11th μSR International Conference (Tsukuba, Japan, 2008).

- Q. Song, K.H. Chow, Z. Salman, H. Saadaoui, M.D. Hossain, R.F. Kiefl, G.D. Morris, C.D.P. Levy, M.R. Pearson, T.J. Parolin, I. Fan, T.A. Keeler, M. Smadella, D. Wang, K.M. Yu, X. Liu, J.K. Furdyna and W.A. MacFarlane. beta-detected NMR of Li in $Ga_{1-x}Mn_xAs$. *Phys. Rev. B 84:054414, 2011*; which contains my analysis and has a version of Section 4.4. I performed the data analysis, conducted the SQUID measurements and wrote the manuscript.

- Q. Song, K.H. Chow, R.I. Miller, I. Fan, M.D. Hossain, R.F. Kiefl, G.D. Morris, S.R. Kreitzman, C.D.P. Levy, T.J. Parolin, M.R. Pearson, Z. Salman, H. Saadaoui, M. Smadella, D. Wang, K.M. Yu, X. Liu, J.K. Furdyna and W.A. MacFarlane. β-Detected NMR Search

for Magnetic Phase Separation in Epitaxial GaAs:Mn. *Physics Proce-dia 30:174-177, 2012*; which has a version of Section 4.6. I assisted in the additional data collection, and wrote the manuscript.

- Q. Song, K.H. Chow, M.D. Hossain, R.F. Kiefl, G.D. Morris, C.D.P. Levy, H. Saadaoui, M. Smadella, D. Wang, B. Kardasz, B. Heinrich and W.A. MacFarlane. β-detected NMR Study of Semi-Insulating GaAs. *Physics Procedia 30:227-230, 2012*; which has a version of Section 3.3. I carried out most of data collection, sample characterization, performed data analysis and wrote the manuscript. I also prepared the associated poster for the 12th μSR International Conference (Cancun, Mexico, 2011).

The respective publishers grant permission for this material to be incorporated into this thesis.

The $Ga_{1-x}Mn_xAs$ sample measured in Chapter 4 was provided and characterized by X. Liu and J.K. Furdyna from the University of Notre Dame. The GaAs crystals used in Chapter 3 were provided by B. Kardasz in B. Heinrich's lab at Simon Fraser University (SFU). The Fe/GaAs samples used in Chapter 5 were epitaxially grown by B. Kardasz in B. Heinrich's lab at SFU. I designed the contact pattens on the Fe/n-GaAs sample. The gold contacts on both sides of the Fe/n-GaAs sample were thermally evaporated by me to conduct current injection experiment presented in Chapter 5. The sample holder for the thermal evaporator was designed by me and made by P. Dosanjh at AMPEL.

In order to carry out the current injection experiment, I designed the system allowing the application of electrical current to a sample during a β-NMR run. The SolidWorks model was initially built by me and later revised by D. Eldridge. I tested the current injection system in liquid Nitrogen and set it up in the β-NMR spectrometer with the help of R. Abasalti.

For the data shown in Chapter 5, I did most of the data collection, and performed all of the analysis.

Table of Contents

List of Tables

List of Figures

List of Acronyms

AMPEL Advanced Materials and Process Engineering Laboratory, the Brimacombe Building at UBC

CCD Charge-coupled device

CW Continuous Wave

DMS Dilute Magnetic Semiconductor

DOS Density of States

EFG Electric Field Gradient

FE Field Emission

FM Ferromagnetic/Ferromagnetism

FWHM Full Width Half Maximum

GMR Giant magnetoresistance

IB Impurity Band

ISAC Isotope Separator and Accelerator Facility, at TRIUMF

MBE Molecular Beam Epitaxial

ML Mono-Layer

NMR Nuclear Magnetic Resonance

PIXE Particle Induced X-ray Emission

ppm parts per million

RBS Rutherford Backscattering Spectrometry

RHEED Reflection High-Energy Electron Diffraction

rf radio frequency

RKKY stands for Ruderman-Kittel-Kasuya-Yosida. It refers to a coupling mechanism in metal between the nuclear magnetic moment to the spins of conduction electrons[1, 2, 3].

SC semiconductor

SFU Simon Fraser University

SI Semi-Insulating

SLR Spin Lattice Relaxation

SQUID Superconducting QUantum Interference Device, a sensitive magnetometer

SRIM Stopping and Range of Ions in Matter, a Monte Carlo code

TRIUMF Tri-University Meson Facility, Canada's national laboratory for nuclear and particle physics research and related sciences

TFE Temperature Field Emission

UHV Ultra High Vacuum

VB Valence Band

Acknowledgements

This thesis could not have been possible without the help of a great number of people. First and foremost, I would like to thank my co-supervisors: Prof. Andrew MacFarlane and Prof. Rob Kiefl for their overall guidance and patience. Their knowledge, expertise and challenge of the experimental and theoretical aspects of our work are crucial for the completion of this thesis, and their enthusiasm for physics have been inspirational and motivating. I would also like to thank other members in my committee: J. Brewer and M. Berciu for reading the thesis and their insightful comments.

This thesis has benefited a lot from the help and expertise of Gerald Morris for his design and continual improvement of the β-NMR facility at TRIUMF. Gerald taught me a lot about how to use β-NMR and about spin injection system designing. I would also like to thank Prof. Kim Chow for his dedication to the technique and interest in my projects. His advice was always very helpful.

I wish to thank my colleagues in β-NMR group: Terry Paronlin, Hassan Saadaoui, Masrur Hossein, Dong Wang, Oren Ofer, Mike Smadella, Todd Keeler, and others. I'm very grateful for you guys spending many nights taking data, and for the helpful discussions and good times we had together. Special thanks to Terry Paronlin, Hassan Saadaoui for teaching me the first lesson of β-NMR. Their encouragements never stopped even after they graduated. Many thanks to Dale Eldridge for improving the design of the spin injection system. I must acknowledge Sarah Dunsiger for her helpful discussions on $Ga_{1-x}Mn_xAs$. I would also like to acknowledge TRIUMF staffs for their great contributions to the β-NMR experiments: Rahim Abasalti, Phil Levy, M.R. Pearson, Donald Arseneau, Bassam Hitti, and Suzannah Daviel, as well as the ISAC II operators.

Chapter 1

Introduction

Electrons, the elementary constituents of electronic devices, not only have electrical charge but also carry an intrinsic angular momentum known as "spin". Ever since the discovery of transistors[4], electronics based on the precise manipulation of carrier charges to achieve information processing has been an exceptional success that has revolutionized everyday life, while the electron spin, although it has been known for most of the 20th century, has been generally ignored until the discovery of the giant magneto-resistance (GMR) effect in multilayered ferromagnetic metals in 1988[5, 6]. The new field of spin electronics, or "spintronics", explores the potential for new devices combining both charge and spin degrees of freedom of mobile electrons (Fig. 1.1). It is driven not only by commercial applications, such as low power data processing and storage, new device functionality and integrating magnetic memory and processing, but also by fundamental interest. Numerous conceptual spin-based transistors have been proposed[7, 8, 9, 10, 11], and spins in semiconductors are expected to play essential roles in quantum computation[12, 13]. These applications require fundamental research to understand the interactions between the electron spin and its solid-state environments, including polarization, transport and detection[14].

As a rapidly emerging field of science and technology, spintronics has shown a significant impact on the electronics. In order to develop spintronic technology, it is first necessary to fully explore potential spintronic materials, such as ferromagnetic semiconductors and heterostructures of ferromagnetic (FM) films on normal semiconductors. The spin polarization of carriers can be generated and detected optically or electronically[14]. Nuclear Magnetic Resonance (NMR), as a local probe, is also suitable to study the interactions of electronic spins within the materials. However, NMR
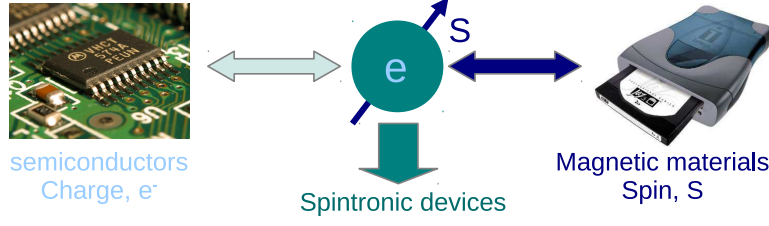
Figure 1.1: The combination of the complementary properties of electron charge and magnetic spin is required to create functional spintronic devices.

requires typically $\sim 10^{18}$ spins for resolvable signals, therefore its application to thin film materials is limited. In a β-detected NMR experiment, one implants spin-polarized radioactive ions into the material under study and monitors the nuclear magnetic resonance via anisotropic β decay. β-NMR could overcome the signal limitation problem and be used as a local probe to study the spin polarization in spintronic materials. The β-NMR technique is presented in Chapter 2. In this thesis, we focus on β-NMR studies on three potential candidate materials for spintronic application: the ferromagnetic semiconductor Mn doped GaAs (Chapter 4), GaAs crystals (Chapter 3), and Fe/GaAs heterostructures (Chapter 5).

As the concept will be important throughout this thesis, first let's discuss the difference between "Fermi energy E_F" and "chemical potential μ". Electrons follow the Fermi-Dirac distribution. Fermi energy E_F is defined as the energy of the topmost filled state at $T = 0$ K. E_F does not vary with temperature. The occupation probability $f(E)$ for a state at energy E is:

$$f(E) = \frac{1}{e^{(E-\mu)/k_B T} + 1} \tag{1.1}$$

where μ the chemical potential is the Gibbs free energy per particle[15] and is a function of temperature. At $T = 0$ K, $f(E)$ changes discontinuously from 1 to 0 at $E = \mu$, so the chemical potential is equal to the Fermi energy $\mu = E_F$. When $T \neq 0$ K, the chemical potential is determined by the total

number of electrons N:

$$N = \sum_i f(E_i) = \sum_i \frac{1}{\mathrm{e}^{(E_i - \mu)/\mathrm{k_B}T} + 1} \tag{1.2}$$

indicating the change in the free energy when one more particle is introduced into the system at finite temperature. When the temperature is much less than the Fermi temperature $T_F \equiv E_F/k_B$, $\mu \approx E_F$[16]. This is valid for metal because of its high E_F[15], resulting in a Fermi temperature on the order of 10^4 K. In semiconductors with wide band gap such as GaAs[15], $T \ll T_F$ is also valid, therefore $\mu \approx E_F$. In this thesis, we still use E_F at finite temperature in the discussion, but it is really the chemical potential μ that indicates where Eqn. (1.1) is 1/2.

1.1 Ferromagnetism

We first quickly review some fundamentals of ferromagnetism before we proceed. Quantum theory of magnetism has been rooted from two starting points: the localized model (localized electron states in real space) and the band model (localized electron states in momentum space)[16, 17]. The localized model mainly deals with magnetism in insulators and rare-earth metals, while the band model provides an insight understanding of ferromagnetism in transition metals[17].

In a strongly interacting system, the inter-atomic interactions come into play and result in the ferromagnetism. In the localized model, each electron remains localized on an atom. The main contribution of the atomic magnetic moment is from the spins of electrons in partially filled d or f bands. The exchange Hamiltonian describing the interaction of localized spins on different atoms is:

$$\mathcal{H} = -\sum_{ij} A_{ij} \mathbf{S}_i \cdot \mathbf{S}_j \tag{1.3}$$

where A_{ij} is the exchange integral, and $\mathbf{S}_i$ is the spin operator at the lattice site i. This is the well-known Heisenberg model (*direct-exchange* interaction), which arises from direct Coulomb interactions among the electrons of
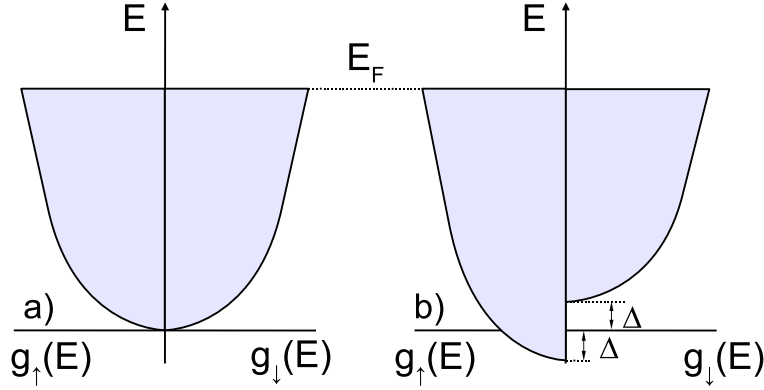
Figure 1.2: Left: Band diagrams of free electron band without exchange interaction. Right: The band splitting when the exchange interaction is in play. The energy splitting between spin-up and spin-down subbands is 2Δ. $g_{\uparrow\downarrow}(E)$ is the density of states for the spin up and down subbands. Adapted from Ref. [16].

any two magnetic ions. When A_{ij} is positive, spins tend to align parallel, and the material is ferromagnetic in the ground state. When A_{ij} is negative, $\mathbf{S}_i$ and $\mathbf{S}_j$ are anti-parallel in the ground state, and the material is antiferromagnetic.

Although the localized model works well for insulating magnetic materials and rare-earth metals, both quantitatively and qualitatively, it does not apply to transition metals: Fe, Co and Ni. Here the d electrons are not fully localized and the magnetic moment is not an integer multiple of the Bohr magneton (μ_B) as it is for magnetic ions. They are itinerant magnets and should be described using the band model.

In the band model, the carriers which carry the magnetism are itinerant. They move in the average field of the other electrons and ions, and the electron levels form energy bands. Inside one energy band, electrons with different spin polarization form two degenerate subbands (spin-up $\uparrow$ and spin-down $\downarrow$ subbands) when there's no exchange interaction. (Fig. 1.2 Left Panel). In the ground state at T=0 K, electrons, following the Fermi-Dirac distribution, fill energy bands up to the Fermi energy (E_F). As mentioned
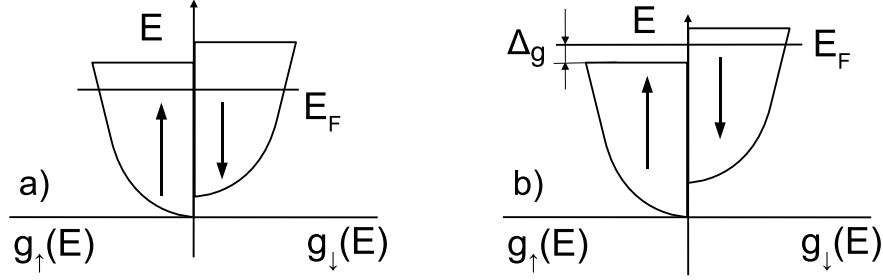
Figure 1.3: Left: E_{F} lies in both $\uparrow$ and $\downarrow$ subbands. Right: E_{F} lies in only $\downarrow$ subband.

above, d electrons are partially localized, and Heisenberg exchange interactions come into play and compete with the kinetic band energy. The electron transfer near the Fermi energy (E_{F}) from spin-down ($\downarrow$) subband to spin-up ($\uparrow$) subband induces an increase in band energy (ΔE_{Band}) and a decrease in the magnetic energy(ΔE_{Mag}). The magnetic order is achieved when the band energy increase is smaller than the magnetic energy loss ($\Delta E_{\mathrm{Band}} < \Delta E_{\mathrm{Mag}}$). The exchange interaction splits the degenerate subbands (Fig. 1.2 Right Panel). The unbalance of electron occupation between the spin-up ($\uparrow$) and spin-down ($\downarrow$) subbands gives rise to a net magnetization M, characterized by densities of up and down spins ($n_\uparrow \neq n_\downarrow$):

$$M = \mu_B(n_\uparrow - n_\downarrow) \tag{1.4}$$

The position of E_{F} results in different types of itinerant ferromagnetism. As shown in the left panel of Fig. 1.3, E_{F} lies in both $\uparrow$ and $\downarrow$ subbands – for instance the metal iron (Fe) (more discussion in Section 1.2.2). Electrons occupy both energy subbands. The polarization of electrons at E_{F} is not 100% parallel aligned in the ground state of Fe. In some cases, *e.g.* nickle (Ni), E_{F} falls in a single spin subband as shown in the right panel of Fig. 1.3. For $T = 0$ K, the spin-up subband is filled, and its density of states at E_{F} vanishes. The magnetic magnetization is $M = \mu_B n_\downarrow(E)$ with $n_\downarrow(E)$ is the density of state at energy E.

1.2 Ferromagnetic Ga$_{1-x}$Mn$_x$As and Fe

Discussion in Section 1.1 on the ferromagnetism provides us with a good start in understanding spintronic materials. This section will review some magnetic properties of the spintronic materials studied in this thesis.

Ferromagnetic semiconductors are attractive candidates, offering the opportunity to integrate information storage and processing into a single material. Some early discovered ferromagnetic semiconductors, such as EuO, exhibit ferromagnetism below a certain transition temperature T_C (Curie temperature), and have been well–studied in the 1960s and 1970s[18, 19]. One way to make a ferromagnetic semiconductor is to dope normal semiconductors (*e.g.* GaAs, GaN) with some magnetic ions, such as Mn^{2+}. The transition temperature can be varied by doping density and process conditions. We focus our attention on Ga$_{1-x}$Mn$_x$As, which will be introduced in Section 1.2.1. Another possibility to combine semiconductor with ferromagnetic materials is to grow ferromagnetic materials on conventional semiconductors, such as Fe/GaAs heterostructures. Fe thin films on GaAs substrates is favored in MBE growth because of their lattice match. The properties of the itinerant ferromagnet iron will be discussed in Section 1.2.2.

1.2.1 Dilute Magnetic Semiconductor: Ga$_{1-x}$Mn$_x$As

Ga$_{1-x}$Mn$_x$As is one of the most promising and the most extensively-studied ferromagnetic semiconductors. The magnetism in Mn doped GaAs was first discovered by H. Ohno in 1996[20]. The Curie temperature (T_C) has been greatly improved, from below liquid nitrogen temperature to above 200 K[21], and even to 250 K by using delta-doping techniques[22].

There are 3 Mn lattice locations in GaAs, which are crucial in determining the magnetic properties[24, 25, 26, 27, 28]. Divalent Mn^{2+} can occupy the Ga lattice sites (Mn$_{Ga}$), forming the Ga$_{1-x}$Mn$_x$As solid solution with concentrations x as high as several percent. Since one Mn^{2+} contributes only two electrons to the GaAs host instead of three by the original Ga^{3+}, one substitutional Mn^{2+} (Mn$_{Ga}$), as an acceptor, provides one free hole to mediate ferromagnetic interactions between Mn ions. Most Mn^{2+} ions take Mn$_{Ga}$

6
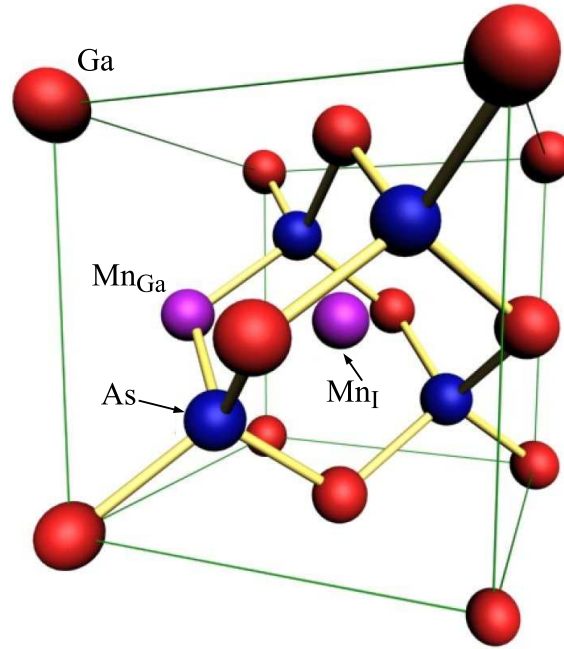
Figure 1.4: Divalent Mn^{2+} occupy the Ga lattice sites in GaAs. Such substitutional Mn (Mn_{Ga}) provides free holes to mediate ferromagnetic interactions between Mn^{2+} local moments. Mn residing in the interstitial sites (Mn_I) is a double electron donor that compensates the hole doping due to (Mn_{Ga}). Adapted from Ref. [23].
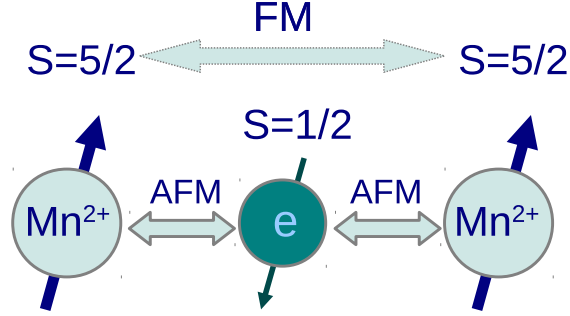
Figure 1.5: Schematic diagram of ferromagnetic coupling mechanism in $Ga_{1-x}Mn_xAs$ mediated by holes.

sites. In addition, a small fraction of Mn (20%) may reside at interstitial sites (Mn_I). Here the Mn_I are double electron donors which compensate the hole doping due to Mn_{Ga}. Furthermore, the moments of Mn_I tend to align antiferromagnetically with the Mn_{Ga} spins, reducing the total magnetic moment. Mn_I are metastable and can, upon annealing, precipitate out as Mn clusters or inclusions of the MnAs impurity phase (a ferromagnetic metallic compound). The MnAs impurity phase may segregate at the surface or interface[29, 30]. Such precipitates will contribute to the overall magnetization. The third site Mn_{Rand} is not a well-defined crystallographic site, but represents some distribution over disordered sites. They are not involved in the FM interactions. Fig. 1.4 shows the ideal zinc blende structure of GaAs with Mn atoms in the Ga substitutional position and interstitial position. Only a few percent of Mn may distribute randomly.

The relatively shallow Mn acceptors introduce holes which, in turn, mediate ferromagnetism among the spin 5/2 Mn^{2+} moments through the indirect exchange interaction as shown in Fig. 1.5. When a hole carrier aligns anti-parallel with two Mn^{2+} cation spins through anti-ferromagnetic coupling, it will cause the two Mn^{2+} spins to align parallel, which is equivalent to a ferromagnetic coupling between the two spin 5/2 magnetic moments. Macroscopic magnetic ordering is then introduced by the propagation of spin-polarized hole-carriers in the bulk semiconductor.

There are two fundamentally opposing theoretical viewpoints on the origin of the holes in $Ga_{1-x}Mn_xAs$[31]. First, electronic-structure calculations have argued that the ferromagnetism in $Ga_{1-x}Mn_xAs$ is driven by impurity-derived states (impurity band (IB) model)[32, 33]. In this picture, the wavefunctions of the carriers mediating ferromagnetism are localized and take on the character of the Mn-derived impurity band. Second, the mean-field Zener model takes into account the valence-band structure of zinc-blende semiconductors (valence band (VB) model)[24, 34], assuming that $Ga_{1-x}Mn_xAs$ is metallic and has a high carrier density p. It argues that the ferromagnetism is mediated by extended hole states and that the Fermi energy locates in the valence band. The Zener model was first proposed in 1950s to explain the ferromagnetism in the transition metals driven by the *indirect exchange* interaction between carriers and localized spins[35].With this model, the Curie temperature of $Ga_{1-x}Mn_xAs$ was predicted to be proportional to $xp^{1/3}$, which suggested that a strategy to synthesize high T_C materials would be to increase the hole-carrier density and the Mn dopant concentration[24].

In the limit of zero concentration (dilute limit), the Mn impurity states are localized and could not mediate ferromagnetism. In this limit, any delocalized holes would be described by the GaAs valence band picture. However, at much higher concentrations (percent level) relevant for the observed ferromagnetism, the Mn states broaden into a band of delocalized states. Within the impurity band model, it is these states that are the mediators of ferromagnetism. At even higher concentrations, this impurity band is expected to broaden further and merge with the valence band of GaAs. In this regime, one would expect that, again, the holes might be better described by the GaAs valence band, and the VB model of ferromagnetism should apply. The crossover concentration between these two limits is still a matter of debate and is complicated by factors such as the compensating effect of Mn interstitials that compensate the Mn_{Ga} hole doping.

The VB model has been proved successful in explaining many experimental trends observed in dilute magnetic semiconductors (DMS) like $Ga_{1-x}Mn_xAs$ such as the magnetic anisotropy and the dependence of Curie tempera-

ture on hole concentration[28]. Detailed models of this mechanism involve parametrization of the relevant hole states, *e.g.* the approximation of the GaAs valence band (valence band model)[36].

There is controversy over which is the appropriate picture for the highest magnetic transition temperature (T_C) compositions well into the metallic conduction regime[37, 38]. Optical [39, 40, 41, 42], transport[43, 44] and scanning tunneling microscopy[45] (STM) results favour the impurity band model. Rokhinson *et al.* attributed the observed negative magnetoresistance in $Ga_{1-x}Mn_xAs$ at low temperature and low magentic fields to weak localization which strongly suggests impurity band transport[43]. The atomic scale fluctuations in the local electronic density of states at the Fermi level mapped by atomic resolution STM showed features characteristic of the localized limit, that would be absent for more extended states deep in the valence band[45]. Recent channeling measurements on $Ga_{1-x}Mn_xAs$ with the Mn concentration ranging between 3% and 6.8% infer impurity-band-mediated ferromagnetism[46]. On the other hand, a variety of features are consistent with the valence band model[24, 25, 47, 48, 49].

There is also a debate whether this material is magnetically phase-separated. A Low Energy μSR (LE-μSR) experiment reported that parts of the sample remained in the paramagnetic state below T_C[50], which is also supported by the direct magnetization measurement[51]. On the other hand, a systematic study with LE-μSR strictly defines the asymmetry baseline and shows no sign of phase separation[52].

The origin of the holes mediating the ferromagnetism and the magnetic phase separation are problems under debate over a dozen years. Chapter 4 will deal with these two questions in detail.

Calculations predict that in the ferromagnetic ground state the hole magnetization is opposite to (and much weaker than) that of the Mn^{2+} local moments[28]. The delocalized holes play a crucial role in the formation of the magnetic ground state, however, little is known experimentally about their magnetization and its variation with temperature. As the material is intrinsically inhomogeneous, a local probe may also reveal any magnetic inhomogeneity, through broadening and structure of the resonance line, for

example, in the controversial proposal of magnetic phase separation[50, 51, 52]. Nuclear spin lattice relaxation yields information on the low frequency spin dynamics where correlations are expected to play an important role[53]. The β-NMR in $Ga_{1-x}Mn_x$As is presented in Chapter 4

The thermodynamic equilibrium solubility limit of Mn in GaAs is very low, while the required concentration of Mn for ferromagnetism to occur in GaAs is in the few atomic percent range, far beyond the solubility limit[54]. So the production of $Ga_{1-x}Mn_x$As at the high Mn concentrations necessary for ferromagnetism requires non-equilibrium growth in the form of thin films, and bulk samples are not available. Growing $Ga_{1-x}Mn_x$As thin films by molecular beam epitaxy (MBE) at low temperatures of 200-300 °C limits Mn diffusion and suppresses the formation of other phases. Post-growth annealing has proven to help remove intersitial Mn atoms therefore increase T_C[27].

Preliminary experiments injecting spins from $Ga_{1-x}Mn_x$As into GaAs using a spin-LED structure demonstrated reasonable spin-injection efficiencies[55]. The discovery of ferromagnetic $Ga_{1-x}Mn_x$As and the demonstration of spin injection suggests the feasibility of all-semiconductor spintronic circuits, where magnetic and non-magnetic semiconductors could co-exist to perform spintronic functions, analogous to the integrated circuits.

1.2.2 Itinerant Ferromagnetism: Fe

As discussed at the beginning of this section, one candidate to make use of the spin property is the heterostructure of ferromagnetic thin films on conventional semiconductors, such as thin Fe films on GaAs. It is expected that the spin polarization could be injected from the ferromagnetic Fe layer into semiconductor GaAs. Therefore it is useful to review the properties of the itinerant ferromagnet iron (Fe).

Iron is a common transition metal with the atomic number 26. It's also the most commonly-used ferromagnetic material. The electron configuration is [Ar] $3d^6 4s^2$, with 6 $3d$ electrons. The melting temperature ($T_{melting}$) is 1538 °C, and the magnetic ordering temperature (Curie temperature) T_C

is 1043 K (770 °C) which is much higher than the $Ga_{1-x}Mn_xAs$ discussed above. Iron is usually in the solid phase with the density 7.874 g/cm^3 at room temperature.

As an "unsaturated" itinerant ferromagnet, the $3d$ and $4s$ bands of iron are partially filled[56]. In the $4s$ band, a weaker exchange interaction causes an approximately equal distribution of spin-up and spin-down electrons. Therefore the itinerant s electrons are not responsible for the magnetism, but do contribute to the conductivity. On the other hand, the $3d$ electron wave function is more localized on each atom. The exchange interaction splits the spin-up and spin-down $3d$ bands leading to an unbalanced electron population and resulting in a net magnetic moment per atom. As shown in the left panel of Fig. 1.3, for $T = 0$ K, both spin $\uparrow$ and $\downarrow$ subbands are partially filled ($g_\uparrow(E_F) \neq 0$, $g_\downarrow(E_F) \neq 0$), therefore the magnetic moment per atom is not saturated for $H_o = 0$.

Above T_C, iron is paramagnetic, and its susceptibility follows the Curie-Weiss Law, as shown in the top panel of Fig. 1.6. Here the inverse of the susceptibility χ^{-1} is linearly proportional to the temperature. Iron orders ferromagnetically below T_C. As shown in the bottom panel of Fig. 1.6, the reduced magnetization M/M_o increases as the temperature decreases and follows a power law. For our experimental temperature range (300 K – 3 K), M is nearly constant for Fe.

The spin polarization of a ferromagnet P_{FM} is defined as the spin asymmetry in the density of states (DOS) at the Fermi level:

$$P_{FM} = \frac{g_\uparrow(E_F) - g_\downarrow(E_F)}{g_\uparrow(E_F) + g_\downarrow(E_F)} \qquad (1.5)$$

where $g_\uparrow (g_\downarrow)$ is the majority (minority) DOS, respectively. In bulk iron, the DOS at the Fermi level is dominated by the spin-split $3d$ band and a high P_{FM} is expected assuming simple parabolic bands. Since the electrons responsible for conduction processes are those close to the Fermi level, this means a current flowing through a ferromagnet is spin polarized with a polarization approximately P_{FM}. The polarization of the electron spin could be conserved and injected into normal semiconductors such as GaAs
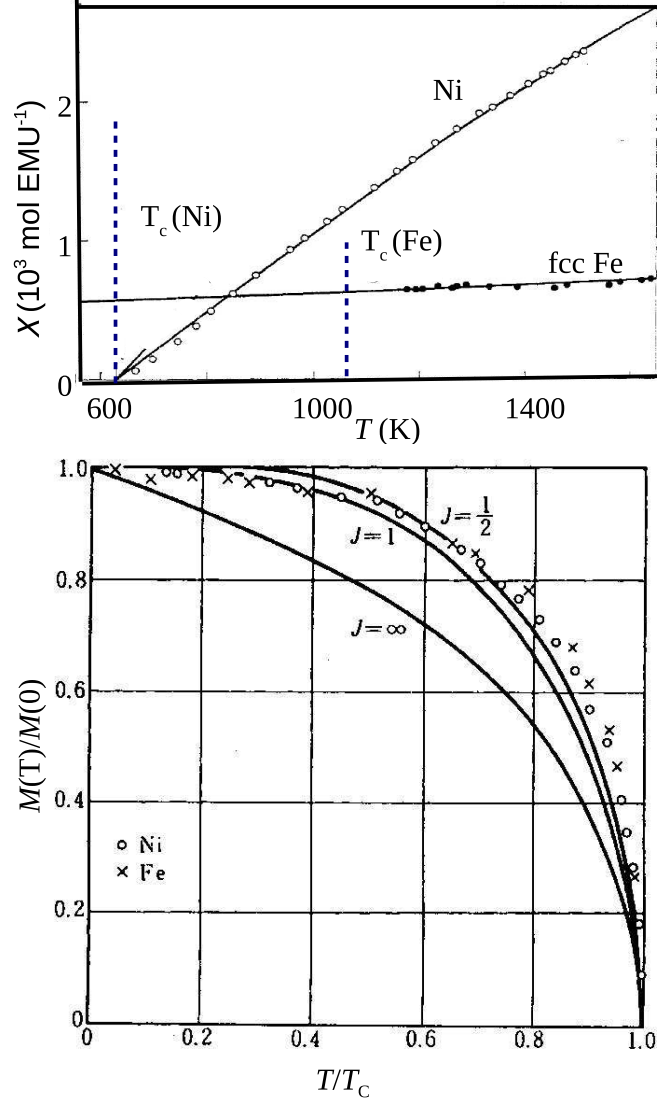
Figure 1.6: Fe Magnetization as a function of temperature above (top) and below (bottom) T_C. Top: the inverse of the molar susceptibility χ^{-1} as a function of temperature above T_C. Above T_C, iron is paramagnetic, and its susceptibility follows the Curie–Weiss Law, (adapted from Ref. [57]). Bottom: the reduced magnetization M/M_o as a function of the reduced temperature T/T_C. Fe is ferromagnetic below T_C, and its magnetization follows a critical power law as $T \rightarrow T_C$. Ni, a similar itinerant ferromagnet, is also shown in both panels, (adapted from Ref. [58]).

13

(Chapter 5).

An important distinction between Fe and $Ga_{1-x}Mn_xAs$ is that Fe is a good metal with a high carrier density. This has important consequences at the interface with a semiconductor which we describe in the next section.

1.3 Ferromagnetic Proximity Effect and Spin Injection

We have reviewed the properties of the ferromagnetic semiconductor $Ga_{1-x}Mn_xAs$ (Section 1.2.1) and itinerant ferromagnetic iron (Section 1.2.2). In order to make use of the spin degree of freedom and the mature (nonmagnetic) semiconductor technology, we expect that the ferromagnetism in a magnetic layer could be "transferred" into a conventional semiconductors, such as GaAs. The ferromagnetic proximity effect and spin injection are possible mechanisms which could achieve the goal. We'll briefly review the basics of ferromagnetic proximity effect and spin injection in this section and present our β-NMR study on the proximity effect of Fe/GaAs heterostructure in Chapter 5.

1.3.1 Schottky Barrier at the Fe/GaAs Interface

First we review the Schottky barrier at a metal/semiconductor interface which may have great influence on the production of spin polarization in the semiconductor.

The Schottky barrier is the intrinsic energy barrier which is formed at the interface of most metal/semiconductor junctions. When a metal layer is in contact with GaAs, the conduction band edge of GaAs bends up to make the chemical potentials are equal on both sides in thermal equilibrium. The conduction electrons of the semiconductor, which have higher energy, cross over into the metal and leave the positive ions behind, setting up a static electric field. In the GaAs region near the Fe, this electric field causes the GaAs to be depleted of mobile electrons. Fig. 1.7 shows a schematic energy band diagram of the Fe/GaAs junction for n-type GaAs relevant to the
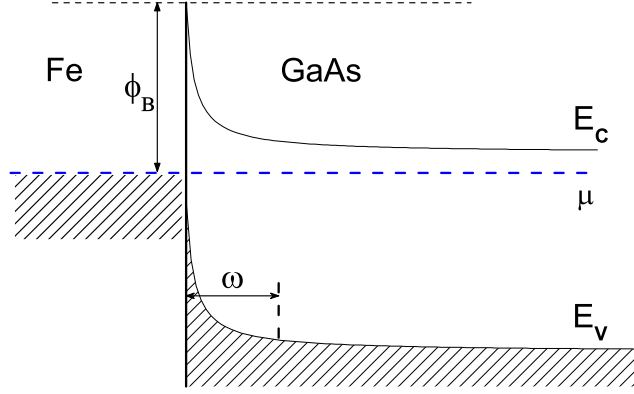
Figure 1.7: Diagram of the Schottky Barrier formed when Fe is in contact with n-type GaAs. The conduction band edge of the semiconductor bends up when the chemical potentials μ (Eqn. (1.1)) are equal on both sides (in thermal equilibrium). The conduction band electrons cross over into the metal and leave the positive ions behind, therefore the GaAs region near the Fe is depleted of mobile electrons. The Schottky barrier height ϕ_B and depletion width ω are shown.

study presented in Chapter 5.

In a simple model[16], the depletion width ω at a Schottky barrier can be estimated as

$$\omega = \sqrt{\frac{2\epsilon\epsilon_0\phi_B}{ne}}, \tag{1.6}$$

where e is the electron charge, ϵ is the static dielectric permittivity, ϕ_B is the height of the Schottky barrier and n is the carrier concentration. Take the heavily doped GaAs as an example. Assuming that in Fe/n-GaAs heterostructure, the Schottky barrier height $e\phi_B$ is ~0.72 eV (Ref. [59]), $\epsilon = 13.18$ for GaAs, and the carrier concentration of heavily doped n-GaAs is $n \sim 2 \times 10^{18}$ cm^{-3}, ω is ~ 23 nm.

Ever since the proposal of the spin dependent field effect transistor[7], the interest in spin injection from a ferromagnetic metal into semiconductors has been greatly intensified. The polarized spin can be sourced either from ferromagnetic semiconductors such as Mn doped GaAs[55, 60], or from ferromagnetic metals[61]. The first approach gives excellent results, but the

effort to obtain a magnetic semiconductor with a high Curie temperature T_C above room temperature is still ongoing. For the latter approach, the conductance mismatch between the ferromagnetic metal and the semiconductor prevents the direct injection from a low-resistivity magnetic metal[62], and the Schottky-barrier-induced electric field can cause strong spin relaxation, making spin injection almost negligible beyond the barrier region[63].

1.3.2 Ferromagnetic Proximity Effect

The *magnetic proximity effect* refers to the induction of magnetism by contact with a magnetic material. In the simplest case, a nonmagnetic material may be driven magnetic by contact with a ferromagnet. Early studies on metallic heterostructures[64, 65] found that the coherence length for induced magnetization was material dependent and generally small (tens of $\mathring{A}$), making detailed studies very difficult. This line of inquiry, in the context of multilayer systems, led to the discovery of the interlayer exchange coupling and giant magnetoresistance effects recently recognized with the 2007 Nobel Prize in Physics[5, 66]. Within the nonmagnetic metallic layer of such a heterostructure, the magnetic proximity effect induces an oscillating spin polarization in the conduction electrons.

Ultrafast optical pump-probe measurements reveal that the coherent electron spin dynamics in the n-type GaAs are strongly modified by the adjacent ferromagnetic (FM) layer[67], aligning along the ferromagnet's magnetization M. The dominant interaction is hyperfine coupling with nuclear spins in the GaAs[68, 69, 70], not fringe fields or direct exchange interactions with the ferromagnet. In the bulk semiconductor, polarized electron spins from the adjacent ferromagnet couple to nuclear spins through the hyperfine interaction. Nonequilibrium electron spins relax to equilibrium by transferring some of their angular momentum to the nuclear spins via the hyperfine interaction, and dynamically polarize the nuclear spins in the bulk semiconductor–"imprinting" the magnetization of the ferromagnetic layer on the nuclear spin in n-type GaAs. The lifetime of the induced spin polarization in a semiconductor is long and the spin polarization can be transported

over a long distance. A series of Time-resolved Faraday Rotation (TRFR) experiments[71, 72] show that in GaAs the spin polarization could persist as long as 0.1 μs, and is robust to transport over distances of $\sim 100\mu$m and across heterointerfaces.

Epstein *et al.* [73] found that photoexcited electrons in a *n*-GaAs layer could be rapidly spin-polarized due to the proximity of an epitaxial ferromagnetic metal, and that the GaAs nuclear spins are dynamically polarized with a sign determined by the spontaneous electron-spin orientation. In Fe/GaAs, the electron spin polarization is parallel with the magnetization M of the ferromagnet, and the spin-dependent density of states (DOS) near the Fermi level is larger for the majority spins than the minority spins. The electrons cause the dynamic polarization of nuclear spins and the sign of the nuclear-spin polarization depends on the electron-spin orientation rather than M. This effect demonstrates new control of both electron and nuclear spins in a semiconductor by carefully choosing ferromagnetic materials and manipulating the orientation of M.

1.3.3 Spin Injection

Spin injection, the intentional introduction of spin polarized carriers by a spin polarized electrical current, is one of the prerequisites for the realization of spintronic devices. For spintronics, it is thus particularly important to introduce spin polarized electrons into a *semiconductor* such as GaAs to take advantage of the long spin lifetime[72].

Spin injection has been done by optical excitation with polarized light[68] and by tunnelling from a ferromagnetic STM tip[74], but more recently there has been enormous effort to try to inject polarized carriers from an adjacent magnetic material[14, 75]. Spin injection is achieved by electrical current injection through a ferromagnetic contact. Ferromagnetic metals such as Fe have been used, but generally the injection efficiency is small[76] due to the Schottky barrier (depletion layer) at the interface, which may be as thick as hundreds of nanometers.

The spin polarization can be detected optically by measuring the cir-

cular polarization of the recombination electro-luminescence in a quantum well(*e.g.* Ref. [76, 77, 78]). Crooker *et al.* used the optical Kerr effect to image the transport and precession of injected spins[79]. The spin polarization can also be detected electrically. All-electrical injection and detection of electrons spins injected were demonstrated in semiconductors[80, 81, 82, 83].

To avoid the difficulties of metal-semiconductor interfaces, there has also been much effort in developing ferromagnetic semiconductors, either of the dilute variety, such as GaAs doped with a few percent Mn[55, 60] (discussed in Section 1.2.1), or dense, such as EuO[84]. The closer conductivity match with the nonmagnetic semiconductor leads to much more efficient spin injection, but the transition temperatures are still too low for a useful room temperature device.

Spin injection has been demonstrated in metals and semiconductors, such as GaAs, typically using spin-resolved optical or electrical detection of carriers transmitted through a nonmagnetic layer, yielding an overall measure of the effect. While such measurements are very sensitive, a much more detailed understanding could be obtained from a depth profile of the induced spin polarization, which could then be compared to theory. There are few techniques capable of such depth-resolved magnetic measurements on nanometer length scales[85]. We will see that variable energy β-NMR is a sensitive depth-resolved way to probe the distribution of magnetic field in heterostructures (Chapter 2), and we will use this technique to study spin injection from ferromagnetic metals and semiconductors into nonmagnetic semiconductors in Chapter 5.

1.4 Organization of This Thesis

This thesis presents β-NMR studies on three spintronic materials: the GaAs crystals, the ferromagnetic semiconductor Mn doped GaAs and Fe/nGaAs heterostructures. The GaAs crystals (semi-insulating and heavily doped n-GaAs) were studied as control experiments. Chapter 2 will give an introduction of the technique used in the study–β-detected NMR.

Chapter 3 will discuss the local magnetic field in the semiconductor

GaAs: semi-insulating and heavily doped n-type. This constitutes a "baseline" for the β-NMR studies of thin films grown on GaAs substrates. The beta-detected NMR experiments carried out on both GaAs crystal wafers use the pulsed radio frequency scheme to make high resolution measurements. As a control experiment, we investigate the magnetic properties as a function of temperature and depth. The range of depths probed, from $\sim$140 nm down to $\sim$20 nm, coincides with the region of electronic band-bending due to the surface. Similar measurements are made on heavily doped n-type GaAs for comparison, whose Schottky barrier width is reduced to ~ 20 nm because of its high carrier concentration.

The β-NMR studies on Mn doped GaAs are presented in Chapter 4. The magnetic properties of a 180 nm thick epitaxial film of the dilute magnetic semiconductor $Ga_{1-x}Mn_xAs$ with $x = 0.054$ are investigated using beta detected NMR of low energy implanted $^8Li^+$. We follow the temperature dependence of the local magnetic field in the $Ga_{1-x}Mn_xAs$ thin film through the ferromagnetic transition, and discuss the microscopic magnetic phase separation that has been suggested by some low energy muon spin rotation measurements[50]. In $Ga_{1-x}Mn_xAs$, the resonance shift and broadening are much larger than in GaAs crystals (Chapter 3). Therefore we can concentrate on the resonance in the $Ga_{1-x}Mn_xAs$ layer and neglect the tiny shift in the GaAs substrate.

Chapter 5 follows the line of Chapter 3, presenting the β-NMR study on the Fe/GaAs heterostructures. The local field of the GaAs substrate under the effect of the adjacent thin Fe layer due to the proximity effect is probed as a function temperature and implantation depth. In addition, current is injected in the $Fe/n-GaAs$ heterostructure while ^8Li beam is continuously injected to detect the local field *in situ*.

Chapter 6 summarizes the results on the β-NMR studies on spintronic materials, and discusses the potential of depth-resolved β-NMR for investigating spintronic materials in reduced geometries with the new capability of current injection.

Chapter 2

The β-NMR Technique

β-NMR is a powerful and sensitive tool in condensed matter physics and material science, but it is not widely known or widely used. It is very specialized with only a few groups worldwide. This technique, similar to conventional NMR, provides a precise local probe to conduct investigations on, *e.g.* micro structures, local magnetism, hyperfine interactions, spin relaxation, impurities and defects. Conventional NMR requires, in general, $\sim 10^{18}$ probe nuclei to generate measurable signals, so that it's generally not applicable to studies on thin films. In contrast, β-NMR needs only $\sim 10^7$ nuclei, as it is much more sensitive than conventional NMR. In β-NMR a beam of highly spin-polarized radioactive probe nuclei (^{8}Li$^+$ in our case) is introduced into the sample under study. Once implanted into the material, the probe nuclei interact with external and internal magnetic fields within the sample until they decay and emit β particles preferentially opposite to the probe nuclear spin direction. The anisotropic angular distribution of the emitted β particle reflects the probe nuclear spin state inside the material at the moment of its decay. Applying an rf field with a frequency matching the spin resonance condition, the spin polarization can be destroyed by rapid precession with random phases, leading to an isotropic emission of β-electrons and thus the asymmetry reduction.

In this chapter, we will discuss the generation of spin-polarized ^{8}Li$^+$ (Section 2.1) and the β-NMR spectrometer (Section 2.2), and describe the ion implantation profile (Section 2.3) and β-NMR data collection (Section 2.4).

2.1 Production of Spin-Polarized ^{8}Li$^+$

The proton beam with 500 MeV energy generated in the TRIUMF cyclotron is used to drive a secondary radioactive ion beam at the Isotope Separator and Accelerator (ISAC) facility. The high energy proton beam bombards a special production target and produces various radioactive ions by nuclear reactions. The production target, typically tantalum or SiC, usually is heated to ~ 2500 °C, and held at a high positive voltage of 28–30 kV. Thermal ionization at the surface of the target produces isotopes of metals with low ionization energies, such as the alkali metals. After diffusing to the surface and ionizing, the ions are accelerated by the target potential to 28–30 keV. The desired isotope is selected by a high resolution mass separator. Although many β-emitting isotopes are suitable β-NMR nuclei, a good β-NMR probe needs to meet some basic requirements. The isotope must have high production rate and be able to be efficiently spin polarized. It should have a high β-decay asymmetry and small nuclear spin to keep the spectra simple. Table 2.1 lists some isotopes suitable for β-NMR among which ^{8}Li$^+$ is the easiest to generate with high intensity ($\sim 10^8$ ion/s) at ISAC. The ion beam of interest is then focused and steered to the β-NMR experiment station by electrostatic beamline elements. The other two isotopes ^{11}Be and ^{15}O are also suitable for β-NMR, but there are important differences. For instance, ^{15}O is spin 1/2 particle with no quadrupole moment, which simplifies its spectrum in complex structures. Also its lifetime (122 s) is much longer than the ^{8}Li$^+$ lifetime, so it could only be used if the relaxation time T_1 is very long.

The radioactive beam is polarized by optical pumping using circularly polarized light from a single-frequency ring dye laser. A diagram of the polarizer and the spectrometer is shown in Fig. 2.1. The polarization process includes three steps. First the ion beam ^{8}Li$^+$ is neutralized by passing through a cell of Na vapor, typically held at 480 °C. The neutral beam then flows into the optical pumping region (1.9 m long) where a small longitudinal field of 1 mT is present to maintain the polarization axis. The remaining ^{8}Li$^+$ ions that are not neutralized after Na cell are removed by

21

Isotope	Nuclear Spin I	$T_{1/2}$ (s)	γ (MHz/T)	β-Decay Asymmetry	Production Rate (s^{-1})
^{8}Li	2	0.842	6.3018	0.33	10^8
^{11}Be	1/2	13.8	22	0.016[86]	10^6[86]
^{15}O	1/2	122	10.8	0.7[87]	10^8

Table 2.1: Some isotopes suitable for β-NMR study. Properties listed are nuclear spin I, half life $T_{1/2}$, gyromagnetic ratio γ, β-decay asymmetry, and production rate.
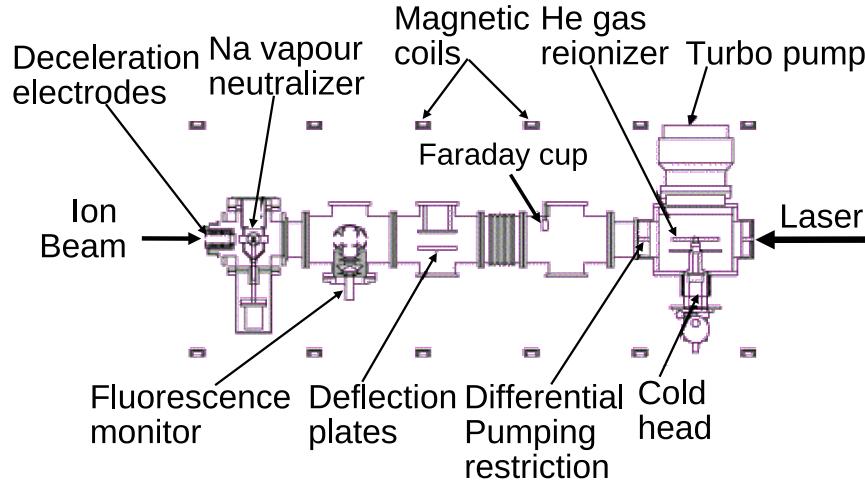
Figure 2.1: A schematic diagram of ISAC collinear polarizer. Adapted from [88].

two electrostatic deflection plates and dumped into a Faraday cup.

Optical pumping is carried out by a single frequency dye laser which is pumped by a Nd:YAG laser. The neutral ^{8}Li atoms interact with the counter-propagating laser light which is circularly polarized with respect to the magnetic holding field axis. The laser is tuned to 671 nm, the wavelength of Li D1 transition– the transition from the ground state $^2S_{1/2}$ to the first excited state $^2P_{1/2}$. As shown in Fig.2.2, due to the hyperfine coupling between the total electronic angular momentum for $^8Li^0$ atoms ($J = 1/2$) and the nuclear spin ($I = 2$), both the ground state $^2S_{1/2}$ and the first excited state $^2P_{1/2}$ are split into two hyperfine levels of total angular momentum of

22
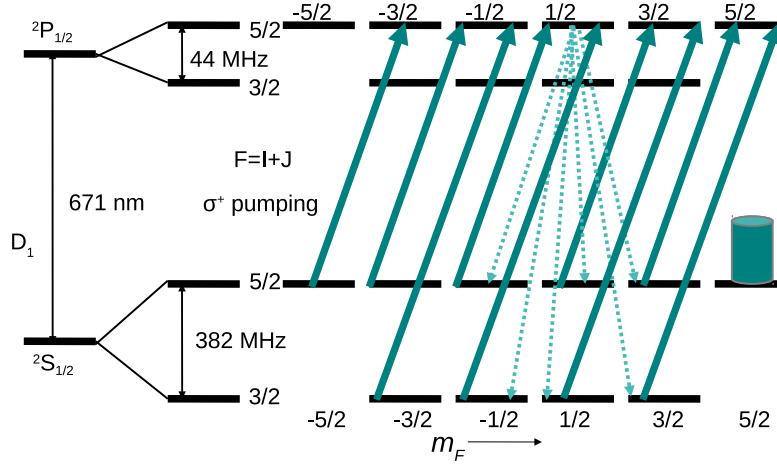
Figure 2.2: Optical pumping scheme with σ^+ light for the D1 transition of ^{8}Li. The excitation induced by the laser is shown in heavy arrows, and the spontaneous emission is in thin arrows. After many cycles of optical pumping, all atoms are "pumped" into the fully stretched state (m_F=5/2) with full nuclear and electronic polarization, and can't be pumped out of this state by laser light. Adapted from Ref. [88].

the atom electron $J = 1/2$ and nuclear spin $I = 2$ ($F = J + I$): $F = 3/2$ and $F = 5/2$. The splitting is 382 MHz in $^2S_{1/2}$ state , and 44 MHz in $^2P_{1/2}$ states. In the presence of a small external holding field (~ 10 G), the hyperfine levels are further split into 2F+1 almost degenerate sublevels with magnetic quantum number m_F ($m_F = -F, -F + 1, \cdots, F - 1, F$). For circularly polarized light with positive helicity (σ_+ pumping), the only allowed absorptions are transitions increasing m_F by +1, $\Delta m_F = +1$, whereas the spontaneous emission can occur with $\Delta m_F = 0, \pm 1$. The quantization axis is established by the helicity direction of the laser light and maintained by the small magnetic field. The lifetime for spontaneous fluorescence of the excited state is ~ 50 ns, much shorter than the transport time through the optical pumping region ($\sim \mu$s). Therefore ^{8}Li atoms have gone through multiple pumping cycles when they reach the end of the region, and a high degree of electronic and nuclear spin polarization is achieved. After about
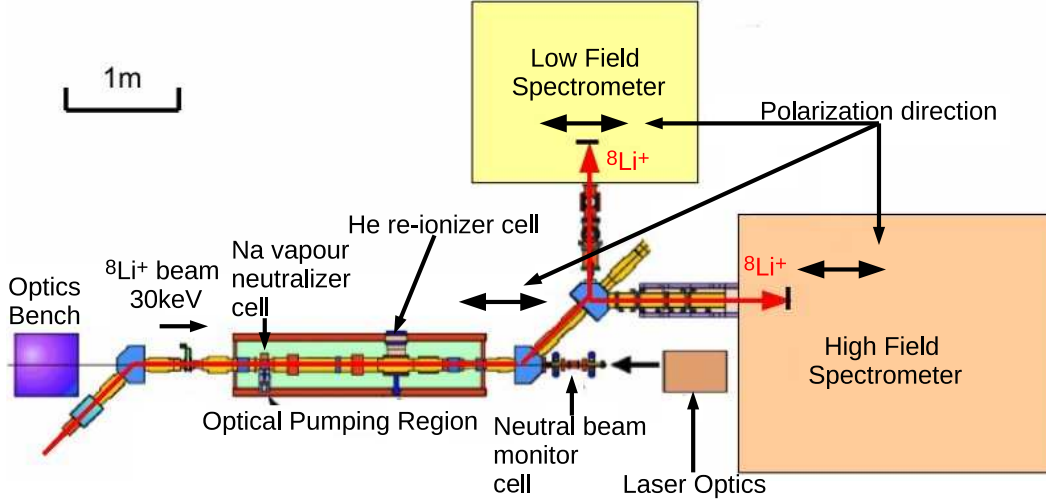
Figure 2.3: A schematic layout of ISAC collinear polarizer and β-NMR spectrometer. Adapted from Ref. [89].

10-20 cycles of absorption and emission, the angular momentum carried by the photons is transferred to the ^{8}Li atoms. Thus the atoms are "pumped" towards a state of high atomic spin polarization. For the positive helicity of the laser light, the atoms are pumped to a state of $F = 5/2, m_F = 5/2$ with a high degree of nuclear polarization (70%). Correspondingly the nuclear spin state is $m_I = +2$, and the nuclear spin polarization is antiparallel to the holding field direction. For the negative helicity, ^{8}Li atoms are pumped to the state $F = 5/2, m_F = -5/2$. In this case, $m_I = -2$ and the nuclear spin polarization is parallel to the holding field. The nuclear polarization is defined as:

$$P = \frac{1}{I} \sum_{m_I} m_I p_m \tag{2.1}$$

where m_I is the magnetic quantum number of the nuclear spin, and p_m is the population of the corresponding quantum state. $\mathbf{P}$ is defined with respect to the longitudinal holding field which is set as the $\hat{z}$ direction. The optically-generated nuclear polarization along this direction is the initial nuclear polarization of $^8Li^+$ and denoted as P_o.

Finally, the beam is re-ionized by passing it through a He gas cell, ion-

izing the ^{8}Li with an efficiency of $\sim 50\%$. The spin-polarized and recharged ^{8}Li$^+$ beam is steered through a 45° electrostatic bending element and is delivered to the low- (β-NQR) or high-field (β-NMR) spectrometers (Fig. 2.3). Any ^{8}Li that are not re-ionized go straight into a neutral beam monitor (NBM) at the end of the polarizer. The nuclear polarization is preserved during the electron stripping process. The polarization of ^{8}Li$^+$ is parallel to the momentum at β-NMR station and perpendicular at the β-NQR spectrometer.

We now have a beam of probe ^{8}Li$^+$ at (28.000 ± 0.001) keV that are spin polarized and they can now be directed onto a sample held in the spectrometer.

2.2 The β-NMR Spectrometer

The high field spectrometer is designed with longitudinal geometry. The ^{8}Li$^+$ spin polarization and the external magnetic field are both along the beam axis (Fig. 2.4 Panel a). This is necessary because the incoming ions and outgoing β-electrons are both strongly focused by the magnet at a high magnetic field. In order to detect β-electrons in the backward direction, it is required that the detector be outside the magnet since the β-electrons are confined to the magnet axis while inside the magnet bore. Although the solid angles subtended by the two detectors in zero field are very different, they have similar detection efficiencies in high magnetic fields due to the focusing effect of the solenoid.

In the section just before the high field spectrometer, there are three electrostatic Einzel lenses and three adjustable collimators which control the beam spot on the sample. A schematic drawing of the spectrometer is shown in Fig. 2.4 Panel a. The polarized beam enters from the left and passes through a hole in the back detector before entering the last Einzel lens at the entrance to the superconducting solenoid generating a homogeneous magnetic field up to 9 Tesla. ^{8}Li$^+$ beam is focused by the magnetic field on to the sample, and the beam spot at the center of the magnet is a sensitive function of Einzel lens voltage, magnetic field and beam energy. Images of
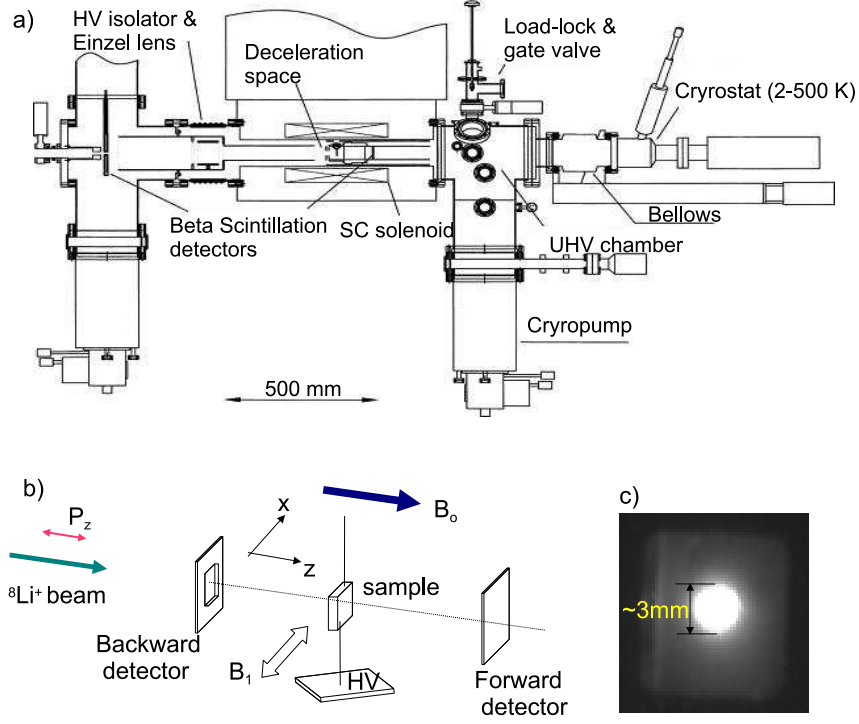
Figure 2.4: a: the layout of β-NMR spectrometer at ISAC. The beam incident from the left enters the spectrometer by passing through the hole at the center of the backward scintillation detector, and is focused to the sample by the high magnetic field generated by superconducting solenoid. The emitted β-electrons are detected by forward and backward scintillation detectors centered on the axis of the field. Adapted from Ref. [89]

b: the geometry of β-NMR experiment. The sample is sitting on a high-voltage platform. c: a typical beam spot image on a sapphire disk in the high field. Adapted from Ref. [90]

the ^{8}Li$^+$ beam at the sample position were obtained by using a sapphire scintillator at the sample location and taken by a CCD camera. Fig. 2.4 Panel c shows a typical image of the focused β-NMR beam spot usually of 2-4 mm in diameter depending on the above conditions.

As shown in Fig. 2.4 Panel b, the polarization of ^{8}Li$^+$ is along the beam axis, and parallel to the magnetic field $B_o = B_o \hat{z}$ (100 G $< B_o <$ 6.5 T). A small Helmholtz coil is used to apply a transverse radio-frequency (rf) field $B_1(t)$ ($B_{1max} \sim 1$ G) at frequency ω in the horizontal direction, perpendicular to both the beam and the initial polarization. For a photo of this coil, see Fig. 2.5b). Two plastic scintillators are placed in front and behind the sample to detect the outgoing β-electrons emitted from the ^{8}Li$^+$ β-decay. The emitted β-electrons have an average energy ~ 6 MeV and thus can easily pass through thin stainless steel windows in the UHV chamber to reach the detectors. The backward detector is located outside the bore of the magnet as mentioned above. The focusing effect of the high magnetic field leads to similar detection efficiencies in both detectors although they have different solid angles as the forward detector is much closer to the sample. The sample is mounted on a UHV cold finger cryostat (Oxford Instruments). UHV is critical to avoid the buildup of residual gases on the surface of the sample at low temperature. The pressure in the main chamber can be reduced to 10^{-10} torr using differential pumping. Temperatures from 300 K to 3 K are obtained by using a helium gas flow cryostat.

The cryostat, connected to a motorized bellows, can be inserted into, or retracted from the bore of the superconducting solenoid (Fig. 2.5 Panel a). This allows us to change the sample through a load-lock without venting the entire UHV chamber. Panel b of Fig. 2.5 shows the end of the cryostat viewed along the axis. When loaded, the sample is at the center of the rf coils. The sample holder port in the cryostat is keyed such that the sample can only be loaded facing the beam. A picture of a typical sample is shown in Panel c of Fig. 2.5. Typically, a β-NMR sample is ~ 8 mm $\times$ 10 mm, 0.5 mm thick. Smaller samples may be attached to a sapphire plate (~ 8 mm $\times$ 10 mm $\times$ 0.5 mm) using UHV compatible silver paint, and clamped to the sample holder (made of copper or aluminum) by two clamps fastened
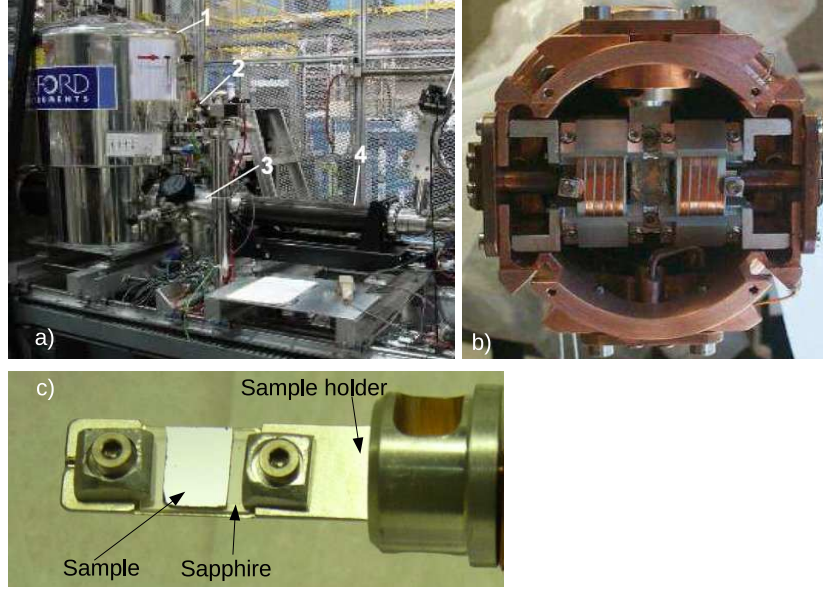
Figure 2.5: a: The β-NMR spectrometer retracted from the bore of the magnet: 1–superconducting solenoid; 2–sample loadlock; 3–UHV chamber; 4–cryostat bellows. b: Axial view of the end of the cryostat (out of UHV) showing the sample position and the rf coil around it. c: The copper housing with a sample mounted on it. The sample is right in the middle of the rf coil.

with M2 screws. We redesigned the sample holder for the current injection experiment. More discussion of this can be found in Appendix C.

The whole spectrometer is placed on a high-voltage platform which is electronically isolated from ground and can be biased up to 30 kV. By biasing the platform, the incident ^{8}Li$^+$ must overcome the electrostatic potential barrier generated by the bias voltage before they reach the sample. Therefore the ^{8}Li$^+$ beam is decelerated and injected into the sample with different energies, stopping in the sample at different implantation depths. The bias voltage is thus an adjustable parameter controlling the beam implantation depth and allowing depth-resolved measurements. Depth-resolution is an important capability of the β-NMR spectrometer. The whole platform is caged and interlocked for safety. We will discuss β-NMR implantation profile

and how it varies with implantation energy in more details in the next session (Section 2.3).

2.3   β-NMR **Ion Implantation Profile**

As mentioned above, the implantation energy of $^8Li^+$ ions can be controlled by adjusting the platform bias voltage, corresponding to different implantation depths–from several nanometers to a few hundred nanometers. $^8Li^+$ with a higher implantation energy stop further in the sample, and *vice versa*. The deceleration of $^8Li^+$ is an important characteristic of the β-NMR spectrometer, allowing for the depth-controlled surface and interface studies.
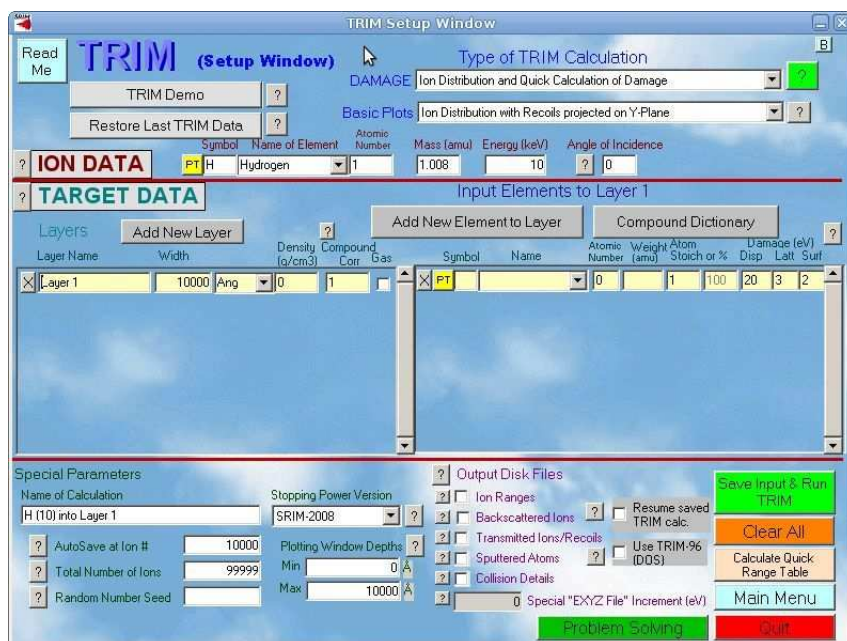
Figure 2.6: SRIM graphic interface. The ion implantation profile is simulated by specifying the probe's charge, atomic mass and energy as well as the densities of target materials in each layer and their thicknesses[91].

Ion implantation is an inherently random process, with each ion following an individual path as it scatters from atoms in the target. However, due to

the large numbers of ions involved, it is possible to describe the ion profile statistically. The program Stopping and Range of Ions in Matter (SRIM) can simulate the depth profile of the implanted ions in materials. This program is based on the binary collision approximation model using Monte Carlo algorithms for atomic collision processes in solids[91, 92]. The accuracy in calculating ion range distributions in various materials is well established, and it is routinely used in similar depth controlled experiments such as low-energy μSR[93]. Fig. 2.6 shows the graphic interface of the program SRIM. The implantation profile is simulated by specifying the properties of both the incident beam and the target material, including the beam energy, ion charge and atomic mass for the probe, the number of probe particles, and the composition, density and thickness of each layer of the sample under study.

Two parameters of an implantation profile are important in this thesis: projected range and ion straggle[91]. The projected range is the averaged stopping range of ^{8}Li$^+$ in the target, and is referred to as "the implantation depth". The ion straggle (width) is defined as the standard deviation, which characterizes distribution of the stopping range. As an example of a SRIM simulation result, the left panel of Fig. 2.7 shows the characteristic asymmetric and positively skewed distribution of ^{8}Li$^+$ with the beam energy of 5 keV into a GaAs crystal. At 5 keV, the ion range is $\sim$ 31 nm. The profile is narrow with a straggle of $\sim$ 17 nm.

The implantation depth and straggle of ^{8}Li$^+$ with different implantation energies is shown in the right panel of Fig. 2.7. The average depth increases from $\sim$20 nm with the beam energy of 3 keV to $\sim$140 nm at full beam energy. At low energy, a significant fraction of ^{8}Li$^+$ is backscattered from the sample.

The fraction of ions that backscatter is strongly energy dependent, so this is a potentially important systematic effect to consider when comparing different implantation energies. If one ^{8}Li$^+$ backscatters as an ion, the high magnetic field will confine it to the magnet axis and it will likely exit the cryostat and stop upstream possibly near the back detector. On the other hand, it is possible that the backscattered ion captures an electron
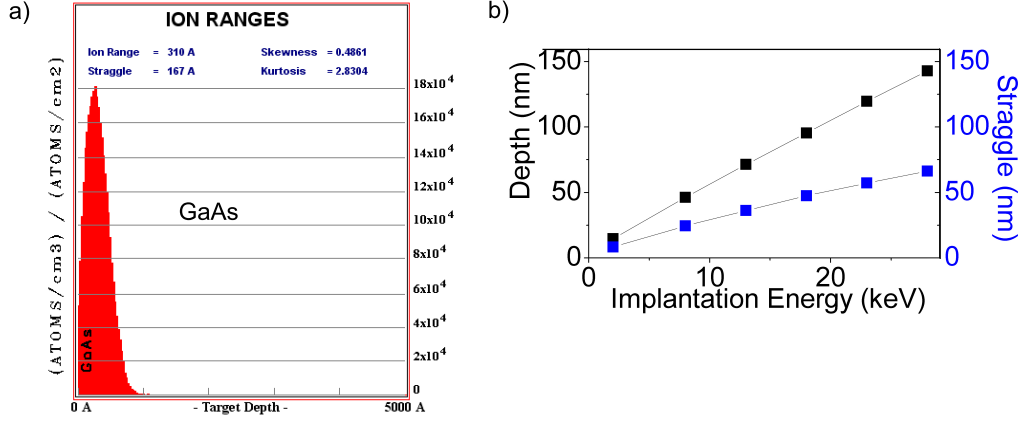
Figure 2.7: Left: The SRIM simulation of the implantation profile of ^{8}Li$^+$ with the implantation energy of 5 keV in GaAs. Right: The implantation depth and width (straggle) with various beam energies.

and leaves as a neutral atom. The trajectories of such atoms are not affected by the magnetic field or the electric field, and these ^{8}Li may stop in the spectrometer in or near the coils in materials such as Cu, Al, ceramic or vespel. Such ^{8}Li may result in a background signal. However, if they are not located near the rf coil, they will not contribute a background resonance signal. The effect of backscattering likely causes a systematic energy dependence on the baseline asymmetry defined below (Section 2.4.1).

Although SRIM simulation provides a reasonable profile prediction, it does not include channeling effects which may be very important in certain single crystalline materials along specific directions. An example is given in Fig. 2.8 from Ref. [94]. The long tail due to the channeling effect extends up to 6–6.2 μm in the measured depth profile (left panel of Fig. 2.8), but is not accounted for in SRIM simulation (right panel of Fig. 2.8). Channeling of implanted ions occurs for incidence below a critical angle Ψ that is estimated simply as[95]

$$\Psi = \sqrt{\frac{2Z_1 Z_2 e^2}{dE}} \tag{2.2}$$

where Z_1, Z_2 are the atomic number of the incident particle and the stopping
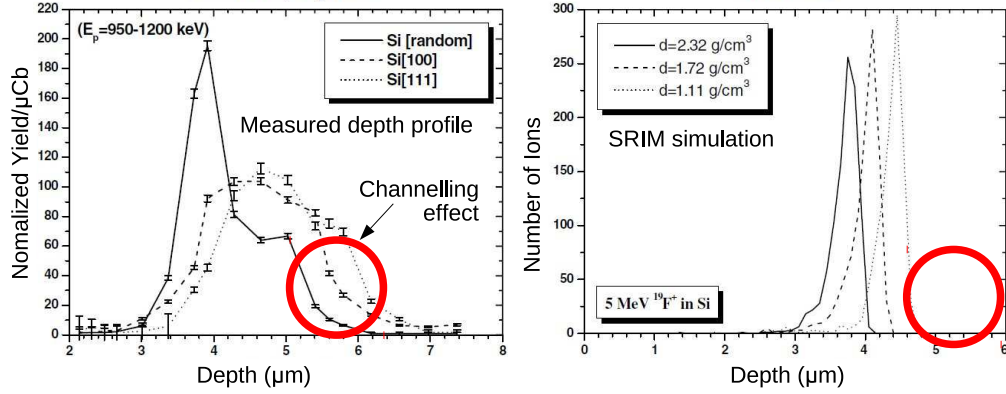
Figure 2.8: An example of the discrepancy of the measured depth profile and SRIM simulation. Left: experimental fluorine depth profile in Si[94]. The random orientation (no channeling) is presented in comparison with the Si(100) and Si(111) channeling orientations for the same accumulated fluence of $\sim 10^7$ atoms/cm^2. Right: SRIM-2000 simulation for the random case. Adapted from Ref. [94].

medium, E is the incident energy and d is the distance between lattice atoms along a chain in the channeling direction. The role of channeling in GaAs is considered in Section 4.3.

2.4   β-NMR **Data Collection**

In this section, I will describe the procedure for recording resonance spectra (a function of frequency) in Section 2.4.1 and spin-lattice relaxation spectra (a function of time) in Section 2.4.2. For both types of spectra, we measure the difference between the count rates in the forward and backward counters, the asymmetry A, resulting from the β decay of the ^{8}Li$^+$ which violates parity symmetry.

The ^{8}Li nucleus decays into ^{8}Be in an excited state and emits one electron and one antineutrino:

$$^8_3\textbf{Li} \longrightarrow {}^8_4\textbf{Be} + e^- + \overline{\nu}_e \qquad (2.3)$$
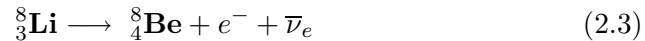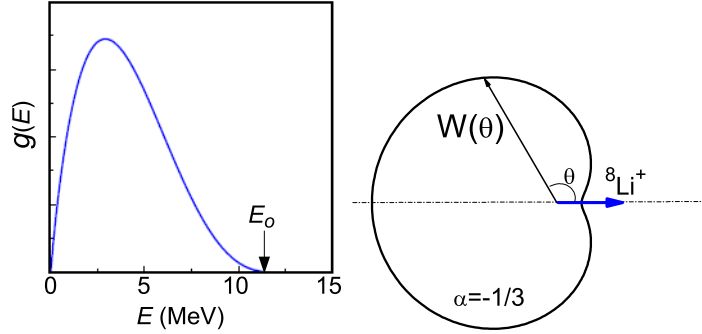
Figure 2.9: The angular (left) and energy (right) distributions of the emitted electrons after ^{8}Li$^+$ β-decay. The asymmetry factor $a = -\frac{1}{3}$. Adapted from Ref. [96]

The emitted β-electrons have an average energy of ~ 6 MeV, with a maximum (end-point) energy of $E_o = 12.5$ MeV[97] (Fig. 2.9 left panel). The weak interaction does not conserve parity, and this leads to an angular distribution $W(\theta)$ of the emitted electrons (Right panel of Fig. 2.9):

$$W(\theta) = 1 + aP\frac{v}{c}cos\theta \tag{2.4}$$

where v is the average velocity of the electrons emitted from the β-decay, c is the speed of light (at these energies $v \approx c$), $a = -\frac{1}{3}$[97] is the asymmetry factor of the β-decay of ^{8}Li$^+$, P is the nuclear polarization (from Eqn. (2.1)), and θ is the angle between the β-decay emission direction and the spin polarization axis. Thus the β-electrons are emitted preferentially in the opposite direction (negative a) to the nuclear spin polarization at the moment they decay. As described in Section 2.2, the ^{8}Li$^+$ ions are implanted with their polarization either parallel or antiparallel to their momentum, depending on the helicity of the laser light. The emitted β-electrons are detected by the forward (F-) or backward (B-) detector, and the counting rate $N_{F/B}$ is:

$$N_{F/B} = \epsilon_{F/B}W(\theta = 0/\pi) = \epsilon_{F/B}(1 \pm aP) \tag{2.5}$$

33

where $\epsilon_F(\epsilon_B)$ is the experimental factor depending on the detection efficiency of the forward (backward) detector and their geometry. Therefore the ratio of the two detectors' counting rates is:

$$\frac{N_F}{N_B} = \frac{\epsilon_F(1 + aP)}{\epsilon_B(1 - aP)} \tag{2.6}$$

Assuming similar detection efficiencies and solid angles of both detectors ($\epsilon_F \approx \epsilon_B$)), one can find:

$$aP = \frac{N_F - N_B}{N_F + N_B} \equiv A(t) \tag{2.7}$$

The final polarization (P) of ^{8}Li just before it decays is directly proportional to the asymmetry (A), defined by Eqn. (2.7) of the β counting rates between the two detectors, and its evolution can be deduced by measuring the asymmetry $A(t)$ as a function of time.

The measured asymmetry can be affected by many factors such as the scattering of the β-electrons in the sample, the background count rates, and the geometrical inequalities between the two detectors. To overcome the instrumental effects, the asymmetry is measured in positive (A^+) and negative (A^-) helicity of the laser light. The separate helicities are combined to calculate the difference in asymmetry A:

$$A = \frac{A^+ - A^-}{2} \tag{2.8}$$

Multiple scans are accumulated alternately between the two helicities to improve the statistics. Each scan can be viewed individually and discarded if it's of poor quality. Scans in a given helicity are averaged before combination into a single spectrum.

2.4.1 β-NMR Resonance Spectra

β-NMR adopts a method similar to conventional Continuous-wave (CW) NMR to measure the spin resonance. Spin-polarized ^{8}Li ions are continuously injected into the sample and interact with sample nuclear and elec-
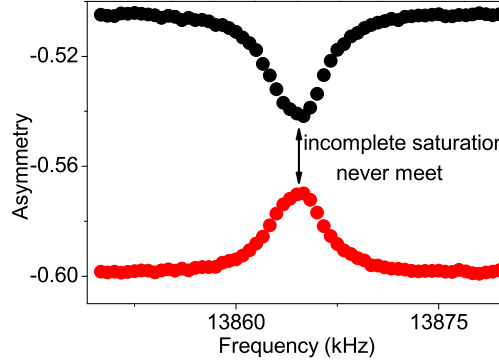
Figure 2.10: An example of the incomplete saturation. The resonance in two helicites does not meet at midway.

tronic spins, as well as electronic currents, before they decay and emit β-electrons. One can perturb the ^{8}Li spins by applying a small oscillating radio frequency (rf) field B_1, normal to the static field B_o, and record the asymmetry as a function of this rf frequency ν (Fig. 2.4 b). The Larmor frequency of ^{8}Li$^+$ is defined as:

$$\nu_L = \gamma B_{tot} \tag{2.9}$$

where γ = 630.15 Hz/G is the gyromagnetic ratio of ^{8}Li$^+$, and B_{tot} is the total local magnetic field. When ν matches the Larmor frequency, the ^{8}Li$^+$ precess about B_{tot}, resulting in depolarization of ^{8}Li$^+$ spin, and thus a reduction of the asymmetry. With enough rf power, all the ^{8}Li$^+$ could be excited at the resonance frequency. In this case, the ^{8}Li$^+$ polarization is completely suppressed, and the asymmetry in each helicity meets at midway. Sometimes the rf power is not high enough, the resonances in two helicities do not meet as shown in Fig. 2.10. An example of complete saturation is shown in Fig. 4.14 (open blue squares in the top panel).

In conventional NMR, a large static magnetic field is applied to polarize the nuclear spins sample under study, and a pick-up coil is needed to detect the induced signal from the ensemble's nuclear spin polarization. Therefore, a large number of particles ($\sim 10^{18}$) are required. However in β-NMR

the signal is generated by the injected ^{8}Li$^+$ which is already highly spin-polarized (Section 2.1) and is detected by measuring the asymmetry of the electrons emitted by ^{8}Li$^+$ in the β-decay rather than a pick-up coil. Therefore only $\sim 10^7$ particles are needed for a resolvable signal, β-NMR is in this sense more sensitive than conventional NMR and can be used to study, for example, materials only available in thin film form such as Mn doped GaAs (Chapter 4) and thin film interfaces (Chapter 5).

The β-NMR resonance provides information about the magnetic and electronic properties in the material. The Larmor frequency ν_L indicates the total magnetic field at the probe site B_{tot}. B_{tot} is determined by the applied external field B_o and the static and time-averaged internal magnetic field B_{int} from the atomic environment:

$$\mathbf{B}_{tot} = \mathbf{B}_o + \mathbf{B}_{int} \qquad (2.10)$$

A shift of the resonance frequency $\Delta\nu$ is calculated by comparing the resonance frequency in the material of interest ν to that in the reference material ν_{ref}:

$$
\begin{aligned}
\Delta\nu &= \nu - \nu_{ref} \\
&= \gamma(B_{tot} - B_{ref})
\end{aligned}
\qquad (2.11)
$$

Usually we use MgO as the standard reference material to calculate the resonance shift. MgO is nonmagnetic insulator with a simple cubic lattice, and the nuclear moments from Mg and O are negligible and this ^{8}Li$^+$ resonance is very narrow. Therefore the total local magnetic field in MgO is the same as the applied external field ($\nu_{MgO} = \gamma B_o$) and the resonance is very sharp (only ~ 0.4 kHz in pulsed rf mode (see Section 2.4.1.2)). Therefore, Eqn. (2.12) can be further written as :

$$
\begin{aligned}
\Delta\nu &= \nu - \nu_{MgO} \\
&= \gamma(B_{tot} - B_o) \\
&= \gamma B_{int}
\end{aligned}
\qquad (2.12)
$$

Sometimes we convert the resonance shift ($\Delta\nu$) into the relative shift (δ) in the unit of parts per million (*ppm*):

$$\delta = \frac{\nu - \nu_{ref}}{\nu_{ref}} \times 10^6 \qquad (2.13)$$

The frequency shift $\Delta\nu$ (or δ) reveals the homogeneous static field causing the enhancement or reduction of the external field by the electrons surrounding the nucleus. The broadening and structure of the nuclear magnetic resonance may reflect inhomogeneities in the static internal field. In a static approximation, the area under the resonance spectrum can be taken as a measure of the number of spins observed in the resonance.

There are two modes of resonance data collection used in this thesis depending on the method used to apply the RF: (1) the continuous wave (CW) where a weak rf oscillating magnetic field is continuously applied; (2) the pulsed rf mode, where a short rf pulse is used. The pulsed rf mode is convenient for narrow resonances and has been used in Mn doped GaAs data (Chapter 4) and in the GaAs crystal (Chapter 3). While the CW mode is useful for measuring broader line and has been used to study the proximity effect of Fe in GaAs described in Chapter 5.

2.4.1.1 Continuous-Wave (CW) Mode

In the CW mode, a small oscillating rf field B_1 is continuously applied perpendicular to B_o in a sinusoidal form:

$$\mathbf{B}_1(t) = B_1 \cos(\omega t)\hat{x} \qquad (2.14)$$

where $B_1 \sim 0.1$–1 G. To measure the asymmetry, the frequency $\nu = \omega/2\pi$ is scanned in steps of Δf in a frequency range ΔR around the Larmor frequency ν_L. The frequency is stepped slowly (~ 1 s per step) compared to the ^{8}Li lifetime to avoid distortions due to ^{8}Li$^+$ memory effect–*i.e.* ions persisting in the sample from previous frequency steps[98]. At each frequency, the counts are measured in N bins of time at t_p per bin. Therefore it takes $t_{scan} = Nt_p\Delta R/\Delta f$ to record each scan. For example, if $\Delta R = 100$ kHz,

$\Delta f = 200$ Hz, $N = 100$, and $t_p = 10$ ms, it is $t_{scan} = 500$ s to finish one scan. After each scan, another scan is taken with the same helicity, but in the opposite direction of the frequency sweep. After two scans with one helicity, the helicity is flipped and new scans starts and so on. After several good scans for each helicity, the scans of each helicity are averaged and then the final asymmetry is calculated using Eqn. (2.8).

The polarization of implanted ^{8}Li$^+$ ions depends on the ^{8}Li$^+$ lifetime τ and the relaxation time of the polarization T_1 in the sample. For a continuous beam of ions implanted at a constant rate R and the initial nuclear spin polarization P_o (Eqn. (2.1)), assuming a single relaxation mechanism (the spin-lattice relaxation rate is $1/T_1$), the dynamic equilibrium value of the polarization in the sample averaged over time is:

$$\begin{aligned} \bar{P} &= \frac{P_o R \int_0^\infty e^{-t/\tau} e^{-t/T_1} dt}{R \int_0^\infty e^{-t/\tau} dt} \\ &= \frac{P_o}{1 + (\tau/T_1)} \end{aligned} \tag{2.15}$$

The forward/backward counters' counting rates $N_{F/B}$ are proportional to the polarization (Eqn. (2.5)). The observed asymmetry in each helicity $A^\pm$ is calculated by Eqn. (2.7) and then combined to yield the total asymmetry A by Eqn. (2.8). As discussed at the beginning of this section, when the rf field is tuned on the resonance Larmor frequency of the ^{8}Li$^+$ in the sample, the ^{8}Li$^+$ polarization precesses in a plane normal to B_1, and β-electrons are emitted isotropically due to the result rapid precession in the rotating reference frame. Therefore the rapid precession during the integration time results in a loss of the average polarization and a decrease in the observed asymmetry. Fig. 2.11 shows an example of a CW resonance spectrum in MgO–the standard material in the β-NMR experiment. The resonance spectrum is taken at room temperature in a magnetic field of 2.2 T. The left panel shows spectra with positive and negative helicities. The combined asymmetry is shown in the right panel.

The NMR line is not infinitely sharp. It could be broadened by inhomogeneity of the internal field, power broadening due to the oscillating field
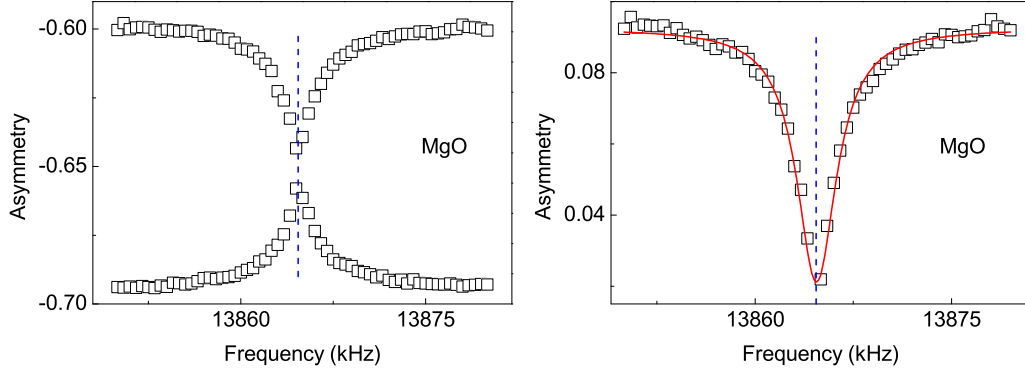
Figure 2.11: Typical CW mode resonance spectrum of $^8\text{Li}^+$ in MgO at room temperature in the external magnetic field of 2.2 T. The left panel is the spectra with positive and negative helicities, and the right panel is the combined asymmetry. The spectrum is fit to one Lorentzian (Eqn. (2.16)), and the linewidth is 3.7 ± 0.1 kHz.

B_1, and relaxation processes (*e.g.* relaxation rate $1/T_1$). For any line shape, we define its linewidth as the full-width at half maximum (FWHM). In CW mode, the large amplitude of B_1 leads to power broadening of the resonance. The broadening due to B_1 is temperature-independent and gives rise to a Lorentzian line[99]:

$$A(\nu) = A_o - \frac{A_{amp}\sigma^2}{4(\nu - \nu_o)^2 + \sigma^2} \tag{2.16}$$

where A_o is the baseline, ν_o, σ and A_{amp} are the resonance position, width (FWHM) and amplitude, respectively. When $^8\text{Li}^+$ stop in a region with two distinct magnetic environments (*e.g.* the thin magnetic film and the substrate on which the film is grown epitaxially), one expects two resonances in the spectrum. In this case, we fit the spectrum to multiple peaks, two Lorentzians for example:

$$A(\nu) = A_o - \left(\frac{A_{sub}\sigma_{sub}^2}{4(\nu - \nu_{sub})^2 + \sigma_{sub}^2} + \frac{A_{over}\sigma_{over}^2}{4(\nu - \nu_{over})^2 + \sigma_{over}^2}\right) \tag{2.17}$$

where $i = sub$ and *over* denotes the resonance in the substrate and in the

39

overlayer thin film respectively. An example of two component resonance spectrum will be shown in Chapter 4.

Since Lorentzian widths add linearly, the measured width is approximately:

$$\sigma = \sigma_{int} + (\gamma H_1) + (1/\tau + 1/T_1) \tag{2.18}$$

where σ_{int} is the intrinsic static linewidth, γH_1 is the power broadening, and $(1/\tau + 1/T_1)$ is the dynamic relaxation broadening. In the materials studied in this thesis, the dynamic contribution is at least 2 orders of magnitude smaller than σ_{int} at all temperatures, and thus negligible.

^{8}Li$^+$ are spin $I = 2$ ions with a small electric quadrupole moment $Q = +31$ mB[100]. In general, the quadrupole moment results in a quadruple splitting of the spectrum if ^{8}Li$^+$ ions stop at non-cubic sites where there is an electric field gradient (EFG). The data shown in this thesis were all collected in a high magnetic field ($\sim 1 - -4$ T) and in materials based on the GaAs crystal, a semiconductor of zinc-blende structure. When ^{8}Li$^+$ stop in the GaAs crystal, they prefer to take up the substitutional Ga sites or interstitial sites, both of which are of cubic symmetry. At cubic sites, the electric field gradient (EFG) is zero by symmetry, so that the quadrupole interaction also vanishes. However, any imperfections in the GaAs crystal, *e.g.* created by dislocations, strains, or vacancies, create non-vanishing EFGs at ^{8}Li$^+$ stopping sites, which vary both in orientation and in magnitude from site to site and have an influence on the lineshape of the spectrum. In a high magnetic field, the quadrupole interaction is much smaller than the Zeeman interaction, and can be treated as a perturbation. In this case, the quadrupole interaction contributes to the intrinsic β-NMR linewidth (σ_{int}), and the quadrupole broadening σ_Q is usually independent of temperature or the magnetic field (in the high field limit).

From Eqn. (2.7) and Eqn. (2.15), we can see that the asymmetry is affected by the relaxation rate $1/T_1$, $A \propto \frac{P_o}{\tau/T_1}$ for $\tau/T_1 \gg 1$. Therefore, a fast relaxation rate results in a lower baseline asymmetry A_o and smaller resonance amplitude. The average polarization P_o is scaled down by the relaxation rate $(1/T_1)$. We divide the resonance amplitude A_{amp} by the

baseline A_o to account for the relaxation and calculate the normalized amplitude A_{norm}. As already discussed, the area of the resonance in β-NMR is used as a measure of the number of ^{8}Li$^+$ contributing to the resonance. For a sharp peak, we use the multiple of the normalized amplitude A_{norm} and the width σ to approximate the peak area. This analysis will be applied to the data shown in Chapters 4 and 5.

Using this mode, we can measure resonances as broad as $\sim$30 kHz. For narrow lines, the linewidth is comparable to the artificial power broadening γB_1. In this case, we use the pulsed rf mode.

The CW mode resonance is sensitive to instability of the beam. Such instability may result in a time-dependent change to the measured asymmetry $A(t)$, which interferes with the measurement of the resonance lineshape. For example, a time-dependent change in the baseline asymmetry induced by the beam drifting can not be distinguished from a change in the polarization induced by the rf field. Since these variations in $A(t)$ occur on the time scale of ^{8}Li$^+$ lifetime τ or longer, we could avoid this problem by applying the rf field in the form of rf pulses instead of continuous waves.

2.4.1.2 Pulsed RF Mode

If the β-NMR resonance is narrow, we use rf pulses to avoid the power broadening. The rf pulse is applied on a short time scale (10 – 160 ms), much shorter than the ^{8}Li$^+$ lifetime τ ($\sim$ 1 s). Therefore the sensitivity of the β-NMR resonance to the instability of beam is reduced.

In β-NMR short rf 90° pulses (ln-sech pulse) are applied periodically to suppress the polarization while the beam is continuously on. The shaped rf pulse is applied at the required frequency ω to excite a frequency band width $\Delta\omega$. A common shape in pulsed NMR is the frequency and amplitude modulated hyperbolic secant pulse[101]:

$$\mathbf{B}_1(t) = B_1 \text{sech}(\beta t)(e^{i\Phi(t)})\hat{x} \qquad (2.19)$$

where B_1 is the rf field amplitude ($\sim$ 0.1-1 G), β is a constant proportional to the bandwidth $\Delta\omega$, $\Phi(t) = \mu(\ln(\text{sech}(\beta t)))$ is the phase, and μ is a constant.
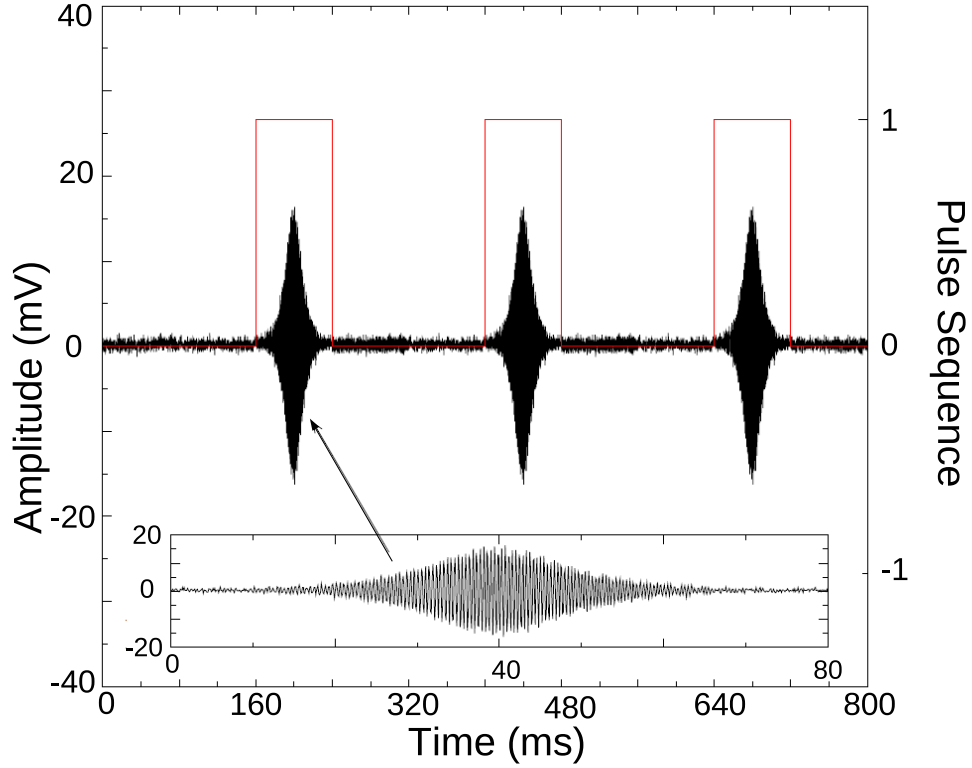
Figure 2.12: A typical rf pulse sequence used in β-NMR. The hyperbolic secant (ln-sech) pulse (black line) is on for $t_p = 80$ ms corresponding to a bandwidth of $\Delta\omega = 200$ Hz. The pulse sequence (red line) regulates the rf delivery. The inset is the enlarged ln-sech pulse. Adapted from Ref. [96].

The rf is on periodically for a short time $t_p \propto 1/\Delta\omega$ and t is truncated between $\pm t_p/2$. Fig. 2.12 shows a typical rf pulse used in β-NMR. The rf pulse is on during $t_p = 80$ ms corresponding to a bandwidth of $\Delta\omega = 200$ Hz.

The rf pulse is shaped to destroy the polarization of $^8\text{Li}^+$ whose Larmor frequency falls in the frequency interval $\omega \pm \Delta\omega/2$. The change in the polarization before and after the pulse is proportional to the number of spins with resonance frequency in that interval. Therefore the polarization change is non-zero only at the resonance frequency. To find the asymmetry,

the counts are measured in a time bin t_p before and after the rf pulse. The asymmetry for each helicity ($h = \pm$) is $A^h(t) = A^h_a(t) - A^h_b(t)$, where $A^h_{a/b}(t)$ is the asymmetry after/before the pulse for helicity h. The final asymmetry is again the difference of the positive and negative helicity asymmetries $A(t) = (A^+(t) - A^-(t))/2$ (Eqn.(2.8)).

In the pulsed rf mode, scanning a frequency range is much faster than in the CW mode. The time spent at each frequency (t_p), determined by the bandwidth $\Delta\omega$, is typically 10 ms - 160 ms, *i.e.* at least 10 times smaller than the CW mode (usually ~ 1 s per frequency). For example, for $t_p = 80$ ms (the repetition rate = 1/80 ms = 12.5 Hz), and frequency steps $\Delta\omega = 200$ Hz, it would take $t_{scan} = 4$ s to sweep a range $\Delta R = 10$ kHz. The frequency sweep is repeated with changing helicities. Each run takes about an hour to accumulate enough statistics. Because the repetition rate is high, the time between rf pulses Δt is short compared to the recovery time τ', therefore the polarization can be approximated to linearly scale with time before and after the rf pulse. However, the sweep time $N\Delta t$ (N–number of pulses in the sweep) is long compared to τ', so that all spins in the given frequency interval have enough time to relax back to equilibrium before the next rf pulse is applied to the same interval. Within the frequency sweep, the frequencies of the rf pulse are generated randomly to minimize history effects.

Because the rf pulse is short in time, the polarization is not very sensitive to beam instability. The instability in the beam will affect one frequency point and not the whole spectrum. There's no power broadening because the rf pulse band width is not greater than the step size. The resulting lineshape is more clearly related to the intrinsic resonance lineshape. The asymmetry is calculated by measuring the difference before and after the short pulse. Therefore the baseline asymmetry is no longer important in this mode, and the scan range could be greatly reduced, which in turn allows for more scans and better averaging. Fig. 2.13 shows a typical pulsed rf mode resonance in MgO. The resonance is fit to one Lorentzian using Eqn. (2.16). Compared to the CW-mode resonance (Fig. 2.11), we scanned a much smaller frequency range and the resonance is much narrower (~ 0.4 kHz).

The pulsed rf mode resonance is particularly important in the high res-
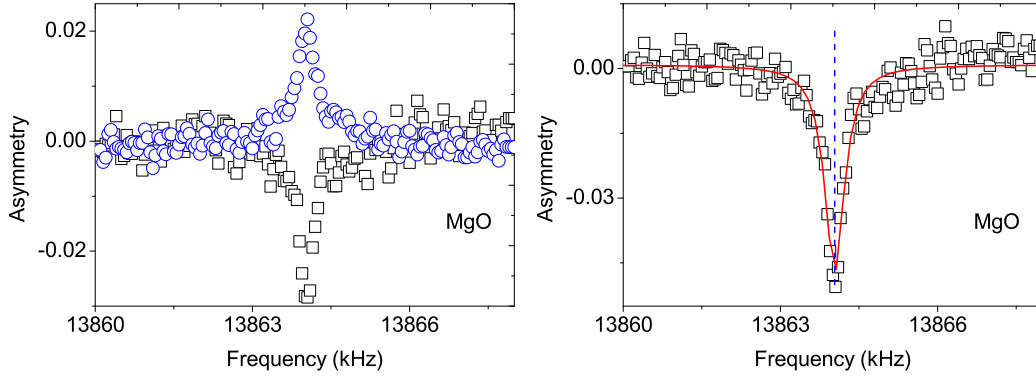
Figure 2.13: Typical pulsed rf mode resonance spectra of ^{8}Li$^+$ in MgO at room temperature in the external magnetic field of 2.2 T. The left panel is the resonance spectra in positive and negative helicities, and the right panel is the combined asymmetry. The spectrum is fit to one Lorentzian using Eqn. (2.16) and linewidth is 0.44 ± 0.04 kHz, much narrower than that in CW mode (Fig. 2.11).

olution measurements when the resonance is narrow. Any resonance with a linewidth on the order of 400 Hz can be accurately measured in pulsed rf mode within a moderate scan time to build up enough signal-to-noise (S/N) ratio. If the resonance is much wider than ~ 400 Hz, the S/N ratio accumulates very slowly so that it takes too long time to get enough data. We will present some high resolution measurement using the pulsed rf mode in Chapters 4 and 3.

2.4.2 β-NMR Spin Lattice Relaxation (SLR) Spectra

β-NMR resonance data senses the static time-averaged possibly inhomogeneous local field at the probe site. In contrast, in a spin lattice relaxation (SLR) measurement, we monitor the polarization of the probes as a function of time in the absence of an rf field. The rate of decay (SLR rate λ) is determined by magnetic fluctuation at the resonance Larmor frequency.

For such measurements, the ion beam is pulsed with an electrostatic kicker such that a pulse of beam of duration t_o is delivered to the sample. The time-dependent β-decay asymmetry is monitored both during and after

the pulse. In all SLR data shown in this thesis, the ion beam is on continuously for 4 s, yielding the sharp change at this time, and then off for a counting period of 12 s. While the beam is on, the measured asymmetry approaches a dynamic equilibrium value determined by the SLR rate λ and the ^{8}Li$^+$ lifetime τ (Eqn. (2.15)). This cycle is repeated many times (typically ~ 30 mins) to accumulate reasonable statistics. The counts from two detectors are used to generate the experimental asymmetry directly proportional to the ^{8}Li$^+$ nuclear polarization $P(t)$ (Eqn. (2.7)). The time-differential spectra are measured in both helicities, averaged over each helicity and then combined to generate the final asymmetry (Eqn. (2.8)).

The spin-lattice relaxation rate $\lambda \equiv 1/T_1$ is extracted from the SLR spectra as follows. Assume a general spin relaxation function $f(t, t'; \lambda)$ for the ions implanted at t'. The average polarization follows[102]:

$$P(t) = \begin{cases} \dfrac{\int_0^t e^{-(t-t')/\tau} f(t,t';\lambda) dt'}{\int_0^t e^{-t/\tau} dt} & t \le t_o \\[2em] \dfrac{\int_0^{t_o} e^{-(t_o-t')/\tau} f(t,t';\lambda) dt'}{\int_0^{t_o} e^{-t/\tau} dt} & t > t_o \end{cases} \tag{2.20}$$

For example, assuming a single mechanism of relaxation with the relaxation rate λ, $f(t, t'; \lambda) = Ae^{-\lambda(t-t')}$, the asymmetry $A(t)$ which is proportional to the polarization $P(t)$ is

$$A(t) = \begin{cases} A_o \dfrac{1-e^{-t/\tau'}}{1-e^{-t/\tau}} & t \le t_o \\[1.5em] A(t_o) e^{-\lambda(t-t_o)} & t > t_o \end{cases} \tag{2.21}$$

where A_o is the maximum β-decay asymmetry at $t = 0$, τ is ^{8}Li lifetime, $\frac{1}{\tau'} = \frac{1}{\tau} + \lambda$ and $A(t_o) = A_o e^{-\lambda t_o}$. During the beam on time, the dynamic equilibrium asymmetry is (Eqn. (2.15)):

$$\overline{A} = \frac{\int_0^\infty e^{-(t-t')/\tau} f(t,t';\lambda) dt'}{\int_0^\infty e^{-t/\tau} dt}$$
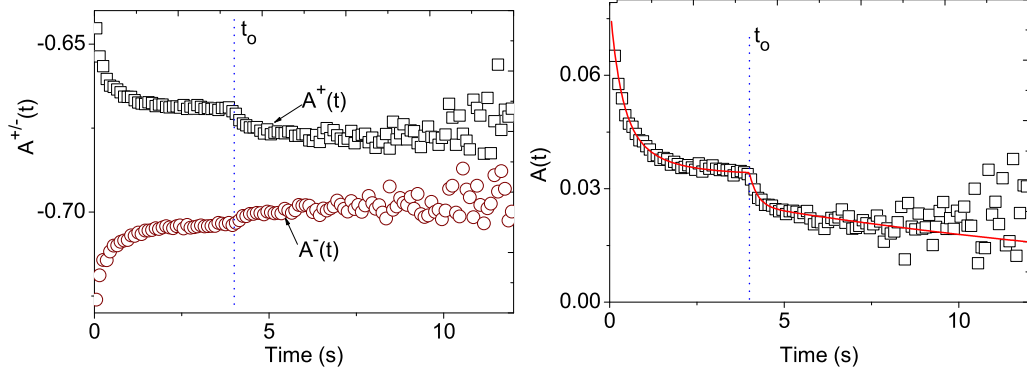
Figure 2.14: Representative SLR spectrum. Left panel: the averaged asymmetry in each helicity. Right: the combined asymmetry. The combined asymmetry is fit to Eqn. (2.21) with one relaxing component (Eqn. (2.23)). The blue dotted line indicates the beam off time.

$$= \frac{A_o}{1 + \lambda\tau} \tag{2.22}$$

and A approaches $\overline{A}$ asymptotically.

In some cases, there is more than one relaxation mechanism, *e.g.* two relaxing components due to an overlayer thin film and its substrate:

$$P(t, t'; \lambda_{sub}, \lambda_{over}) = A_o^{sub} e^{-\lambda_{sub}(t-t')} + A_o^{over} e^{-\lambda_{over}(t-t')} \tag{2.23}$$

where A_o^i and λ_i are the initial amplitude and relaxation rate with $i = sub$ and *over* for the substrate and the overlayer, respectively. We could fit the SLR data to Eqn. (2.21) with the combination of two components (Eqn. (2.23)), and extract the respective relaxation rates. Fig. 2.14 shows a typical SLR spectrum which is taken in Mn doped GaAs in the field of 1.3 T at 50 K. The spectrum of each helicity is shown in the left panel and the combined spectrum is shown at the right. The combined asymmetry is fit to two exponential components using Eqn. (2.23) (the red curve in Fig. 2.14 right). The slow relaxation is assigned to the GaAs substrate and the fast one to the magnetic Mn doped GaAs overlayer (T_C= 72 K). More discussion

on these results are found in Chapter 4.

Chapter 3

The Local Magnetic Field in Crystalline GaAs

GaAs is one of the most widely used semiconductors in both industry and scientific research. As a common impurity in semiconductors, studies of Li in GaAs have a long history[103], but little is known about the NMR of isolated Li in GaAs. Moreover, as one of the best studied semiconductors, GaAs is often used as a substrate, upon which other materials are grown, such as Mn doped GaAs (Chapter 4) and Fe (Chapter 5). GaAs is well lattice matched with Fe (only $\sim 1.4\%$ mismatch) for epitaxial growth of a magnetic Fe overlayer. In order to study such magnetic heterostructures, it is important to understand the behavior of $^8Li^+$ in GaAs bulk crystal as a control study, and this is the topic of this chapter.

The pure GaAs crystal ("undoped" GaAs) does not display either n– or p– type conductivity. Electrons are thermally activated from the valence band to the conduction band, and holes are left in the valence band. Hence electrons and holes are of the same concentration (n = p $\sim 10^6$ cm^{-3} at room temperature). The semi-insulating GaAs used in this thesis is undoped GaAs with a very low intrinsic carrier concentration (n = $\sim 10^7$ cm^{-3}) and very high room temperature resistivity ($\sim 5.7 \times 10^7$ Ωcm) .

The electronic properties and conductivity of GaAs can be changed in a controlled manner by adding very small quantities of other elements – "dopants". In crystalline GaAs, typically the doping process is achieved by adding impurities of Si or Zn to the melt at high temperatures and then allowing it to solidify into the crystal. The GaAs crystal can be changed from semi-insulating to metallic by varying the dopant concentration. For

this metal-insulator transition, we can use the Mott criterion[16] to estimate the critical dopant density N_c at which the metal-insulator transition occurs:

$$a_B^* \cdot N_c^{1/3} \approx 0.24 \qquad (3.1)$$

with $a_B^* = 103$ Å the effective Bohr radius for GaAs[16]. The critical dopant density is estimated to be 1.26×10^{16} cm^{-3}. We expect β-NMR of ^{8}Li$^+$ in GaAs to be quite different from metallic to the semi-insulating GaAs if ^{8}Li$^+$ is sensitive to the mobile carriers introduced by the doping. Moreover, the magnetic proximity effect and spin injection are likely very different for undoped and heavily doped GaAs (Chapter 5).

In this chapter, we first discuss various contributions to the susceptibility of GaAs in Section 3.1, and review the previous β-NMR study on semi-insulating GaAs (published in Ref. [104]) in Section 3.2. In Section 3.3, we report an unexpected shift of the ^{8}Li$^+$ NMR, depending on both temperature and depth, that is revealed by the higher resolution pulsed rf measurements on a different semi-insulating GaAs crystal (sample: 09-B1) and a heavily doped n-type GaAs crystal (sample: 09-B2).

3.1 The Susceptibility of GaAs

The uniform static magnetic susceptibility of a material gives rise to a magnetic field within the material that differs from the applied field. This generally causes a magnetic shift of the resonance, i.e. a frequency shift that scales with the applied field. However, if the susceptibility consists of several contributions, one may be much more strongly coupled to the nucleus than the others. This is the case, for example, in metals, where the Pauli susceptibility yields the Knight shift, which is often the dominant shift. Other contributions to the susceptibility yield the temperature independent orbital (or chemical) shift. Assuming that the resonance shift is proportional to the susceptibility of GaAs, it is necessary to review the magnetic properties of GaAs first before we proceed to the β-NMR results.

GaAs is a diamagnetic solid with a small and weakly temperature-

dependent magnetic susceptibility[105]. Its susceptibility can be decomposed into several components:

$$\chi = \chi_{core} + \chi_{diamag}^{Langevin} + \chi_{paramag}^{van\ Vleck} + \chi_{ionized\ dopants} + \chi_{free\ carriers} \quad (3.2)$$

where χ_{core} is the diamagnetic (negative) susceptibility due to the ion cores (Ga^{3+} and As^{5+}). $\chi_{diamag}^{Langevin}$ is the Langevin contribution to the susceptibility due to the valence band, sensitive to the spatial distribution of the valence electrons in the chemical bonds in this network covalent structure. $\chi_{paramag}^{van\ Vleck}$ is the van Vleck type paramagnetic (positive) susceptibility, which originates from the second order perturbation of Zeeman energy, and inversely proportional to the band gap. The band gap of GaAs is weakly temperature dependent, being 1.43 eV at room temperature while 1.52 eV at low temperatures[15]. $\chi_{ionized\ dopants}$, the contribution from ionized dopants, is diamagnetic and usually considered negligible at all temperatures. $\chi_{free\ carriers}$ is the contribution from free electrons, *e.g.* electrons in the conduction bands in our case.

$\chi_{free\ carriers}$ can be further decomposed into 2 contributions:

$$\chi_{free\ carriers} = \chi_{Pauli} + \chi_{Landau} \quad (3.3)$$

where χ_{Pauli} and χ_{Landau} are the Pauli and Landau susceptibilities of free carriers, respectively. Paramagnetic χ_{Pauli} (spin susceptibility) is usually very small and temperature-independent in a metal because of the Pauli exclusion principle and an electronic density of states that is only weakly dependent on energy in the vicinity of the Fermi level. Only the carriers near the Fermi energy (within $\sim k_B T$) contribute to the susceptibility with a constant density of states near E_F. The net electronic moment leads to an effective field at the probe $^8Li^+$ nucleus. The shift produced by this field in a metal is the famous Knight Shift[15]. As in Eqn. (4.9), the Knight shift δ_{Knight} can be written as:

$$\delta_{Knight} = \left(\frac{A}{N_A \mu_B} \right) \chi_{Pauli} \quad (3.4)$$
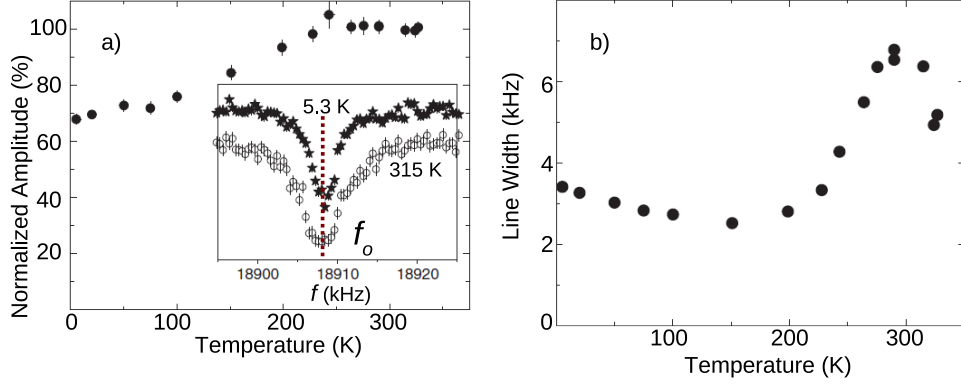
Figure 3.1: Left: the temperature dependence of the amplitude of the β-NMR resonance at the ^{8}Li$^+$ Larmor frequency in GaAs. The inset shows example resonance data for two temperatures, offset for clarity. Right: temperature dependence of the linewidth of the β-NMR resonance in GaAs. Adapted from Ref. [104].

where N_A, μ_B, A are Avogadro's number, the Bohr magneton and the hyperfine coupling constant between the ^{8}Li$^+$ probe and the conduction electrons, respectively. In contrast to a metal, the density of states of free carriers in heavily doped GaAs is no longer a constant as in metals. The electrons freeze out into bound states at the dopant ions at low temperature. Therefore the paramagnetic χ_{Pauli} in n-GaAs changes with temperature. The hyperfine interaction between the ^{8}Li$^+$ probe and the conduction electrons in n-GaAs may lead to a resonance frequency shift like the Knight shift in a metal, but which depends on temperature. The diamagnetic χ_{Landau} is $-\frac{1}{3}\chi_{Pauli}$ in a metal, but is significantly enhanced in semiconductors generally, particularly in n-GaAs, which $\frac{\chi_{Landau}}{\chi_{Pauli}} \propto (\frac{m_e}{m^*})^2$ because of the small effective mass m^* in n-GaAs[15]. χ_{Landau}, as an orbital contribution, is unlikely to strongly couple to ^{8}Li$^+$ nucleus, but it may contribute to an orbital shift.

3.2 Previous β-NMR Study on Semi-Insulating GaAs

Here we summarize previous β-NMR measurements on GaAs[104]. β-NMR because of its sensitivity, has been proved an effective probe to study isolated impurities in semiconductors[106, 107]. Early resonance measurements on GaAs using CW mode were conducted in the presence of a static magnetic field $H_o \sim 3$ T parallel to the $\langle 100 \rangle$ crystal direction. The ^{8}Li$^+$ with full energy was implanted into a ~ 350 μm thick semi-insulating GaAs substrate, stopping at a penetration depth of ~ 140 nm. As shown in the inset of Fig. 3.1 left panel, a single broad resonance with no quassdrupolar splitting is observed at all temperatures, indicating that Li is located at cubic sites (the discussion on the quadrupole splitting is in Section 2.4.1.1). In the Zincblende lattice, that is the interstitial tetrahedral or substitutional site. The resonance does not shift substantially below 300 K. The Left panel of Fig. 3.1 shows the amplitude of the resonance. At high temperatures, all of the Li stay in a high symmetry site, while at low temperatures, about 70% of the Li are in such locations with 30% unaccounted for, possibly in a broad unresolved resonance. The amplitude loss at low temperatures can be attributed to ^{8}Li$^+$ moving out of a high symmetry site as temperature decreases[108, 109]. ^{8}Li$^+$ stopping at sites of lower symmetry in the near vicinity of some lattice disorder experience an EFG (we don't know how big), so the set of all such sites experiences a distribution of EFGs, likely resulting in a broad component in the resonance that is not resolved and a corresponding loss of amplitude in the narrow resonance as observed in the β-NMR in ZnSe[107].

The temperature dependence of the resonance linewidth is shown in the right panel of Fig. 3.1. The power broadening in CW mode $\gamma H_1 \sim 1.3$ kHz (Section 2.4.1.1) contributes to the linewidth (~ 3 kHz) below 200 K. Another contribution to the linewidth is the nuclear dipolar interactions between the static Li and the Ga and As nuclear moments. The linewidth slightly decreases from 5 K to 150 K, followed by a broadening above 150 K. It peaks at about 290 K and decreases again. This peak is likely due to

a site change.

Now let's discuss the possible $^8Li^+$ sites in the GaAs crystal lattice. Fig. 3.2 shows possible sites Li may take in a simple analogous 2D lattice. The substitutional sites and interstitial sites (top panels of Fig. 3.2) are well-defined cubic sites, at which the quadrupole splitting is zero. Some $^8Li^+$ may also stop in the vicinity of implantation-created crystal defects, Frenkel (vacancy–interstitial) pairs (panel c of Fig. 3.2). These are not well-defined high symmetry sites, therefore the quadruple splitting does not vanish and unresolved quadrupole splitting contributes to the resonance linewidth. If the probe $^8Li^+$ stops very close to such a defect (panel d of Fig. 3.2), the EFG may be so large that the corresponding resonance may be too broad to be detected.

An alternate possible explanation for the temperature dependence is $^8Li^+$ diffusion and trapping as has been observed in some materials for the positive muon[110, 111]. The $^8Li^+$ is much more massive than μ^+, so this is unlikely. If there were any fast long-range diffusion of $^8Li^+$, we would expect a dramatic narrowing of the linewidth at high temperatures, as observed in ^7Li NMR[112]. However, as shown in the right panel of Fig. 3.1, the linewidth at 300 K is not substantially narrower than at 5 K. There is no sign of a motional narrowing at high temperatures, therefore the linewidth change can not be attributed to $^8Li^+$ diffusion. It is also possible that $^8Li^+$ diffuses quickly to a trap (in a small fraction of its lifetime 1.2 s). The resonance would thus be characteristic of the trap site instead of pure GaAs. In this case, one would expect to freeze out such a transition at low temperatures. However, we did not observe a dramatic change in the resonance linewidth at low temperatures as shown in the right panel of Fig. 3.1.

Moreover, α emission channeling studies of ^8Li in GaAs[109] show that below 200 K, the tetrahedral interstitial sites (panel b of Fig. 3.2) are preferentially occupied by $^8Li^+$; while substitutional sites (panel a of Fig. 3.2) are occupied above 200 K. In these experiments, a beam of $^8Li^+$ was injected as the probe. $^8Li^+$ decays into an excited state of ^8Be (Eqn. 2.3) which immediately breaks into two α particles. Within a single crystal, these α parti-

cles experience channeling and blocking effect along major crystal axes and planes, resulting in an anisotropic emission yield from the surface, depending on the lattice site of $^8Li^+$ at the same time of decay. The $^8Li^+$ occupation sites were determined by measuring the distribution of α transmission flux parallel to the sample surface. The probes used in these experiments ($^8Li^+$) is the same used in our measurements, therefore their results measured directly the $^8Li^+$ occupation sites in the GaAs lattice. Theory[113] predicts that the equilibrium site for isolated interstitial $^8Li^+$ is the tetrahedral site surrounded by four nearest As atoms, T_{As}. At low temperatures, a significant fraction of the Li ends up in a T_{As} sites with possible occupancy of a T_{Ga} or substitutional site. However, as the temperature is raised above $\sim$ 200 K, the environment around many of the Li ions is changing significantly. These Li approach nearby implantation-created vacancies (Panel c of Fig. 3.2), and the broadening of the resonance (the left panel of Fig. 3.1) may be due to small unresolved quadrupole splittings. At higher temperatures, Li preferentially occupies the Ga vacancy V_{Ga} where the quadrupole splitting is identically zero, and hence the linewidth is observed to decrease again. Similar behavior has been observed in β-NMR of ^{12}B implanted in the II–VI zincblende semiconductor ZnSe[114].

3.3 High Resolution Measurements of β-NMR in GaAs Crystals

The previous studies were carried out in CW mode which is generally subject to power broadening (Section 2.4.1). Higher resolution measurements could be made in pulsed rf mode, which reproduces the intrinsic lineshape more faithfully (Section 2.4.1.2). The rf pulsed mode measurements reveals a small unexpected temperature-dependent shift of the β-NMR resonance in both the semi-insulating GaAs (09-B1) and the heavily Si doped n-GaAs (09-B2). In addition, depth dependence of the shift is observed in the semi-insulating GaAs (09-B1) but not in the n-GaAs (09-B2).
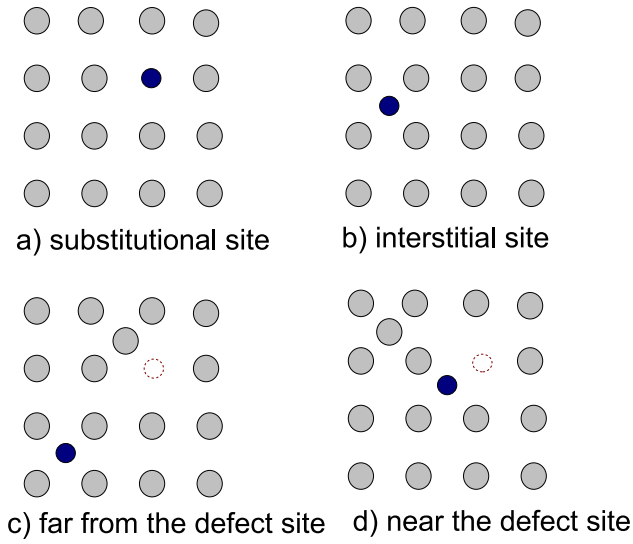
Figure 3.2: Possible sites ^{8}Li$^+$ may take in an analogous 2D lattice. The gray points represent the analogous GaAs 2D lattice, and the blue points represent ^{8}Li$^+$ stopping sites. Panel c and d show ^{8}Li$^+$ sites in the vicinity of a lattice defect, a vacancy-interstitial Frenkel pair. See text for more details.

3.3.1 Experimental

The semi-insulating GaAs is provided by Wafer Technology Ltd., UK in the form of a 3" diameter $\sim 350\mu$m thick wafer grown at low pressure from high purity polycrystalline GaAs in a vertical temperature gradient (VGF – Vertical Gradient Freeze) with one side polished. For the semi-insulating GaAs crystal (09-B1), no compensation dopants are deliberately added to produce the semi-insulating property. The carrier concentration n is in the range of $(2.00–6.30)\times 10^7$ cm^{-3} measured by the provider. The surface is carefully cleaned before delivery and any surface contamination will be bound up in the surface oxide (a native oxide layer $\sim$3 nm thick ideally Ga$_2$O$_3$). The sample used in the experiment is 8 mm $\times$ 10 mm cut from the 3" diameter wafer without any further surface preparation.

The heavily doped n-GaAs crystal (09-B2) is cut from a 3" diameter wafer ($\sim 350\mu$m thick) from AXT Inc., USA, also grown by VGF. It is heavily doped by Si to give n-type conductivity. The carrier concentration n is in the range of $(1.5-1.7)\times 10^{18}$ cm^{-3}, well into the metallic region. The Si dopant is nearly 100 % activated at room temperature, donating one free electron per Si, therefore the dopant concentration N_d is very similar to the carrier concentration n. So N_d in this n-GaAs crystal (09-B2) is much higher than the critical dopant concentration N_c for the metal-insulator transition, therefore 09-B2 is highly metallic. One side of the wafer is polished and the other side is rough but flat, and chemically etched.

The ^{8}Li$^+$ implantation profile is simulated by SRIM-2006.02 (Section 2.3). The energy dependence of the average implantation depth and the width of the distribution are shown in the inset of Figure 3.3. The pulsed rf mode β-NMR spectra in the semi-insulating GaAs crystal (09-B1) were measured in the field of 2.2 T while the same measurements in the heavily doped n-GaAs (09-B2) were taken at 4.1 T.

The resonance spectra are fit to a single Lorentzian using Eqn. (2.16) and the shift is calculated with respect to the frequency of ^{8}Li$^+$ in MgO at 300 K by Eqn. (2.13).

As we discussed in Section 4.4.3, we need to correct for the demagneti-
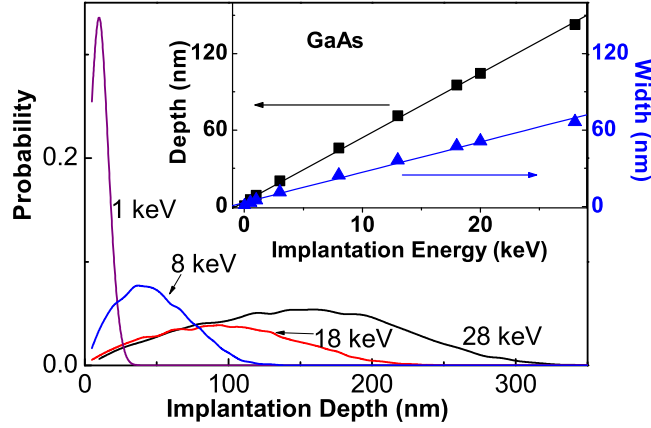
Figure 3.3: SRIM simulation of ^{8}Li$^+$ in the GaAs single crystal. The implantation profiles in GaAs simulated by SRIM-2006.02 with different implantation energies. The implantation energy varies from full beam energy 28 keV to 3 keV, corresponding to the average implantation depth from $\sim$ 140 nm to $\sim$ 20 nm. The inset shows the implantation depth and width with different beam energies.

zation effect in the GaAs[115]. The total field can be decomposed in Eqn. (4.3) where all components are defined the same as in Section 4.4.3. Note that $\nu = \gamma B_{tot}$, the relative shift is:

$$
\begin{aligned}
\delta &= \frac{\nu - \gamma B_o}{\gamma B_o} \\
&= \frac{B_{demag} + B_{Lor} + B_{loc}}{B_o}
\end{aligned}
\tag{3.5}
$$

here $\nu = \gamma B$ is the frequency in MgO. We need to account for B_{demag} and B_{Lor} to obtain the shift of interest $\delta_c = \frac{B_{loc}}{B_o}$. As discussed in Section 4.4.3, $B_{Lor} = 4\pi/3$ for a spherical Lorentz cavity, and the demagnetization field $B_{demag} = -NM$ where the dimensionless demagnetization factor N ranges from 0 to 4π in the cgs system. For a finite size thin film sample, N can be written as:

$$
N \approx 4\pi(1 - \frac{\pi}{2}\xi + 2\xi^2)
\tag{3.6}
$$

where ξ is the aspect ratio of the sample (thickness to transverse dimension).

In the GaAs samples, the GaAs wafer is $\sim 350\mu$m and cut into an 8 mm $\times$ 10 mm plate. Thus $\xi \approx \frac{350\mu\text{m}}{8\text{mm}} = 0.043$. So the demagnetization factor N is estimated as $4\pi \times 0.94$. Substituting these quantities in Eqn. (3.6) and noting that $\chi_v = M/B$ with χ_v the volume susceptibility of GaAs, we obtain that

$$\delta_c = \delta - (-4\pi \times 0.94 + 4\pi/3)\chi_v \times 10^6 \tag{3.7}$$

For example, at room temperature, $\chi_v = -1.32 \times 10^{-6}$ emu/cm^{-3}, the resonance shift we measured in SI-GaAs (09-B1) is -5 ppm. The shift after demagnetization correction is -15 ppm. The fit results after demagnetization correction are shown in Fig. 3.5 (depth dependence) and Fig. 3.7 (temperature dependence).

3.3.2 Results and Analysis

3.3.2.1 Depth Dependence of the Local Magnetic Field in GaAs

The spectra of ^{8}Li$^+$ in the semi-insulating GaAs crystal (09-B1) at 5.5 K in the field of 2.2 T as a function of implantation depth is shown in the top panel of Figure 3.4. The shift at 3 keV (corresponding to the average implantation depth $d \sim 20$ nm) amounts to about -50 ppm relative to the resonance position in crystalline MgO, our standard reference material. The magnitude of the shift is comparable with Knight shifts of ^{8}Li$^+$ in some noble metals[116]. At this temperature, the shift is clearly depth dependent being more negative deeper in the crystal (28 keV, corresponding to $d \sim 140$ nm) than near the surface (3 keV, $d \sim$ 20 nm). Note that the linewidth, however, shows no significant energy dependence.

In contrast, the bottom panel of Fig. 3.4 shows the β-NMR spectra in the heavily doped n-type GaAs crystal (09-B2) at 5 K with implantation energy of 28 keV ($d \sim 140$ nm) and 9 keV ($d \sim 50$ nm) in 4.1 T magnetic field. At the time of this experiment, we could not decelerate ^{8}Li$^+$ down to 3 keV, therefore we measured at 9 keV, the lowest beam energy we could achieve. Both resonances shift negatively compared to MgO (the blue dashed line), but neither the shift nor the linewidth changes significantly as a function of
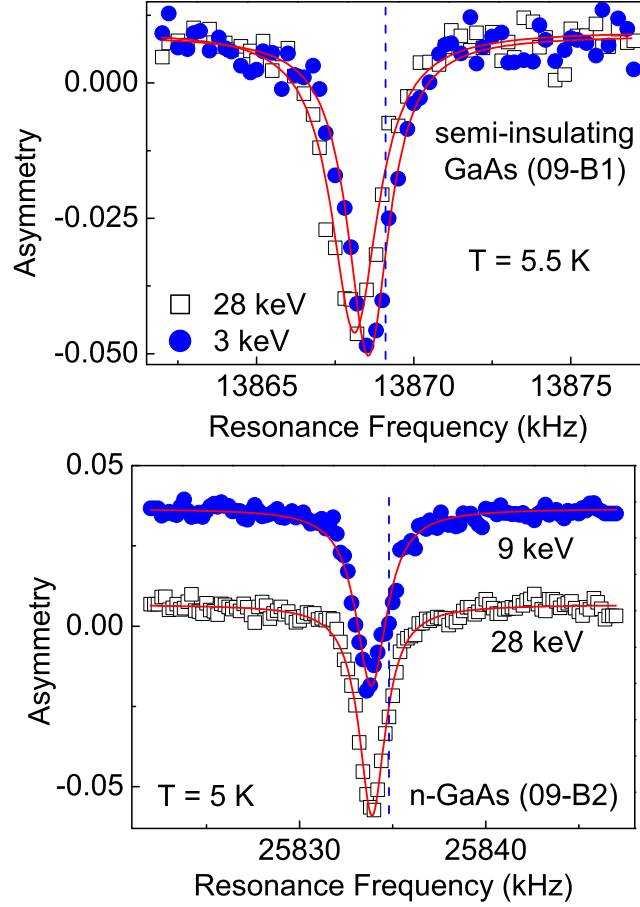
Figure 3.4: Top: β-NMR spectra in of the semi-insulating GaAs crystal (09-B1) in the field of 2.2 T at 5.5 K with implantation energies of 28 keV (black open squares) and 3 keV (blue solid circles). The resonance shifts negatively without broadening as the beam goes deeper into the GaAs crystal.

Bottom: β-NMR spectra of heavily doped n-type GaAs (09-B2) with different implantation energies at 5 K in the presence of an external field of 4.1 T. Although both spectra negatively shift compared to the reference, the frequency shift is not implantation energy dependent and no obvious broadening appears. Spectra are vertically offset for clarity.

In both panels, the blue dashed line is the reference resonance frequency of $^{8}Li^{+}$ in crystalline MgO.
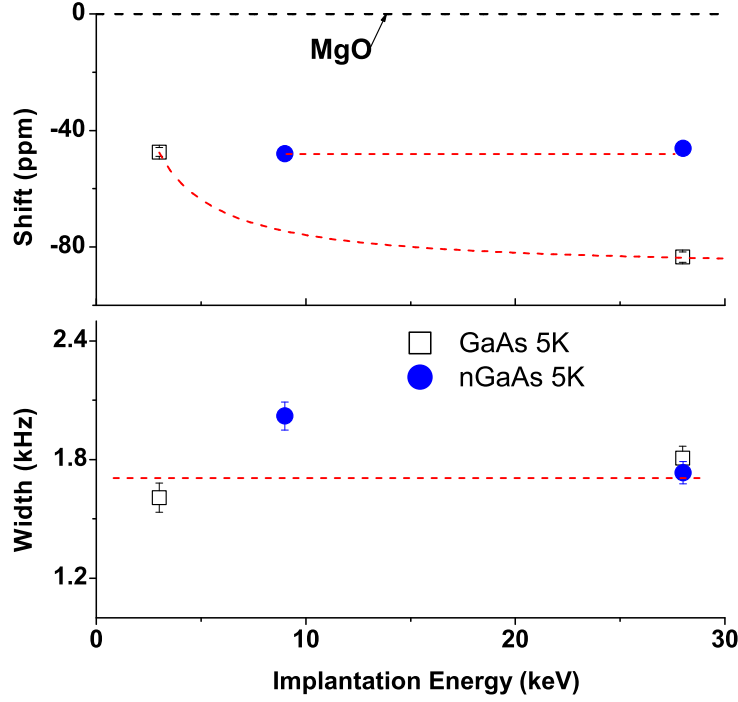
Figure 3.5: Implantation energy dependence of the frequency shift (top) and width (bottom) measured in semi-insulating GaAs (open black squares) and heavily doped n-GaAs (solid blue dots) at 5 K. The black dashed line indicates the ^{8}Li resonance position in MgO.

implantation energy.

Fig. 3.5 summarizes the fit results of the β-NMR spectra in both GaAs crystals as a function of implantation energy. In the semi-insulating GaAs (09-B1), the resonance shift close to the surface ($d \sim 20$ nm) is comparable to the depth-independent resonance shift in the n-GaAs (09-B2), but is more negative when ^{8}Li$^+$ stops in the bulk ($d \sim 140$ nm). The linewidths are ~ 1.8 kHz, comparable in both GaAs crystals at 28 keV ($d \sim 140$ nm). The resonance is slightly broadened at the beam energy of 9 keV (~ 50 nm implantation depth) in n-GaAs (09-B2).

3.3.2.2 Temperature Dependence of the ^{8}Li$^+$ Resonance in GaAs

Now we present the temperature dependence of ^{8}Li$^+$ resonance in both GaAs crystals at 28 keV. Fig. 3.6 shows the resonance spectra at various temperatures in both semi-insulating GaAs (left panel) and heavily doped n-GaAs (right panel) crystals at 28 keV implantation energy – corresponding to an average depth of ~ 140 nm. The fit results are summarized in Fig. 3.7, and the shift is also corrected for the demagnetization effect as discussed above. As evident in the spectra, the resonance does not move at high temperatures, but starts to shift to lower frequencies below 150 K in both samples. The resonance shifts further negative as temperature decreases, saturating at about 10 K (see the first two points in the red circle shown in the top panel of Fig. 3.7). The shift in the heavily doped n-GaAs crystal (09-B2) is smaller in magnitude than in the semi-insulating GaAs (09-B1). Above 150 K, there is still a temperature-independent negative shift in both crystals. The resonance linewidth (bottom panel of Fig. 3.7) is minimum at ~ 150 K and peaks at ~ 240 K. The linewidth is consistent with the value measured in CW mode subtracting the power broadening (Section 3.2).

3.3.3 Discussion

In GaAs, we expected only a small chemical (orbital) shift independent of implantation depth and temperature. So it is really surprising to find depth dependence in the SI GaAs and significant temperature dependence in both SI- and n-GaAs. In this section, we will discuss what this could mean.

The resonance only shifts with the implantation depth in the semi-insulating GaAs crystal (09-B1). This may indicate that the resonance shift is related to the carrier concentration. The periodic structure of chemical bonds in the GaAs crystals is terminated at the surface, resulting in unsaturated (dangling) bonds. These dangling bonds can rearrange themselves and might bond to a (mono) layer of adatoms, *e.g.* oxygen, forming a native oxide layer. The native oxide of GaAs generates states localized at the surface and the energy of these surface states form an energy band in the band
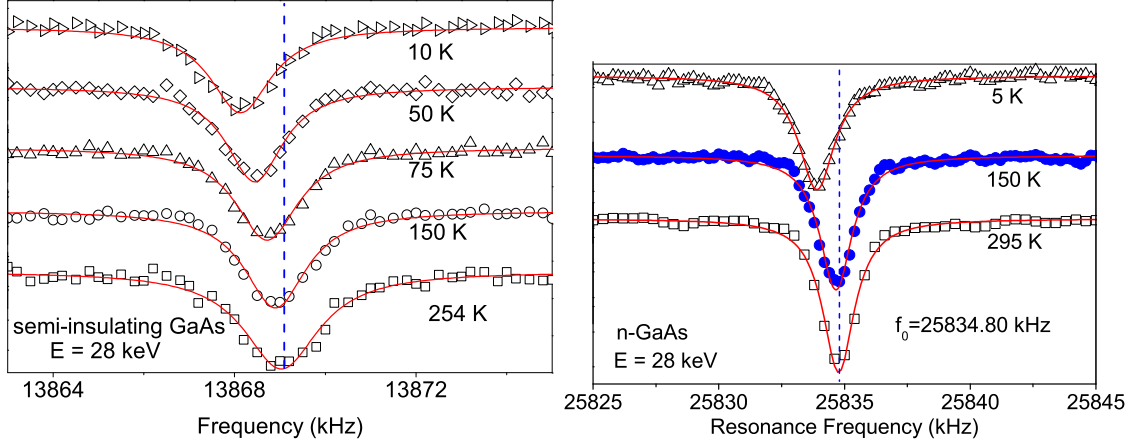
Figure 3.6: β-NMR spectra as a function of temperature in the semi-insulating GaAs (left) and in the n-GaAs (right) crystal. The resonance frequency in both crystals shifts negatively when cooled without significant broadening. Spectra are vertically offset for clarity.

gap with a high density of levels. The Fermi level is pinned about 0.5 eV above the valence band[117]. The electrons in the semiconductor flow into the surface region to match the chemical potential in the surface with the bulk, making the surface negatively charged. The immovable positive ions are left in the near surface region and a thin layer depleted of free electrons is created. The conduction and valence bands bend upwards (for n-GaAs) near the surface region forming a surface barrier[117], just like the Schottky barrier formed at the interface when the semiconductor is in contact with a metal layer. The upward bending of the conduction and valence bands could make the EL2 deep defect level (located ~ 0.8 eV below the conduction band) a possible donor, since for an EL2 level, the emission rate of an electron into the conduction band is sensitive to the electric field[118]. In bulk materials, its concentration is on the order of $10^{16}/\text{cm}^{-3}$[119]. The surface barrier width can be roughly estimated by assuming a uniform charge distribution using Eqn. (1.6). In this case, $e\phi_B$ is the height of the surface barrier ~ 0.52 eV[120]. According to Eqn. (1.6), the band bending results in a barrier width of ~ 100 nm, which is the order of implantation depth.
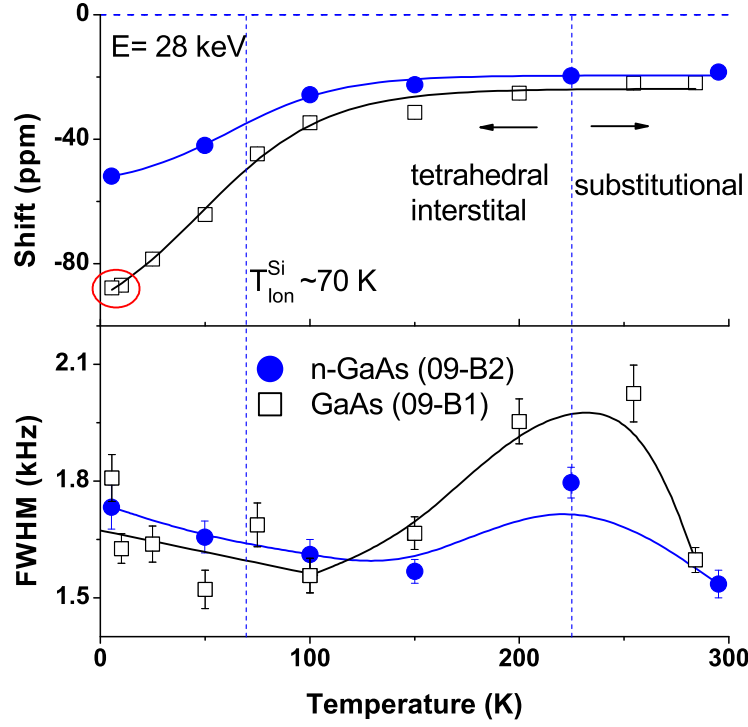
Figure 3.7: Temperature dependence of the frequency shift (top panel) and width (bottom) in semi-insulating GaAs (open black squares) and heavily doped n-GaAs (solid blue dots). The negative resonance shift is small and temperature-independent above 150 K, but increases as temperature decreases below 150 K, saturating at ~ 10 K. Resonance shift in the heavily doped n-type GaAs (09-B2) is prominently smaller than that in the SI-GaAs (09-B1) at low temperature. In contrast to the resonance shift, the resonance linewidth, consistent with the preliminary study, peaks at ~ 290 K and narrows at ~ 150 K.

This may explain the depth dependence of the resonance shift.

Using the same assumption for n-GaAs (09-B2) with a larger carrier concentration $n \sim 1.6 \times 10^{18}$ cm^{-3}, we estimate that the surface barrier width is ~ 20 nm, much narrower than that in the semi-insulating GaAs (09-B1). The detection range (50 nm – 140 nm) is far beyond the surface barrier. Therefore ^{8}Li$^+$ stopping either in the bulk ($\sim$140 nm) or closer to the surface ($\sim$50 nm) see the same magnetic field, and the resonance frequency is depth independent.

Now we consider possible origins for this unexpected temperature dependence of the resonance shift found in both SI-GaAs (09-B1) and n-GaAs (09-B2). First we discuss a number of effects that can be ruled out. 1). The resonance shift can't be due to the field inhomogeneity. The applied field generated by the superconducting solenoid is very uniform at the sample position. The magnetic field difference within 1 cm from the magnet center is less than 3 ppm. The movement of the sample position, *e.g.* the thermal contraction of the cryostat (~ 4 mm from 300 K to 10 K), or the movement of the beam spot (less than the sample size ~ 8 mm$\times$mm), will result in shifts less than 3 ppm, much smaller than the observed shift. 2) One may consider whether this shift is due to some dilute paramagnetic magnetic impurities, like the demagnetization effect in Ga$_{1-x}$Mn$_x$As(discussed in Chapter 4). In this case one would expect the shift to follow Curie's law, i.e. inversely with temperature. This is evidently not the case as such a shift would double going from 10 K to 5 K, in contrast to the observed constant value below 10 K (the first two open black squares in the top panel of Fig. 3.7). 3). The shift might be related to the temperature dependent bulk susceptibility of GaAs, either by the demagnetization field or by a local hyperfine field. However, the susceptibility χ of GaAs is weakly temperature dependent[105]. At $T = 10$ K, it only changes by $\sim 1\%$ from the room temperature value (-1.32×10^{-6})[121]. The demagnetization correction due to the GaAs magnetization (similar to the analysis in Section 4.4.3) is estimated to be ~ 17 ppm, and very weakly temperature-dependent. So the observed shift is not the demagnetization effect of GaAs.

Ruling these out, now we discuss what possibilities remain. There is a

temperature-independent negative shift above 150 K in both undoped and heavily doped GaAs. This is consistent with ^{71}Ga NMR shift measurements [122, 123]. In Ref.[122], Fistul *et al.* find the ^{69}Ga shift increases at low temperature in both undoped GaAs crystal (the carrier concentration $n = 1.5 \times 10^{16}$ /cm^{-3}) and p-type GaAs doped ($p \sim 10^{12}$ /cm^{-3}). They excluded the conduction electrons as the source of the shift because of the low carrier concentration. In our case, the carrier concentration in the semi-insulating GaAs is so low ($n \sim 10^7$ /cm^{-3}) that a Knight shift also seems unreasonable. However, band bending may change the carrier concentration near the surface, making the Knight shift possible. As already discussed in Section 3.1, χ_{Pauli} from conduction electrons may depend on temperature in GaAs and lead to a temperature dependence of β-NMR resonance shift analogous to the Knight shift in metals.

The temperature dependence of the shift in GaAs (Fig. 3.7) appears to be activated with an activation energy comparable to shallow donors like Si ($E_i = 5.8$ meV[124], corresponding to a temperature of ~ 70 K). This suggests that, surprisingly, there is a contribution to the shift from free carriers. This is surprising because the carrier density is so low. Despite this, let's consider the possibility that there is a contribution from the free carrier. In a simple picture, the shift may consist of two parts (as shown in Fig. 3.8):

$$\delta = \delta_d + \delta_p \tag{3.8}$$

where δ_p is a positive shift, analogous to a Knight shift in metal, associated with the free carriers. It exhibits an activated temperature dependence, but it may also contain a constant part in the metallic sample. δ_d, on the other hand, is a diamagnetic temperature independent shift likely connected with the overall diamagnetism of GaAs, *i.e.* an orbital shift.

Now let's consider this possibility further. In the semi-insulating GaAs (09-B1) with such low carrier density (10^7 cm^{-3}), impurities such as Si form isolated energy levels below the conduction band. Some electrons in the impurity levels could be thermally excited to the conduction band. The thermally excited carriers contribute to χ_{Pauli} which may be related to the
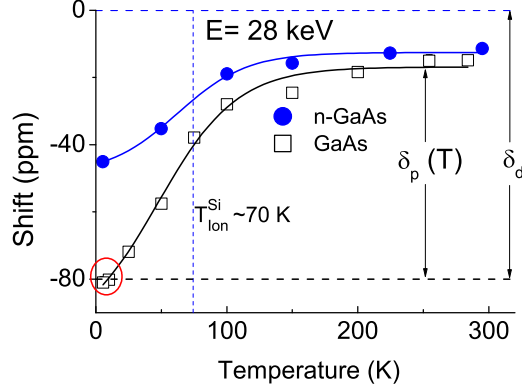
Figure 3.8: The resonance shift may be decomposed into two part: a positive shift $\delta_p(T)$ related to the free carrier, and the temperature-independent negative shift δ_b.

resonance frequency shift δ_p. At high temperatures, both χ_{Pauli} and χ_d contributes to the resonance shift, generating a positive shift δ_p and a negative shift δ_d. At 150 K, the electrons start to localize in the impurity levels and χ_{Pauli} starts to decreases as the carrier concentration decreases. Considering the temperature independent δ_d contributed by χ_d, the total resonance shift is getting more negative with temperature decrease. Below 10 K, the electrons are fully localized in the impurity levels, no electrons can be thermally excited to the conduction band. δ_p completely disappears, and there is only the temperature-independent χ_d contribution to the resonance shift ($\delta_d \sim -80$ ppm). The total shift is saturated below 10 K.

For the metallic n-GaAs (09-B2), the carrier concentration on the order of $\sim 10^{18}$ cm^{-3} is so high that the impurity band is formed due the heavily doped Si and merged with the conduction band, making the n-GaAs crystal metallic. At ~ 70 K, the Si donors start to freeze and the conduction electron concentration decreases as temperature decreases. However, there are still conduction electrons at low temperatures because of the impurity band formed by the high Si doping. Using the saturated shift at low temperatures in semi-insulating GaAs (09-B1) as δ_d in the heavily doped n-GaAs (09-B2), the positive shift δ_p observed in n-GaAs (09-B2) is ~ 70 ppm at

room temperature, and ~ 35 ppm at 5 K, on the same order of the Knight shift observed in the noble metal gold.

One can roughly estimate Pauli susceptibility in the heavily Si doped n-GaAs (09-B2) using $\chi_{Pauli} = \mu_B^2 g(E_F)$[15] with $g(E_F)$ the density of states at Fermi energy E_F. In the free electron case, valid in the highly metallic n-GaAs, $g(E_F) = \frac{3n}{2E_F}$ at $T = 0$. Pauli susceptibility is roughly estimated to be 0.026×10^{-6} emu/cm^3, which is much smaller than Pauli susceptibility in Au. Pauli susceptibility of Au is $\chi_{Pauli} = 1.21 \times 10^{-6}$ emu/cm^3, and the Knight shift of ^{8}Li$^+$ in Au is measured to be $+73(5)$ ppm for the substitutional site and $+141(4)$ ppm for the octahedral interstitial sites[116]. However, considering the fact that χ_{Pauli} in n-GaAs (09-B2) estimated above is two orders of magnitude smaller than χ_{Pauli} in Au, the coupling constant A_{HF} would also need to be two orders of magnitude larger (which seems unreasonable) unless the carrier content is quite drastically different near the surface.

We have no clear explanations for the observed temperature dependent shift in GaAs, but the detailed shift is somewhat sample dependent, so it may be controlled by other factors which we may not control, such as the native oxide on the surface and the surface preparations done by the provider. A clearer picture could be obtained by testing more carefully prepared samples. This would be best done using a GaAs layer grown by MBE on commercial GaAs wafers with a better surface quality control.

3.3.4 Summary

In summary, pulsed rf β-NMR provides higher frequency resolution for studying the magnetic properties of GaAs. A resonance frequency shift is observed in both SI-GaAs (09-B1) and n-GaAs (09-B2) as a function of temperature. It does not exhibit a Curie temperature dependence, but saturates below 10 K. The resonance shift is likely a combination of temperature-independent δ_d and temperature dependent Knight shift δ_{Knight}. It moves as a function of implantation depth only in SI-GaAs (09-B1). The depth dependence suggests it may be related to surface barrier due to the band-bending.

Similar temperature dependence of the resonance shift was observed in two commercial GaAs crystals from independent sources. This may indicate that the resonance shift is intrinsic to GaAs. However, the resonance observed in the control experiment on n-GaAs (10-B1) (Section 5.2.2) provided by the same company as SI-GaAs (09-B1) shifts to a higher frequency as temperature decreases, in the opposite direction of what is observed in this chapter. Moreover, a careful examination of the resonance in the substrate of $Ga_{1-x}Mn_xAs$ which is MBE grown pure GaAs on commercial SI-GaAs wafer, does not show a similar temperature dependence (Section 4.4), remaining a constant within error bars. The small temperature-independent negative shift of the resonance above 150 K seems an intrinsic property of GaAs crystals. However, below 150 K, the magnitude and the direction of the resonance shift are sample dependent.

In contrast, the temperature dependence of the resonance width in all GaAs samples is consistent. It is intrinsic to the GaAs crystals that the resonance linewidth is minimum at ∼ 150 K and peaks at ∼ 250 K.

Regardless of the source of this shift, these control measurements establish the baseline behavior of the $^8Li^+$ probe in GaAs from which we can assess the effects of proximity to a ferromagnetic layer of Fe and of an injected current from this layer in Chapter 5. This is primarily important for the results presented in Chapter 5. The resonance observed in $Ga_{1-x}Mn_xAs$(Chapter 4) has a shift orders of magnitude larger and is much broader, so that we can neglect the tiny shift in the GaAs substrate and concentrate on the resonance in the magnetic $Ga_{1-x}Mn_xAs$ layer.

Chapter 4

β-Detected NMR of Li in $\mathrm{Ga}_{1-x}\mathrm{Mn}_x\mathrm{As}$

4.1 Introduction

As discussed in Section 1.2.1, it is widely accepted that ferromagnetism in the dilute magnetic semiconductor $\mathrm{Ga}_{1-x}\mathrm{Mn}_x\mathrm{As}$ is driven by coupling between local Mn^{2+} $S = \frac{5}{2}$ moments mediated by delocalized holes [24, 28]. However, there is a controversy over the properties of delocalized holes for the highest T_C compositions—the valence band model vs. the impurity band model. It is thus important to elucidate the magnetic properties of the itinerant holes. Some information can be gleaned from tunnelling spectroscopy in specially designed heterostructures[37, 125], while magneto-optical studies probe the polarization of the carriers and their hybridization with the local moments[126, 127]. However, a complementary, atomically resolved probe such as nuclear magnetic resonance (NMR) would provide a more complete picture of the magnetic properties at the atomic level. In this context, NMR senses the average hole contribution through a shift of the resonance, analogous to the Knight shift in a paramagnetic metal[99]. As the material is intrinsically inhomogeneous, an atomically resolved probe also reveals the associated magnetic inhomogeneity, through broadening and structure of the resonance line, for example, in the controversial proposal of magnetic phase separation[50, 51, 52] (more discussions in Section 4.6).

As discussed in Section 1.2.1, $\mathrm{Ga}_{1-x}\mathrm{Mn}_x\mathrm{As}$ is only available in the form of thin films. Because of signal limitations, conventional NMR cannot generally be used for thin films, but when NMR is detected by the anisotropy of

radioactive beta decay (for a β-radioactive NMR nucleus), it is possible to overcome this limitation. In this chapter, we use an implanted spin-polarized beam of $^8\mathrm{Li}^+$ to study a 180 nm thick epitaxial film of $\mathrm{Ga}_{1-x}\mathrm{Mn}_x\mathrm{As}$ with $x = 0.054$ ($T_\mathrm{C} = 72$ K) using β-NMR.

All measurements were carried out in a field of 1.33 T applied normal to the sample surface. Note that the easy magnetization axis of $\mathrm{Ga}_{1-x}\mathrm{Mn}_x\mathrm{As}$ is in the plane. A field of 1.33 T is strong enough to rotate the magnetization out of plane and to polarize it along the field. This value of the field was chosen as it allowed a good beam spot. Moreover, this field was found to represent a good compromise in that the magnetic shift of the signal in the Mn doped layer was measurable, while the magnetic broadening and relaxation were not excessive.

One of the major advantages of β-NMR using a low–energy ion beam is the possibility to vary the implantation energy by electrostatic deceleration and thus probe the sample as a function of depth (Section 2.2 and 2.3). Such a depth dependent study in a thin film of $\mathrm{Ga}_{1-x}\mathrm{Mn}_x\mathrm{As}$ at 50 K (below T_C) is discussed in Section 4.3.

Section 4.4 presents both resonance (in pulsed rf mode) and spin lattice relaxation data as a function of temperature in the current $\mathrm{Ga}_{1-x}\mathrm{Mn}_x\mathrm{As}$ thin film. Only in a few cases has β-NMR been carried out in a ferromagnet[128, 129]. Since this is the first example in a disordered ferromagnet, it was not clear, prior to the experiment, whether the $^8\mathrm{Li}^+$ spin relaxation would be slow enough, or the resonance narrow enough, to be able to follow it through the magnetic transition; however, the signals are clearly observable, and the results afford a novel local–probe view of the magnetic state in this important dilute ferromagnet.

The discovery of magnetism in Mn doped GaAs[20], has propelled the field of dilute magnetic semiconductors (DMS) into an extremely active branch of material science over the past decade. Despite extensive investigations, the origin and control of ferromagnetism in $\mathrm{Ga}_{1-x}\mathrm{Mn}_x\mathrm{As}$ are still controversial. There is still a debate if $\mathrm{Ga}_{1-x}\mathrm{Mn}_x\mathrm{As}$ is magnetically phase separated at low temperature[50, 51, 52]. In Section 4.6, we use low–energy spin–polarized $^8\mathrm{Li}^+$ as a local magnetic probe to seek evidence for magnetic

phase separation in GaAs:Mn.

4.2 Sample Preparation and Characterization

The 180 nm $Ga_{1-x}Mn_xAs$ film was grown by MBE on a 8.5 mm $\times$ 6.5 mm semi–insulating (100) GaAs single crystal substrate in a Riber 32 R&D molecular beam epitaxy system and subsequently annealed at 280 ^{o}C for 1 hour. More information on the epitaxial growth can be found elsewhere[27]. Low field SQUID magnetometry was used by the grower to determine T_C= 72 K, and the Mn site occupancies were determined by c–PIXE and c–RBS to be 74.5% of Mn at Ga substitutional sites, 21.5% Arsenic interstitial sites, and 4% in nonspecific "random" sites[29]. Transport measurements indicate this film is metallic with low temperature resistivity $\sim$ 30 mΩ-cm. We independently measured the volume magnetization M at 1.33 T using SQUID at AMPEL. The resulting magnetic moment was then corrected for substrate and sample holder contributions and converted to the average volume magnetization using the nominal film thickness (180 nm), as shown in Fig. 4.1. $M(T \rightarrow 0)$ is on the order expected for full polarization of Mn local moments for the known Mn concentration and thickness. More discussions on the magnetization are in Appendix B. The magnetization M is the order parameter in the ferromagnet[130]. However, because of the high field, M is nonzero even above T_C, erasing the symmetry distinction between the ferromagnetic and paramagnetic phases. So the sharp phase transition point T_C disappears and the transition is "smoothed out". Instead of the sharp discontinuity, M changes gradually through T_C[130, 131]. Analysis of $M(T)$ and other thermodynamic quantities using magnetic equations of state[132] and other methods can still be used to determine T_C in field (B). In simple ferromagnets, $T_C(B)$ is generally an increasing function of B, *e.g.* the case of Gd[133].

Implantation profiles of the $^8Li^+$ as a function of beam energy (shown in Fig. 4.2) were performed using the SRIM-2006.02[134] Monte Carlo code based on 10^4 incident ions. Predicted profiles have been found to be reliable for light ions at low energies in a few detailed comparisons[135, 136]. At the
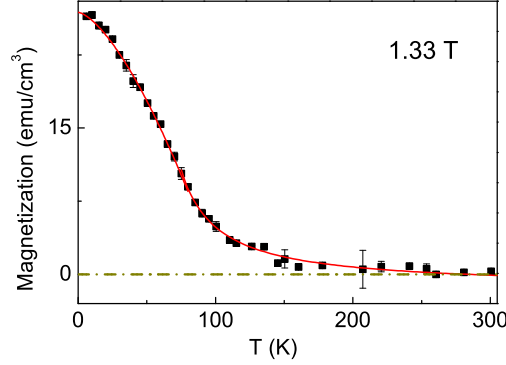
Figure 4.1: The temperature dependence of volume magnetization M at 1.33 T field. The magnitude of $M(T \to 0)$ is of the order expected for full polarization of the Mn local moments for the known Mn concentration and thickness.

highest energy (28 keV), near 30% ^{8}Li$^+$ stops in the substrate, while at 8 keV (Fig. 4.2b), all the ^{8}Li$^+$ should stop in the overlayer, and no substrate signal should be apparent.

Because of the sensitivity of the β detection, relatively few ions are required for the measurement. The total implanted fluence of ^{8}Li$^+$ (in ~4 days of measurement) was on the order of 10^{12}/cm^2. Comparison with the effects of much higher energy ions indicates we can expect little or no net effect of the implantation on the macroscopic properties of the sample[137]. This is confirmed by the fact that we found no time dependence in the results over the course of the experiment and between runs on the same sample[138].

4.3 The Depth Dependence of the Local Magnetic Field in Epitaxial GaAs:Mn

In this section, we present β-NMR results of the ^{8}Li$^+$ implanted in a Mn doped GaAs heterostructure, including both resonance (in pulsed rf mode) and spin lattice relaxation results as a function of implantation energy at 50 K (below T_C=72 K). Below T_C, the Ga$_{1-x}$Mn$_x$As overlayer is in the
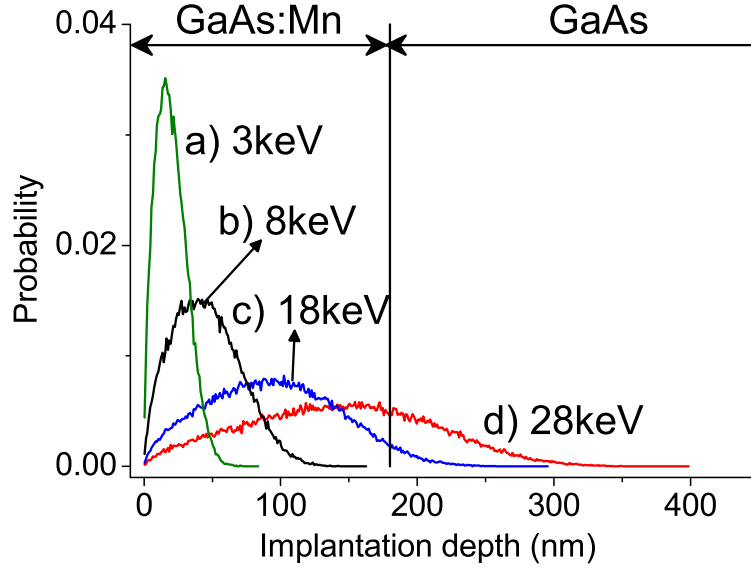
Figure 4.2: The ^{8}Li$^+$ implantation profiles of ^{8}Li$^+$ in Ga$_{1-x}$Mn$_x$As for various energies simulated by SRIM-2006.02.

ferromagnetic state, in which both β-NMR resonance and spin dynamics are very different from the semi-insulating GaAs substrate. We expect a significant contrast between the two layers.

4.3.1 Results and Analysis

Fig. 4.3 shows the β-NMR frequency spectrum in the pulsed rf mode observed in the GaAs:Mn/GaAs sample for various implantation energies between 3 keV and 28 keV at 50K (below T_C). The observed spectrum consists of two lines, one narrow (width consistent with semi-insulating GaAs) and one much broader and centred at a lower frequency. By examining the systematic dependence of this composite spectrum on implantation energy, we can assign the main resonance in the 28 keV spectrum (the cyan dots in Fig. 4.3) to the GaAs substrate, as its linewidth is close to that in undoped GaAs[104], and its amplitude decreases upon deceleration of the ^{8}Li$^+$. Remarkably, as the beam is decelerated, we find a broad, but clearly resolved, resonance

(*e.g.* the green triangles in Fig. 4.3) shifted to lower frequency, which we assign to the ferromagnetic $Ga_{1-x}Mn_xAs$ overlayer. The amplitude of the substrate signal diminishes sharply as the beam energy decreases from 28 keV, indicating that the fraction of $^8Li^+$ stopping in the substrate is decreasing. However, both peaks can still be clearly observed when the beam energy is 8 keV (the green triangles in the small right panel of Fig. 4.3), while the broad peak becomes predominant at 3 keV implantation energy (the black squares in Fig. 4.3). We fit the pulsed rf resonances to the function consisting of two Lorentzian components (Eqn. (2.17)). In this case, $i = mag$ and sub denotes the broad line in the magnetic $Ga_{1-x}Mn_xAs$ overlayer and the narrow substrate resonance, respectively. The product of amplitude and width can be approximated as a measure of the peak area.

The fit results show that the negatively shifted resonance observed in the overlayer is centred at -770(20) ppm relative to the substrate signal, a shift comparable to Knight shifts of ^8Li in ferromagnetically enhanced paramagnetic metals[139, 140]. Like the Knight shift, this shift represents a direct measure of the average spin polarization of the mobile holes, a quantity whose field and temperature dependence is of great interest. We will follow its temperature dependence in Section 4.4 below.

Spin lattice relaxation (SLR) data at 50 K are shown in Fig. 4.4. The asymmetry relaxes from the same initial value at both energies. After 8 seconds, the asymmetry in Fig. 4.4a decreases to about 50% of its initial value, while in Fig. 4.4b the asymmetry drops to only 25% , indicating a faster relaxation rate of $^8Li^+$ in the overlayer. The data are fit to a biexponential spin relaxation function (Eqn. (2.23)) convoluted with the 4 second beam pulse[141]. In this case, $i = sub$ and mag represents the GaAs substrate and the $Ga_{1-x}Mn_xAs$ overlayer. Note that the SLR data start at the same initial point, showing no indication of a missing fraction at 50 K in the Mn doped layer. This is rather remarkable as some of the ^8Li will stop in the near vicinity of Mn moments ($5\mu_B$ for Mn^{2+}, $4\mu_B$ for Mn^{3+}[20]) and experience large fields. However, the SLR data show that even these $^8Li^+$, though they may not contribute to the broad line, do not relax very quickly at 1.33 T.
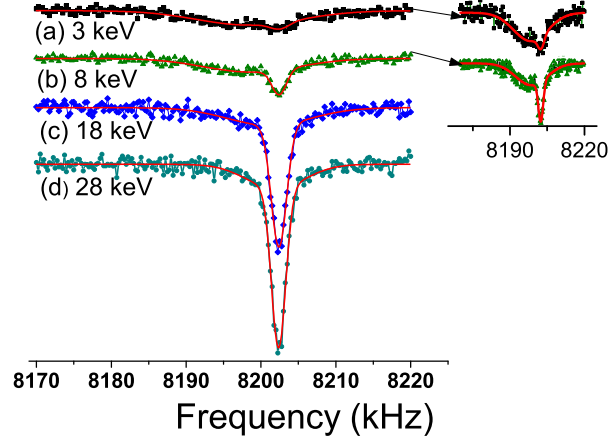
Figure 4.3: Implantation energy dependence of the pulsed βNMR spectrum at 50K, below the Curie temperature (72K). The narrow resonance is characteristic of the semi-insulating GaAs substrate. The broad line associated with the overlayer is negatively shifted by $\sim$5kHz. The small panel on the right is the spectrum at low implantation energies shown in a smaller scale. All spectra offset for clarity.
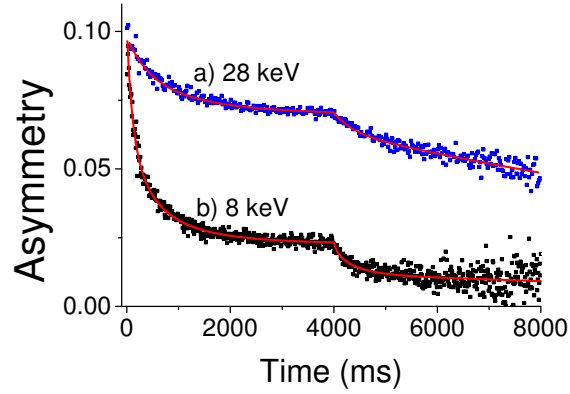
Figure 4.4: Spin Lattice Relaxation (SLR) spectrum at 50K, below the Curie temperature (72K), during and after a 4 second pulse of beam. Li in the magnetic overlayer relaxes much faster than in the nonmagnetic GaAs substrate.

As we already discussed in Section 2.4.1, to understand the implantation energy dependence of the resonance amplitudes, we must consider the spin-lattice relaxation as it determines the maximum resonance amplitude (Eqn. (2.15)). In a simple model of the heterostructure, we have two single exponential relaxation rates λ_{sub} and λ_{mag} for the substrate and the overlayer. Assume that the optical polarizer produces ^{8}Li$^+$ of polarization P_0, according to Eqn. (2.15), the dynamic equilibrium value of the polarization is

$$\bar{P} = \frac{P_o f_{sub}}{1 + \lambda_{sub}\tau} + \frac{P_o(1 - f_{sub})}{1 + \lambda_{mag}\tau}, \tag{4.1}$$

where f_{sub} is the fraction of the ^{8}Li$^+$ stopping in the substrate and is energy dependent. The approach to $\bar{P}$ during beam on period (during time 0-4s) is clearly evident in Fig. 4.4. The maximum resonance amplitude is determined by this "baseline" asymmetry under constant beam rate, meaning that if the substrate and overlayer have significantly different spin relaxation rates, one must scale by the ratio of the relaxation rates to get a comparable measure of the amplitude.

Based on Eqn. (4.1), we multiply the broad resonance area associated to the magnetic overlayer by $(1 + \lambda_{mag}\tau)/(1 + \lambda_{sub}\tau)$ to account for the fast relaxation in the magnetic thin film layer. The sum of the two resonance peak areas are normalized to 1, and each peak area is accordingly normalized to obtain a measure of f_{sub} and $f_{mag} = 1 - f_{sub}$. The normalized peak area of each component is a measure of the fraction of ^{8}Li$^+$ stopping in the associated layer.These are plotted in Fig. 4.5 and compared to the SRIM prediction.

4.3.2   Discussion

The broad line observed in the magnetic $Ga_{1-x}Mn_xAs$ overlayer is surprising. Since the heterovalent Mn dopants must locally break cubic symmetry, ^{8}Li that stop in sites immediately adjacent to Mn will experience such strong local magnetic fields, and fast spin relaxation, that they will not likely contribute to the observed resonance. Such ^{8}Li$^+$ will also experience the largest electric field gradients, and hence the largest quadrupolar splittings. Cubic
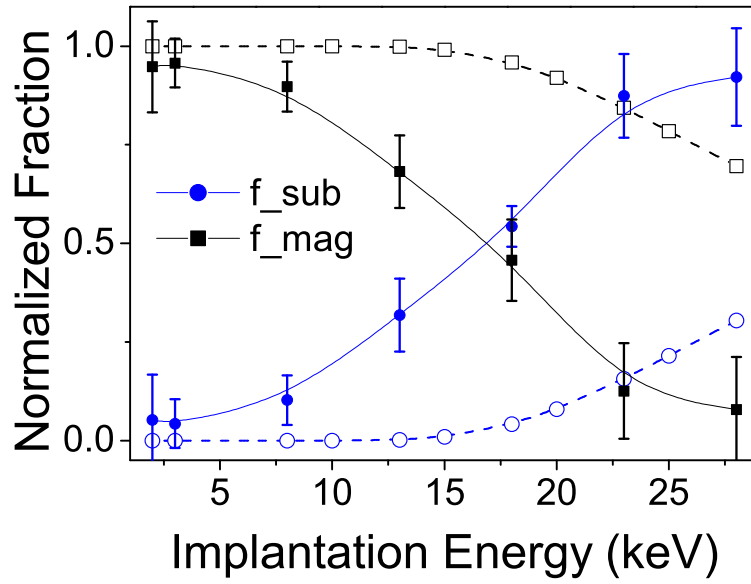
Figure 4.5: The portion of Li stopping in the GaAs substrate (circles) compared with that stopping in the magnetic overlayer (squares). Open and solid symbols are SRIM simulation and the experimental results at 50 K, respectively.

symmetry will be restored upon averaging over all sites, but a distribution of unresolved quadrupolar interactions may contribute to the width of the resonance (Section 2.4.1).

Fig. 4.5 clearly shows that there is **disagreement** between the data and the SRIM simulation, with the substrate fraction always exceeding the predicted value. For example, according to the simulation, all the Li should stop in the overlayer at 8 keV (Fig. 4.2b, while there is a clear sharp peak in the experimental spectrum (Fig. 4.3b, showing that as much as $\sim 15\%$ of the ^{8}Li$^+$ experiences a substrate-like environment at this energy.

We now discuss possible origins of the discrepancy between the implantation energy dependence of the resonances and the SRIM prediction. First we note that the thickness of the overlayer is accurate to better than 10% from calibrations of the growth rate. Similarly, the film is expected to be uniformly thick even over the mm size of the beam spot, so neither an overestimate of the film thickness, nor bare patches of substrate are likely origins for the inconsistency. One possible explanation is that the overlayer is not microscopically homogeneous, i.e. it may contain Mn deficient regions. Yu *et al.* have argued that Mn_I out-diffuses and forms a Mn-rich oxide layer on the surface, leaving Mn depleted regions behind[27]. Another possibility is that the overlayer, though ferromagnetic, is magnetically phase-separated into regions that remain paramagnetic (Mn moments fast fluctuating) and magnetically frozen regions[50]. However, both models have difficulty explaining the occurrence of *two distinct environments* instead of a continuous range. The nonmagnetic (or Mn deficient) regions must be rather large (so that their boundaries account for at most a small fraction of the area), but rather sparse (since the fraction is small), which seems unlikely. The clearest source for two well-resolved environments is the engineered inhomogeneity in the growth direction which has a single sharp boundary. In this regard, we note that the SRIM prediction may significantly underestimate the stopping range since the $\langle 100 \rangle$ direction in GaAs is a *channeling direction* (Section 2.3). It is known that implanted ions can penetrate much further in specific crystal directions where there are long open channels in the structure[142] and SRIM does not account for this[94]. SRIM is expected to be accurate to

the level of a few percent over a wide range of implantation conditions[143], but, this is not so well tested at the relatively low energies used here. We will come back to the magnetic phase separation problem later in Section 4.6.

In summary, we find both spin lattice relaxation and resonance signals of $^8Li^+$ in $Ga_{1-x}Mn_xAs$ in the ferromagnetic state at 50 K and in the GaAs substrate. Two resonances are clearly resolved in the pulsed rf mode resonance data. The narrow resonance is associated from the GaAs substrate, and the other one from the magnetic $Ga_{1-x}Mn_xAs$ overlayer is much broader and negatively shifted to a lower frequency. We also observe two relaxing components in SLR data. The fast relaxing component is assigned to the magnetic $Ga_{1-x}Mn_xAs$ layer, and the slower relaxation to the GaAs substrate. An unexpected implantation energy dependence is found in the pulsed rf mode resonance, with a substrate signal persisting down to low implantation energies. We attribute this to implantation channeling of ^8Li. This could be tested by rotating the sample by a small angle, so that the probe $^8Li^+$ are not incident along the GaAs channeling direction $\langle 100 \rangle$. In this case, the amplitude of the narrow resonance should be greatly reduced if it is the signal from the substrate. However, this would require a new sample holder that would allow the sample to be rotated. We will follow the evolution of the signal in $Ga_{1-x}Mn_xAs$ in temperature in next section.

4.4 Temperature Dependence of in $Ga_{1-x}Mn_xAs$

Following the last section, we study the β-NMR spectra of $^8Li^+$ in the $Ga_{1-x}Mn_xAs$ thin film at 8 keV implantation energy as a function of temperature across the ferromagnetic transition. Both pulsed rf resonance and spin lattice relaxation data are presented and the magnetic properties of the $Ga_{1-x}Mn_xAs$ film are discussed. Since this is the first study on the temperature dependence of β-NMR resonances through T_C in a ferromagnet, it will be an important reference point to compare with other ferromagnets.
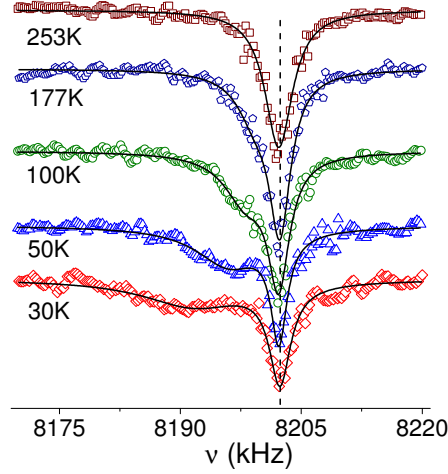
Figure 4.6: Temperature dependence of the β-NMR spectra (vertically offset for clarity) of $^8Li^+$ in $Ga_{1-x}Mn_xAs$ with the implantation energy of 8 keV. ^8Li in the substrate produces the narrow resonance while the broad resonance originates in the $Ga_{1-x}Mn_xAs$ overlayer (See Section 4.3).

4.4.1 Resonance Spectra

The resonance spectra of $^8Li^+$ at 8 keV implantation energy and 1.33 Tesla are shown for various temperatures in Fig. 4.6. At 50 K, the spectrum is the same as that reported in Section 4.3[144], with both broad (overlayer) and narrow (substrate) resonances. There is no evidence of quadrupolar splittings in any of the spectra[145], consistent with the cubic $^8Li^+$ sites known in GaAs (See 3.2).

At the highest temperature, the two resonances are unresolved, and there is no evidence of the broad peak. But as T is reduced, the broad line shifts out of the narrow resonance and broadens continuously, becoming too broad to observe with the limited radio frequency (rf) magnetic field of the broadband spectrometer (amplitude, $H_1 \leq 100\mu T$) below about 30 K. In dilute magnetic alloys, the lineshape is expected to be approximately Lorentzian, though for concentrations at the level of a few percent, there are some deviations[146]. We fit the data to the sum of two Lorentzians (curves in Fig. 4.6) using Eqn. (2.17), with $i = mag$ and sub denoting the

80

broad line in the overlayer and the narrow substrate resonance, respectively in this case. The position of the substrate resonance ν_{sub} was constrained to be independent of temperature, consistent with measurements in semi-insulating GaAs (Section 3.2). Above 250 K and below 30 K, the two lines are unresolved, so a single Lorentzian was used (Eqn. (2.16)).

The results of this analysis are summarized in Fig. 4.7. As is evident in the raw data (Fig. 4.6), the broad line shifts towards lower frequency and broadens as temperature is reduced. The slight temperature dependence of the amplitude of the substrate line A_{sub}, is consistent with previous measurements in semi-insulating GaAs[104]. It may be due to ^{8}Li stopping in noncubic sites produced by implantation–related damage, *e.g.* arsenic vacancies, as has been observed for ^{12}B implantation in ZnSe[114]. The amplitude of the broad resonance A_{mag} decreases as the line broadens, as expected for a constant applied rf field. There is no evidence of a sharp change of either amplitude through T_C, nor is there a sharp change of the total area of the spectrum at T_C. Continuity of the amplitude through T_C is in contrast to the conventional NMR "wipeout effect" that often accompanies such a transition[147].

Using the substrate frequency ν_{sub} as the reference, we measure the average internal field B_{int} sensed by the ^{8}Li in the Mn doped layer, B_{int} by the raw shift of the resonance $\Delta\nu$ using Eqn. (2.12) with $B_{int} = B_{tot} - B_o$ and B_o the applied external field. We discuss the various contributions to B_{tot} in Section 4.4.3.

We now turn to the width of the overlayer resonance. The independent Lorentzian broadening combines linearly (Section 2.4.1), so that we decompose the linewidth into different contributions $\sigma_{mag} = \sigma_{sub} + \sigma_{Mn}$, where σ_{Mn} represents the additional broadening due to Mn doping. As shown in the middle panel of Fig. 4.7, σ_{sub} is approximately constant below 200K, therefore the increase in σ_{mag} at low temperature is due to the Mn doping. As the shift of the broad line represents the average total field in the $Ga_{1-x}Mn_xAs$ layer, the broadening represents a distribution of this field; however, there can be other nonmagnetic sources of broadening. In particular, as ^{8}Li is quadrupolar, the width is sensitive to a distribution of electric
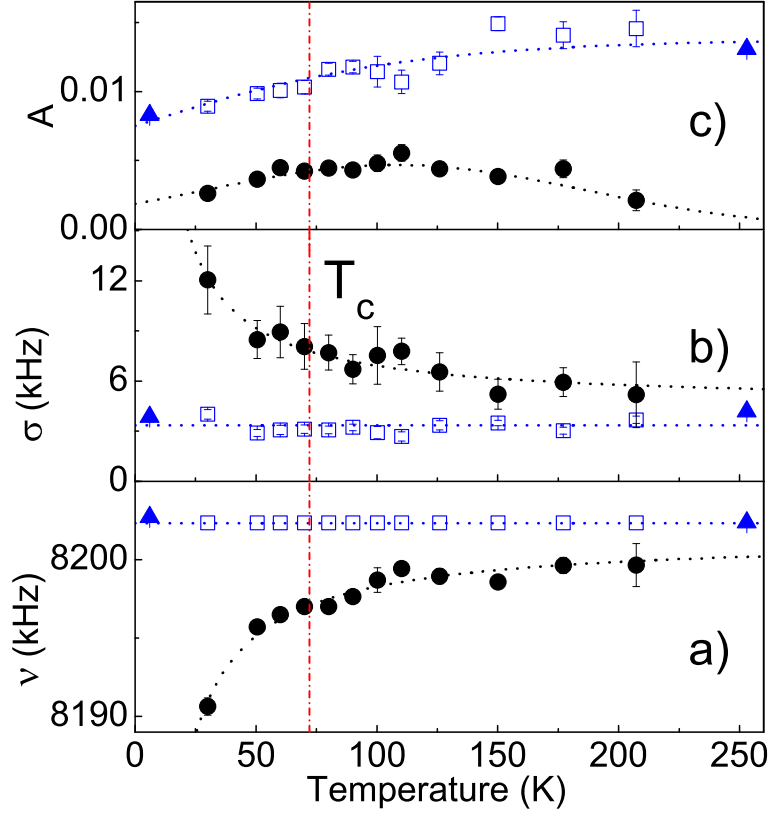
Figure 4.7: The amplitude A (top panel), linewidth σ (middle panel) and position ν (bottom panel) as a function of temperature from Lorentzian fits to the resonance spectra of ^{8}Li implanted at 8 keV in an applied field of 1.33 T. The open squares refer to the narrow substrate resonance, the closed circles to the broad line from the Mn doped layer, and the filled triangles to single Lorentzian fits. The width and position of the substrate line do not change substantially with temperature, in contrast to the resonance from the magnetic layer. The broken vertical line indicates T_C.

field gradients caused by the static charge disorder produced by ionized Mn acceptors. The linear combination of the quadrupolar (σ_q) and magnetic broadening (σ_M): $\sigma_{Mn} = \sigma_q + \sigma_m$ achieves a good fit (see Section 4.4.3). σ_q is expected to be independent of T when $^8Li^+$ is not mobile, as is the case below room temperature.

4.4.2 Spin Lattice Relaxation

In order to better understand the resonance data and to probe the magnetic dynamics in $Ga_{1-x}Mn_xAs$, we performed spin lattice relaxation experiments under the same conditions as the resonances presented above. As expected from the two line spectra, we find a two component relaxation of the $^8Li^+$ nuclear spin polarization. At 8 keV implantation energy, we find a small almost non-relaxing component, consistent with slow relaxation in the GaAs substrate, and a large, much faster relaxing component from the $Ga_{1-x}Mn_xAs$. As in Section 4.3, the relaxation is fit to a simple bi-exponential form (Eqn. (2.23)) for the polarization P at time t after implantation. with A_i is the initial amplitude for each component, and $\lambda_i = 1/T_1^i$ the corresponding relaxation rate, and $i = mag$ and sub denoting the $Ga_{1-x}Mn_xAs$ layer and the GaAs substrate. We fit the experimental data to the convolution of $P(t)$ with the beam pulse to extract the relaxation rate $\lambda_{mag}(T)$ at 1.33 Tesla[148]. Examples of the fits are shown in the top panel of Fig. 4.8. That the 250 K relaxation spectrum lies consistently below the 30 K data is direct evidence that the relaxation is faster at 250 K. The data shown do not appear to have the same total amplitude, likely because there is some very fast relaxation at 250 K which is not captured with the experimental time resolution. Though the fits are reasonably good, this behaviour may indicate that the relaxation is not a simple exponential as in Eq. (2.23). In fact, in an inhomogeneous system, one expects a distribution of relaxation rates corresponding to the distribution of static fields evidenced by the line broadening. Since the polarization of ^8Li in the beam is constant, we fixed the amplitudes in the fits, accounting for the full variation in temperature with only the relaxation rates. Thus λ_{mag} extracted from the fits represents
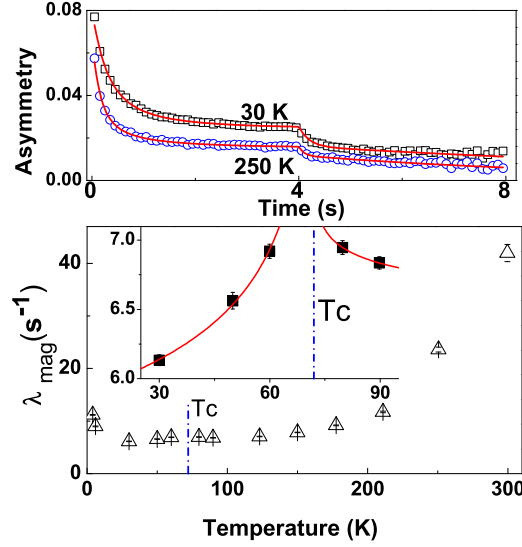
Figure 4.8: Top: Time dependence of the average $^8Li^+$ spin polarization during and after the beam pulse at 30K (below T_C) and at 250 K (above T_C) at 8 keV beam energy in the field of 1.33 T. The relaxation rate is faster at 250 K than at 30 K. Bottom: The spin-lattice relaxation rate λ_{mag} in the overlayer as a function of temperature. The increase in λ_{mag} above 150K is consistent with an increase in semi-insulating GaAs[149] and may be due to the onset of the $^8Li^+$ site change. Inset: An enlarged plot showing a slight enhancement of λ_{mag} in the vicinity of T_C, in contrast to the divergence expected from critical slowing down of spin fluctuations at the transition.

an average relaxation rate for $^8Li^+$ in the $Ga_{1-x}Mn_xAs$ layer. While λ_{sub} varies with T, it remains much smaller than λ_{mag} for all temperatures.

The temperature dependence of λ_{mag} is shown in the bottom panel of Fig. 4.8. Its behavior is very different from that of a conventional ferromagnet $e.g.$ Fe or Ni[150]. For conventional ferromagnetic metals in the paramagnetic state above T_C, the spin lattice relaxation rate λ decreases with increasing temperature since the spins fluctuate faster. Far below T_C, the spins are frozen and the spectral density of the spin fluctuations decreases to zero as temperature decreases to zero. Therefore λ decreases to zero with temperature. In the critical region (near T_C), λ diverges[150], re-

flecting the critical slowing down of spin fluctuations as T_C is approached. Compared with the conventional ferromagnets, λ in $Ga_{1-x}Mn_xAs$ behaves very differently. The most obvious feature is the substantial increase in λ_{mag} above 200 K. Such an increase is unexpected for a simple paramagnet which naively, should exhibit a monotonic decrease of the spin relaxation rate above T_C as spin fluctuations become progressively faster with increasing temperature. The increase, however, may be related to a similar increase[149] found in semi-insulating GaAs that is thought to be due to a $^8Li^+$ site change[104, 108], see also Section 3.2. Enhanced relaxation could result from a stronger hyperfine coupling in the high temperature site, or, if the site change is due to the onset of interstitial $^8Li^+$ diffusion, to the formation of Mn–Li defect complexes[151]. In this case, the $^8Li^+$ may diffuse to the substitutional Mn^{2+} ion (which is effectively negatively charged since it replaces Ga^{3+}) and become trapped. In close proximity to the Mn trap, the $^8Li^+$ would have a strong coupling to the Mn spin and relax quickly. This diffusion–trapping behavior is observed in μSR experiments, *e.g.* in aluminum[110] and iron[152, 153]. The high temperature increase of λ_{mag} accounts in part for the disappearance of the broad resonance at higher temperature. λ_{mag} also increases at the lowest temperature, in contrast to the behavior of a homogeneous ferromagnet. This may be due to some Mn spins remaining paramagnetic well below T_C making a Curie–law contribution to λ_{mag}. Between these limits, λ_{mag} is relatively constant but exhibits a slight peak near T_C inset of Fig. 4.8 bottom panel, where critical slowing down of the Mn moments should yield a *divergence* in the relaxation rate[150]. While the critical region is broadened by the applied field, as well as the microscopic inhomogeneity of the alloy, *e.g.* as in $La_{0.67}Ca_{0.33}MnO_3$[148], the relatively weak temperature dependence through T_C is still surprising. The magnitude of λ_{mag} is large, not only much larger than in undoped GaAs, but also ~ 10 times the rate in metallic Ag, consistent with it originating in the magnetism of $Ga_{1-x}Mn_xAs$.

In general, λ is a measure of the spectral density of (transverse) magnetic fluctuations at the NMR frequency. The absence of a peak suggests that the spin dynamics that dominates the $^8Li^+$ relaxation does not change dramati-

cally through the formation of a static moment, in contrast to homogeneous metallic[150] or semiconducting[154] ferromagnets. Neither does λ follow the linear (Korringa) temperature dependence characteristic of metals[139, 141] that might be anticipated if the relaxation was predominantly due to interaction with a degenerate fluid of delocalized holes in this metallic alloy. However, it is similar to what is found in doped nonmagnetic semiconductors when the Fermi level lies in a narrow impurity band[155, 156, 157].

4.4.3   Analysis and Discussion

We now extend the analysis presented above beginning with the resonance shift. The difference in the average magnetic field between the overlayer and the substrate B_{int} is due to the Mn doping, so we decompose the total field into various contributions from the surrounding Mn doped magnetized layer and the applied field B_o,

$$
\begin{aligned}
B_{tot} &= B_o + B_{int} \\
&= B_o + (B_{demag} + B_{Lor} + B_{dip} + B_{loc})
\end{aligned}
\tag{4.2}
$$

assuming for simplicity that all contributions are parallel at high applied fields. Here B_{demag} is the demagnetization field determined by the macroscopic shape of the sample, and B_{Lor} is the field due to the empty Lorentz cavity that divides the sample into a local region which must be treated atomically from the rest of the sample which may be treated as a homogeneous magnetic continuum. B_{dip} is the net field from the atomic magnetic dipoles inside the Lorentz sphere. B_{loc} is the hyperfine contact field from the atomic environment within the Lorentz cavity.

B_{dip} summarizes the dipolar fields inside the Lorentz cavity:

$$
B_{dip} = \sum_i \frac{3(\mu_i \cdot \mathbf{r}_i)\mathbf{r}_i - \mathbf{r}_i^2 \mu_i}{r_i^5}
\tag{4.3}
$$

where μ_i is the dipole moment at each lattice site $\mathbf{r}_i$ and the sum is over the Lorentz cavity. In high field, all dipoles are aligned parallel to the field (e.g.

along z axis), assuming that they are of the same magnitude μ. Therefore, B_{dip} at the center due to all the dipoles inside the Lorentz sphere is:

$$B_{dip} = \mu \sum_i \frac{3z_i^2 - r_i^2}{r_i^5} = \mu \sum_i \frac{2z_i^2 - x_i^2 - y_i^2}{r_i^5} \tag{4.4}$$

The x, y, z directions are equivalent due to the symmetry of the zincblende cubic lattice and the sphere, thus

$$\sum_i \frac{z_i^2}{r_i^5} = \sum_i \frac{x_i^2}{r_i^5} = \sum_i \frac{y_i^2}{r_i^5} \tag{4.5}$$

Substituting Eqn. (4.5) into Eqn. (4.4), we obtain $B_{dip} = 0$, *i.e.* the net dipole field is zero, so it can not contribute to a shift of the resonance. In this dilute magnetic material, the Mn concentration is 5.4%, corresponding to about one Mn ion in every 5 GaAs unit cells. The dipole field at any particular $^8Li^+$ site (especially those close to the Mn moments) will not be zero, since the surrounding Mn moments are generally not cubic. However, the Mn moments are randomly distributed over the $Ga_{1-x}Mn_xAs$ thin film, so that the $^8Li^+$ site is on average in a site of cubic symmetry with respect to the Mn moments, therefore B_{dip} is averaged out to be zero when summing over the whole film. Note that the dipole field will still contribute to the width of the resonance, see Eqn. (4.11) below.

The sum of B_{demag} and B_{Lor} is defined as the continuum contribution to the internal field:

$$B_{cont} = B_{demag} + B_{Lor} \tag{4.6}$$

B_{int} can be written as:

$$\begin{aligned} B_{int} &= B_{tot} - B_o = \gamma(\nu_{mag} - \nu_{sub}) \\ &= B_{cont} + B_{loc} \end{aligned} \tag{4.7}$$

B_{loc} the local field from the atomic environment within the Lorentz cavity, including the contact hyperfine interaction between mobile holes and the probe nucleus that gives rise, for example, to the Knight shift in metals[115].

It is B_{loc} that is of interest as a measure of the polarization of the delocalized holes.

At the Mn concentration of this sample, there is about one Mn ion per 5 GaAs unit cells (cubic lattice constant ~ 5.7 Å[20]), so there is no difficulty defining a Lorentz cavity much smaller than the film thickness outside of which the $Ga_{1-x}Mn_xAs$ can be treated as a continuum. To an excellent approximation, a thin film of uniform thickness in a perpendicular magnetic field has the maximal demagnetizing field, $B_{demag} = -4\pi M$ (cgs), where M is the continuum magnetization, while for a spherical Lorentz cavity[115], $B_{Lor} = (4\pi/3)M$. We use the $M(T)$ measured in SQUID (Fig. 4.1) to account for these contributions. The continuum field B_{cont} is plotted in Fig. 4.9 together with the measured $B_{int} = B_{tot} - B_o$ for comparison. In using the substrate frequency ν_{sub} as a measure of B_o, we have neglected any chemical shift of the ^{8}Li in GaAs. The assumption is valid because the shift of ^{8}Li in bulk GaAs relative to ^{8}Li in MgO at room temperature is less than 10 ppm (Section 3.3.2.2). We have also assumed that the experimentally determined M is not contaminated by contributions from nonuniformity of the sample, such as impurity phases, *e.g.* occurring at either the surface of the film or at the interface with the substrate. This is reasonable as the measured M is consistent with the literature for films of this composition[158].

From Eq. (4.8),

$$B_{loc} = B_{int} - B_{cont}, \tag{4.8}$$

so that the small observed value of B_{int} (Fig. 4.9) implies B_{loc} must oppose and nearly cancel B_{cont}, i.e. at low temperature B_{loc} is on the order of $+150$ G. We use Eqn. (4.8) to calculate $B_{loc}(T)$ and plot it as a function of $M(T)$ in Fig. 4.10, together with the shift B_{int} and linewidth σ_{Mn}. The clear correlation between B_{loc} and M is embodied in the linear fit $B_{loc} = (7.78 \pm 0.09) \times M[\text{G}] - (3 \pm 1)$ shown in the top panel of Fig. 4.10. This linearity is not surprising, since B_{loc} is predominantly determined by the large contribution of B_{cont} (proportional to M) which is ~ 15 times the size of B_{int}. The ^{8}Li site is cubic on average, so only isotropic contributions to the average B_{loc} will be nonzero[159]. Such fields arise from the contact
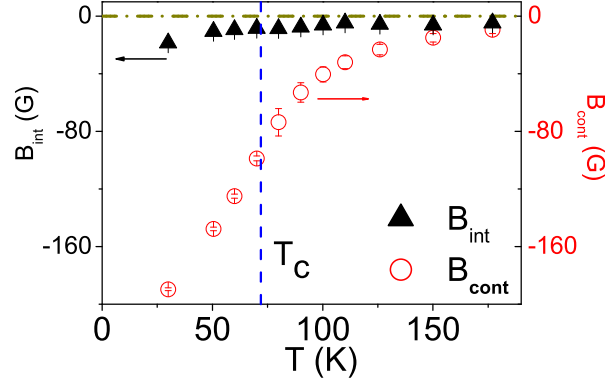
Figure 4.9: A comparison of $B_{int} = B_{tot} - B_o$ (solid black triangles) and the continuum internal field $B_{cont} = -\frac{8}{3}\pi M$ (open red circles). The difference of these indicates that the local field is substantial and nearly cancels B_{cont}.

hyperfine interaction, here due to a mixing of the unoccupied [8]Li $2s$ orbital with partly occupied electronic states of the surroundings, principally the delocalized holes. In this case, B_{loc} should scale with the hole magnetization, M_h, rather than the full magnetization M, i.e.

$$B_{loc} = \left(\frac{A_{HF}}{N_A \mu_B} \right) M_h \tag{4.9}$$

where N_A is the Avogadro's number, μ_B is the Bohr magneton and A_{HF} is the hyperfine coupling constant. In paramagnetic metals this is usually stated as $B_{loc} \propto \chi$, the spin susceptibility of the conduction band. Instead, we express B_{loc} in terms of the field–cooled M to avoid the nonlinearity (hysteresis) in $M(H)$ below T_C. The total macroscopic $M = M_h + M_{Mn}$, where the dominant term is M_{Mn} the magnetization due to the Mn^{2+} local moments, and M_h is predicted to be negative, and much smaller on the order of a few percent of M[160]. While we have no independent measure of M_h, the strong coupling between the holes and Mn moments suggests that $M_h(T)$ should follow the temperature dependence of $M(T)$. Assuming M_h is ~ 1 % of M, as theory suggests[28], the coupling $A = -160 \pm 2$ kG/μ_B is much stronger than in metals such as Ag (20.6 kG/μ_B)[161, 162].

While B_{loc} is evidently positive, M_h is predicted to be negative[160], so A_{HF} is also *negative*. Negative A_{HF} is unexpected from a simple picture where it is due to hybridization of the Li $2s$ orbital with the surrounding GaAs derived valence band. Li is also not likely to exhibit negative A_{HF} from "core polarization"[163]. For ${}^8Li^+$ negative A_{HF} does, however, have precedent in some transition metals where the Fermi level falls in the d band (Pd [139], Pt[140] as well as ferromagnetic Ni[128]). Here a negative s–d coupling arises from the d band wavefunction's behaviour at the interstitial position[164, 165]. In $Ga_{1-x}Mn_xAs$ negative A_{HF} may similarly originate in the Mn derived impurity band picture, where the holes have Mn d orbital character. However, detailed calculations for interstitial Li^+ in both pure and doped GaAs would be necessary to put such a conclusion on a firm footing.

A more stringent test of whether $M_h(T)$ is simply proportional to $M(T)$ comes from considering the raw field shift B_{int} which represents the balance between two nearly cancelling terms, the continuum field that certainly scales with the average $M(T)$ and B_{loc} which may have a different T dependence. In the middle panel of Fig. 4.10, B_{int} is plotted vs. M, demonstrating a linear relationship $(-0.31 \pm 0.03) \times M - (5.2 \pm 0.3)$ that persists through T_C but breaks down at the lowest temperature (30 K), indicating that, well into the ferromagnetic state, the role of the delocalized holes is changing, possibly as temperature falls into the range of the impurity bandwidth. Alternatively, this deviation could be related to the onset of superparamagnetic effects seen in field–effect heterostructures[51]. which may also lead to the observed increase in the spin relaxation at low T (Fig. 4.8).

We now consider the temperature dependence of the linewidth. Assuming the broadening of the resonance in the $Ga_{1-x}Mn_xAs$ layer is a linear combination of a temperature independent quadrupolar broadening (σ_q) from charge disorder and a magnetic broadening that scales with magnetization ($\sigma_m = \alpha M$):

$$\sigma_{Mn} = \sigma_q + (\alpha M) \tag{4.10}$$
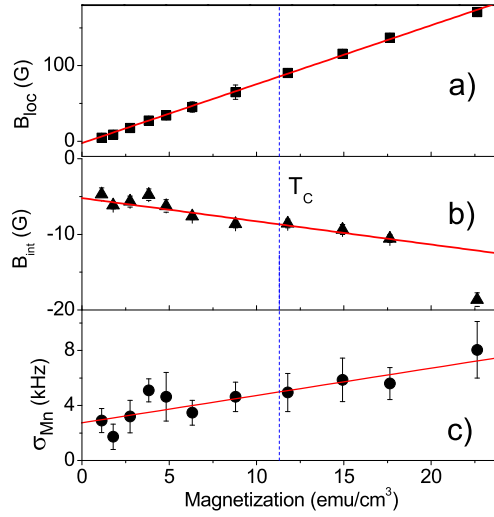
Figure 4.10: Top: The local field B_{loc} after demagnetization correction as a function of the volume magnetization M. The vertical intercept appears slightly different from zero. This is likely due to a slight uncertainty in the background correction for the SQUID measurement of M. Middle: The raw field shift B_{int} as a function of volume magnetization M. The nonlinearity at low temperature indicates B_{loc} is not simply proportional to the measured bulk magnetization. Bottom: The excess linewidth σ_{Mn} as a linear function of M fit to Eq. (4.10). The temperature independent quadrupolar broadening σ_q is found to be 2.7$\pm$0.5 kHz.

We fit σ_{Mn} to Eq. (4.10) as shown in the bottom panel of Fig. 4.10, and find the quadrupolar broadening σ_q is 2.7 ± 0.5 kHz and $\alpha = 0.20 \pm 0.06$ kHz/(emu/cm^3). Due to the randomly located Mn^{2+} local moments, we expect a distribution in the local magnetic field at the ^{8}Li site that will thus give rise to an inhomogeneous broadening of the line that scales with M_{Mn} (or practically with M). Such a broadening is well established in the NMR of dilute magnetic alloys[166]. The observed width indicates the local magnetic field distribution is relatively broad in the sense that its width is comparable to its average (the shift), *e.g.* at the highest M (lowest T), σ_m at the highest magnetization is ~ 8.05 kHz (corresponding to ~ 13 G), comparable to the shift B_{int} in the middle panel of Fig. 4.10. Using the dilute limit result of Ref. [146], we can quantitatively estimate the broadening due to the Mn$_{Ga}$ dipolar fields σ_{dip}, neglecting interstitial Mn and any inhomogeneous polarization of the mobile holes (RKKY oscillations):

$$\sigma_{dip} = \frac{8\pi}{9\sqrt{3}}\rho c \gamma \langle m \rangle \tag{4.11}$$

where ρ is the density of sites available to the impurity (Mn in this case), c is the occupation probability of any given site, γ is the gyromagnetic ratio of ^{8}Li$^+$ and $\langle m \rangle$ is the average impurity moment. In the case of $Ga_{1-x}Mn_xAs$, $\rho c \langle m \rangle = M$. Therefore Eqn. (4.11) becomes:

$$\sigma_{dip} = \frac{8\pi}{9\sqrt{3}}\gamma M \tag{4.12}$$

Assuming $M \approx M_{Mn}$, we estimate the linewidth to be ~ 22.3 kHz at 30 K. Alternatively, this yields an estimate for the parameter $\alpha = 1.02$ for coupling to M of the substitutional Mn, substantially larger than the fit value in the bottom panel of Fig. 4.10. This discrepancy is likely a consequence of the relatively high concentration ($\sim 5\%$), where the dilute limit expression overestimates the broadening, and the magnetic compensating effect of the interstitial Mn[28]. Note that neutron reflectometry has shown there may be a gradient in the interstitial Mn concentration through the film[167], which may thus cause a depth dependence of the ^{8}Li$^+$ resonance.

4.4.4 Summary

We have studied the magnetic properties of an epitaxially grown $Ga_{1-x}Mn_xAs$ thin film, a dilute ferromagnetic semiconductor, with low energy implanted $^8Li^+$, a β-NMR local magnetic probe.

We clearly resolve resonances from both the nonmagnetic GaAs substrate and surprisingly from the magnetic film. The temperature dependence of the resonance position in the film indicates that the hole contribution to the magnetization scales with the macroscopic magnetization through T_C but then deviates below ~ 40 K. The hyperfine coupling constant of $^8Li^+$ in $Ga_{1-x}Mn_xAs$ is unexpectedly found to be negative, which may indicate the Fermi level falls into a Mn derived impurity band. The spin relaxation rate shows a small enhancement at T_C and does not follow the Korringa's Law that might be expected for this metallic alloy. This may also indicate that delocalized holes are from a Mn derived impurity band in $Ga_{1-x}Mn_xAs$.

4.5 The Effect of Magnetic Field on the β-NMR Spectrum of $^8Li^+$ in $Ga_{1-x}Mn_xAs$

In the last section, we observed the $^8Li^+$ resonance spectrum in $Ga_{1-x}Mn_xAs$ consisting of two distinct resonances at 50 K in the field of 1.3 T. The narrow resonance is from the GaAs substrate, while the broad resonance is associated with the magnetic $Ga_{1-x}Mn_xAs$ layer and shifts to a lower frequency. In this section, we present resonance data in pulsed rf mode to study the effect of the external field on the β-NMR spectrum of $^8Li^+$ in $Ga_{1-x}Mn_xAs$ thin film.

The resonance data were taken in 3 different fields at 50 K with the beam energy of 8 keV under the same conditions (Fig. 4.11). Two resonance components are clearly resolved. The broad resonance shifts negatively out of the narrow resonance and broadens as the magnetic field increases. We fit the data to the sum of two Lorentzians (Eqn. (2.17)). Because $^8Li^+$ resonate at different frequency (Eqn. (2.9)), we convert the frequency into frequency shift with respect to the position of the narrow resonance $\nu - \nu_{sub}$, so that

Figure 4.11: Field dependence of $^8Li^+$ resonance spectra in $Ga_{1-x}Mn_xAs$ with implantation energy 8 keV at 50 K below T_C (T_C= 72 K). Spectra are offset for clarity.

Figure 4.12: The analysis results of β-NMR spectra of $^8Li^+$ with 8 keV at 50 K for various fields. Bottom panel: The raw frequency shift linearly scales with the external field. Top panel: The linewidth in the magnetic $Ga_{1-x}Mn_xAs$ overlayer σ_{mag} and in the GaAs substrate σ_{sub} as a function of the external field B.

we can plot the resonance spectra of three magnetic fields in Fig. 4.11. As shown in Fig. 4.12, the broad resonance in the spectrum measured at 0.5 T is almost merged into the narrow resonance. Its presence is only evident by the small asymmetry of the narrow resonance at lower frequency. For the spectrum at 2.2 T, the resonance in the $Ga_{1-x}Mn_xAs$ layer is broadened by the magnetic field and approaches our detection limit, so that the baseline of the spectrum is not defined very clearly. These effects result in large errorbars in the fit results shown in Fig. 4.12.

The fit results are summarized in Fig. 4.12 and we follow the analysis in Section 4.4. The resonance frequency shift $\Delta\nu$ is calculated using Eqn. (2.12) with the substrate frequency ν_{sub} as the reference. The magnetic

origin of the resonance shift is confirmed by the linearity of the frequency shift on the external field B_o: $(-0.09\pm1)+(-5.0\pm0.9)\times B_o$. The y-intercept $((-0.09\pm1)$ kHz/T) is close to zero, indicating that there is no additional orbital coupling in the $Ga_{1-x}Mn_xAs$ overlayer.

Recall that the internal magnetic field $B_{int} = B_{tot} - B_o$ linearly depends on the bulk magnetization M: $B_{int} = (-0.31\pm0.03)\times M-(5.2\pm0.3)$ (Section 4.4.3). Using χ the volume susceptibility $\chi = \partial M/\partial B_o$, we assume that the bulk magnetization of the $Ga_{1-x}Mn_xAs$ overlayer is a linear function of the external magnetic field $M = \chi B_o + M_o$ and M_o is a constant. It is natural that in a ferromagnet, the bulk magnetization does not vanish when the external field is zero once the material is *magnetized*. We could extract from both linear relations that $\chi = 26\pm5$ and $M_o = -16\pm7$ T. Using the resulting volume susceptibility χ, the bulk magnetization M at 50 K and 1.33 T can be estimated as 18 ± 9 emu/cm^3, consistent within error bars with the experimental value measured by SQUID (Section 4.2).

The linewidth of the GaAs substrate σ_{sub} shown in the top panel of Fig. 4.12 is approximately a constant within errorbars, independent of the magnetic field. The nonmagnetic broadening in the GaAs substrate could be quadrupolar broadening, which is due to the small quadrupole moment of $^8Li^+$. The quadrupole splitting resulting from EFG may not be resolved in the spectrum, but goes into the resonance broadening (Section 2.4.1.1). As already discussed in Section 4.4, the linewidths of Lorentzian lineshape add up linearly. Similar to Eqn. (4.10), the linewidth of the broad resonance σ_{mag} shown in Fig. 4.12 is fit to a linear relation of the external magnetic field B_o $\sigma_{mag} = \sigma_q+(\alpha'B_o)$. The fit line is $(1\pm4)+(5\pm3)\times B_o$. Considering the linear relation between the magnetization and the magnetic field $M = \chi B_o+M_o$ assumed above and using the susceptibility $\chi = 26\pm5$ we extracted from the analysis of the shift, we calculate α defined in Eqn. (4.10) $\alpha = \alpha'/\chi = 0.2\pm0.1$ kHz/(emu/cm^3). This value is consistent within errorbars with the value ($\alpha = 0.2\pm0.06$ kHz/(emu/cm^3) we got from the temperature dependence data (Section 4.4.3).

4.6   Magnetic Phase Separation Problem

We now return to the question of phase separation. Based on low energy μSR (LEμSR) experiments, it was proposed that the ferromagnetic state is nanoscopically separated into comparable volumes of ferromagnetic and paramagnetic phases[50]. In contrast, Dunsiger *et al.* also using LEμSR, found no evidence for phase separation in their samples[52]. To address this controversy directly, it is essential to use a local probe, such as ^{8}Li$^+$ to look for evidence of phase separation.

In the pulsed rf data presented in Section 4.4.1, the single broad resonance in the overlayer shows no indication of this inhomogeneity below T_C. But unlike LEμSR, we lack an absolute calibration of the resonance amplitude which depends on a combination of factors, including the spin lattice relaxation rate $(1/T_1)$, the resonance linewidth, and details of the radio frequency (rf) magnetic field used to observe it. Therefore, from the data of Fig. 4.6, we cannot put a quantitative limit on the existence of other phases.

However, with high enough rf power, the resonance collected in the continuous wave (CW) mode may be saturated, providing a means to calibrate the full amplitude. In this section, we analyze the amplitudes from both pulsed and continuous wave (CW) rf measurements, and we conclude that there is no evidence in our data to support phase separation.

4.6.1   Further Analysis on the Amplitude of the Pulsed RF Resonance

We already discussed in Section 2.4.1.2 that, in the pulsed mode, the resonance data is the step in the polarization caused by the rf pulse at that frequency, so there is no direct information in the baseline on the steady state polarization $(\bar{P})$ that still determines the overall resonance amplitude. Using the amplitudes from the Lorentzian fits in Section 4.4.1, we do further analysis on the amplitude. We separately integrate the narrow and broad components to yield the integrated amplitudes A$_{int}$ shown in Fig. 4.13 top panel. Note the substrate and overlayer amplitudes are essentially equal below 150 K before the relaxation rate $\lambda^T = 1/T_1$ is taken into con-
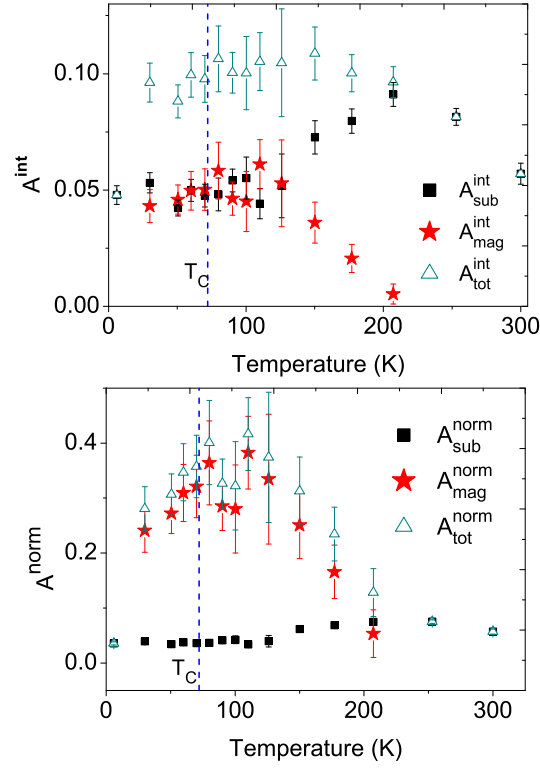
Figure 4.13: Top: Integrated amplitudes A^{int} from the pulsed rf data as a function of temperature. The total integrated amplitude A_{tot}^{int} is constant below 150 K except at 6 K where the resonance in the magnetic layer is too wide to be detected. All integrated amplitudes change smoothly through T_C.

Bottom: Temperature dependence of normalized amplitude A^{norm} weighed by relaxation λ_i rate in each layer. ^{8}Li in the $Ga_{1-x}Mn_x As$ layer relaxes much faster than than in the substrate (Session 4.4.2). Therefore A_{mag}^{norm} is scaled much larger than A_{sub}^{norm} and is dominant in the total normalized amplitude A_{tot}^{norm} as expected from the 8 keV implantation energy.

sideration (Fig. 4.13 top panel). However, fast relaxation in the magnetic overlayer leads to a significant reduction of the apparent amplitude of the pulsed mode rf resonance. As described in Section 4.3.1, we multiply the integrated amplitudes A_i^{int} by the factor $(1 + \lambda_i^T \tau)/(1 + \lambda_{sub}^{300K} \tau)$[141] to account for the contrast in relaxation rate λ^T. Relaxation rates (for each component) are obtained in the spin-lattice relaxation experiments discussed in Section 4.4.2. The resulting A_i^{norm} is plotted in Fig. 4.13 bottom panel. This essentially normalizes the amplitudes to the substrate signal at 300 K. From this, we see that the substrate fraction is only about ∼10% at 100 K. Above 200 K (and at the lowest temperature, 6 K), the overlayer signal cannot be resolved, and the single Lorentzian fits are treated as originating in the substrate, so these points represent only a lower limit for the total amplitude there.

The amplitude A_i^{norm} should be a measure of the relative fractions of ^{8}Li$^+$ stopping in each layer. Most importantly for phase separation, the integrated amplitudes evolve smoothly through T_C. In the proposed phase separation scenario[50], one might consider whether the narrow substrate resonance contains a signal from ^{8}Li in regions of the overlayer that remain paramagnetic. As we already discussed in Secion 4.3, this is not supported by the implantation depth dependence that shows the narrow signal disappears completely at lower implantation energies (Fig. 4.3). Moreover, ^{8}Li in nanoscopic paramagnetic regions within the Mn doped would also experience the same large continuum demagnetizing field and thus would shift with temperature, in contrast to the narrow resonance in Fig. 4.6. On the other hand, if either of the two phase separated regions was unobserved in our spectra, *e.g.* if the spin relaxation was very fast or the static internal field was so large that the resonance occurred outside our frequency range, we would expect to lose some resonance *amplitude* at the transition. However, the continuous change of both amplitudes (the top panel of Fig. 4.7) and the integrated area of the resonance through T_C does not support this. The continuity of A_i^{norm} through T_C thus also shows no evidence of phase separation. This result is, however, consistent with the full volume fraction magnetism found in LEμSR in samples with a range of Mn concentrations

encompassing that of the current sample[52].

4.6.2 CW Mode Resonance

Using resonance data collected in the continuous wave (CW) mode, we have sufficient rf power to fully saturate the resonance at room temperature[136], while at lower temperature, the line is too broad to saturate. The integral of the room temperature spectrum can be used as a calibration of the full amplitude corresponding to all the ^{8}Li.

Fig. 4.14 top panel shows the resonance spectra of ^{8}Li$^+$ in CW mode at full beam energy (28 keV) and at two temperatures, 30 K and 300 K. Please note that these resonance data were only collected as part of the tuning up procedure, so one of the data sets shown in Fig. 4.14 does not completely cover the resonance frequency range. Nevertheless, it is included as it clearly demonstrates complete saturation of the resonance at zero bias and 300 K. The two sets of resonances (up and down) correspond to two ^{8}Li polarizations, parallel and antiparallel to the beam. The first factor influencing the resonance amplitude, the temperature dependent off-resonance baseline, is apparent in the figure. The baseline (steady state polarization) is determined by the spin lattice relaxation ($\lambda = 1/T_1$) and the lifetime of ^{8}Li$^+$ τ (Section 2.4.1), so any temperature dependence of $1/T_1$ will affect it[141]. Simply normalizing to the baseline, i.e. the difference between the two polarizations, at each temperature accounts for this systematic effect.

As shown in Fig. 4.14, at 28 keV, the ^{8}Li$^+$ penetrate the Ga$_{1-x}$Mn$_x$As layer and stop in the GaAs substrate (see Fig. 4.2 and discussion in Section 4.3), resulting in a single resonance, whose width is close to that in GaAs (Section 3.2). At 300 K, the resonances from the two polarizations meet, indicating the resonance is saturated, i.e. the rf power is high enough to destroy all the ^{8}Li polarization. At 30 K the same CW rf is **not** sufficient to achieve saturation even though the resonance is somewhat *narrower*. This behaviour was also observed in semi-insulating GaAs[104]. It may be due to a fraction of ^{8}Li$^+$ that stops in disordered sites, *e.g.* near implantation related vacancies. The resonance from such sites is broadened by quadrupo-
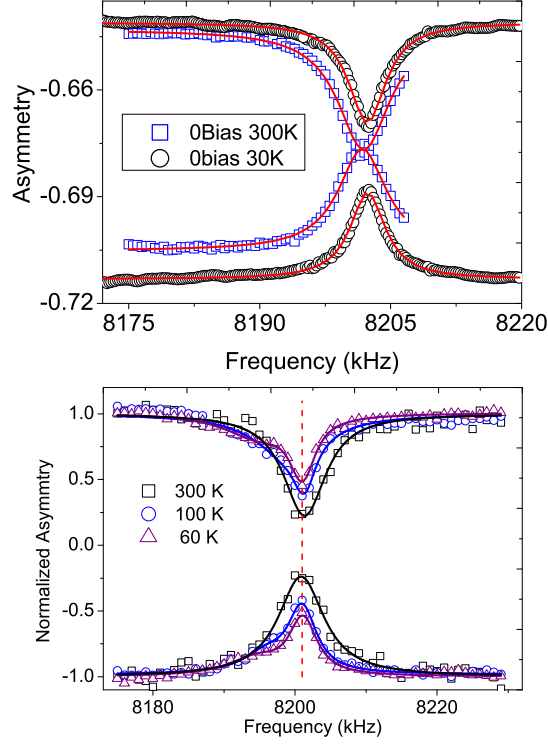
Figure 4.14: Top: The CW β-NMR spectra in the $Ga_{1-x}Mn_xAs$(28 keV implantation) at 300 K (black squares) and 30 K (blue circles). Only a single resonance is resolved. At 300 K, the resonances from the two helicities meet, indicating that the signal is fully saturated.
Bottom: Normalized CW β-NMR resonance spectra at 8 keV implantation energy at different temperatures. $^8Li^+$ in the substrate produces the narrow resonance, while the broad resonance (shoulder on the low frequency side) originates in the $Ga_{1-x}Mn_xAs$ thin film.

lar effects and may be too broad to observe, as has been found in β-NMR of ^{12}B implanted in ZnSe[114].

At a lower implantation energy (8 keV), the analogous behaviour of the CW amplitude in the Mn doped layer is shown in the bottom panel of Fig. 4.14. As discussed in previous sections, the two resonances in the spectra below room temperature are due to ^{8}Li^{+} stopping in the Mn doped layer (broad, negatively shifted) and in the nonmagnetic GaAs substrate (narrow).Because of power broadening, they are not well-resolved here, with the broad line appearing as a low frequency shoulder. At 300 K, the spectrum is *not* saturated, even though the width is comparable to that in the substrate. Similarly the lack of saturation here may be due to ^{8}Li^{+} stopping in disordered sites. In this case such sites may include those neighboring the magnetic Mn^{2+} dopants which cause both quadrupolar and magnetic effects in the ^{8}Li resonance. Again we fit the data to the sum of two Lorentzians (curves in Fig. 4.14) using Eqn. (2.17). At room temperature, a single Lorentzian was used.

To account for the effect of $1/T_1$, we first normalize each spectrum by dividing it by its baseline A_o. Temperature dependent line broadening also affects the amplitude, so we integrate the normalized spectrum over the frequency range of the data to obtain A^{int}_{norm}, the integrated amplitude, that provides a measure of the corresponding ^{8}Li^{+} fraction. The A^{int}_{norm} is then expressed as a fraction of its value at room temperature (and 8 keV), where we have full saturation at least for the fraction of the signal in the substrate. Using this procedure, A^{int}_{norm} at 100 K corresponds to 73% of the room temperature (8 keV) value, and at 60 K to about 62%. Thus, through the transition, the loss of signal corresponds to only about 11 % of the ^{8}Li^{+} at room temperature, much smaller than found by LEμSR[50]. Recall that the amplitude in semi-insulating GaAs also depends on temperature, see the top panel of Fig. 4.7. This intrinsic change in the amplitude of the ^{8}Li resonance may account for much or all of the amplitude change here.

4.6.3 Summary

Although β-NMR does not provide a direct measure of the magnetic volume fraction, we can use the CW rf spectra to make a reasonable estimate. We can also use the pulsed rf spectra weighted by the spin lattice relaxation rate to show these fractions do not change abruptly at T_C. The results both show no evidence for magnetic phase separation in this sample. The lack of evidence for phase separation may be a consequence of differences in the samples used in Ref. [50] which differed both in Mn concentration and in T_C. In contrast, our results are consistent with the full volume fraction magnetism found by a "wipeout effect" of the weak transverse field LEμSR in samples with a range of Mn concentrations encompassing that of the current sample[52].

Chapter 5

Ferromagnetic Proximity Effect in Fe/GaAs Heterostructures

The results of β-NMR measurements in GaAs were presented in Ch. 3. The high resolution pulsed rf spectra show a small intrinsic temperature-dependent shift of the $^8\mathrm{Li}^+$ resonance below 150 K in both semi-insulating and heavily doped n-type GaAs. The depth-dependent resonance shift, only observed in the semi-insulating GaAs, may be due to the band-bending at the free surface. The linewidth is narrow, not depth-dependent and weakly depends on temperature. Having carefully characterized the temperature-depth- and doping- dependence of the $^8\mathrm{Li}^+$ β-NMR signal in the GaAs crystals, we are ready to study the local magnetic properties of the Fe/GaAs heterostructures.

In this chapter, we will first review the preparation and properties of the Fe/GaAs heterostructures in Section 5.1, and present the data on Fe/semi-insulating (SI) GaAs (09-A1) (Section 5.2.1) and Fe/n-GaAs (10-A1) (Section 5.2.2) with no injected current. Section 5.3 will discuss the current injection from the magnetic Fe layer into the heavily doped n-type GaAs (11-A1) detected by β-NMR.

5.1 The MBE Growth and Properties of Fe/GaAs Heterostructures

5.1.1 The MBE Growth of Fe/GaAs Heterostructures

First let's review the MBE growth of Fe/GaAs heterostructures and their properties. As we already discussed in Section 1.3, in addition to ferromagnetic semiconductors, another way of introducing polarized spins in semiconductors is to "transfer" the ferromagnetism from a ferromagnet (FM) into a conventional semiconductor (SC). A direct solution is to fabricate an ultrathin ferromagnetic layer on a carefully-prepared semiconductor surface. Fe/GaAs is an obvious choice for such a hybrid FM/SC system. Fe (reviewed in Section 1.2.2) is a strong ferromagnet with a high Curie temperature (T_C) and high spin polarization. GaAs, on the other hand, is the most widely used III-V semiconductor. The low lattice mismatch between Fe and GaAs provides the basis for good epitaxial growth[168].

Molecular Beam Epitaxy (MBE) is an evaporation technique to grow single crystal at a very low rate (*e.g.* 2–10 atomic layers per minute in the growth of $3d$ transition metals) under ultrahigh vacuum (UHV) conditions (with pressures $\sim 10^{-10}$ Torr). The UHV guarantees that the evaporated atoms or molecules form a beam directed towards the crystalline substrate and are not scattered by the residual gas molecules. The very low rate of impinging atoms or molecules ensures the controllable growth of a highly ordered crystalline layer of a new material with high purity. The individual layer thickness can range from a few atomic layers to hundreds of nanometers which makes MBE particularly suitable for growing ultrathin film structures. All the samples studied in this chapter were grown using MBE by B. Kardasz in the group of B. Heinrich at Simon Fraser University (SFU) in the same way, and they have the same interface features.

We used both semi-insulating (SI) GaAs and heavily Si doped n-GaAs crystals as substrates. The SI-GaAs substrate is cut from the same wafer as Sample 09-B1 (Wafer Technology Ltd.). The characterization of the semi-insulating GaAs substrate was presented in Section 3.3. The n-GaAs sub-
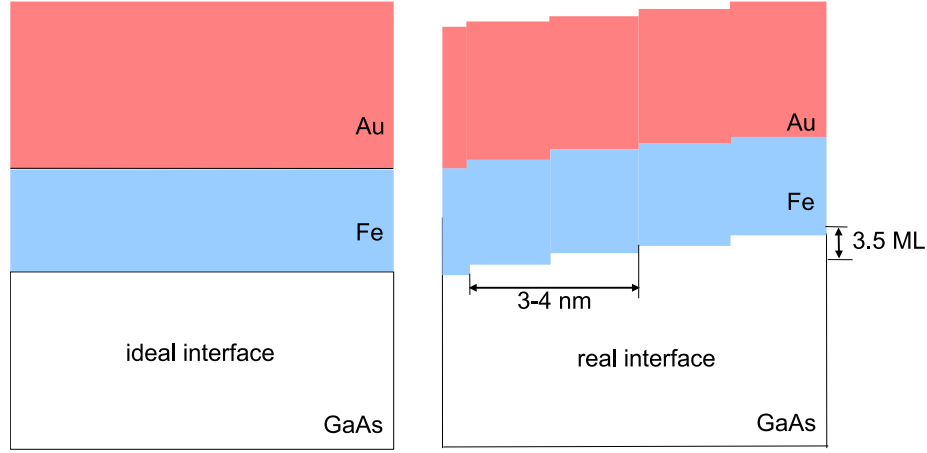
Figure 5.1: Left: diagrams of ideal interface–perfectly flat. Right: real interface.

strate is similar to the one (09-B2) we reported in Section 3.3, but from Wafer Technology Ltd. with one side etched and polished. Its carrier concentration is $(1.1-1.8) \times 10^{18}$ cm^{-3}. Each substrate was cleaned by hydrogen cleaning, sputtered with Ar$^+$ and annealed at $\sim 600°$C before MBE growth to remove any surface native oxide. A 14 monolayer (ML) Fe thin film was epitaxially grown by MBE on the GaAs substrates (semi-insulating or heavily doped n-type GaAs). A 20 ML Au layer was deposited on top of Fe layer to protect it from oxidation. The Fe and Au films were deposited at a relatively low temperature for MBE under UHV ($\sim 10^{-10}$ Torr). During the deposition, the temperature of GaAs substrate was measured to be ~ 65 °C. The growth process was monitored by Reflection High-Energy Electron Diffraction (RHEED) intensity oscillations[169]. The MBE growth at SFU is highly standardized. Their growth studies show that after deposition of the equivalent of three atomic layers, a continuous Fe film was formed, having atomic terraces approximately 3–4 nm wide on average[169]. The interface is not perfectly flat as shown in Fig. 5.1. At the Fe/GaAs interface, the average roughness is 2 ML, and maximum deviation in height is 3.5 ML as measured by STM from characterization done on similar samples grown under the same conditions.

Mössbauer studies were carried out by B. Kardasz [170] on a series of Fe/GaAs samples prepared in the same way but with different Fe layer thicknesses. They indicate the interface is close to ideal, but some Fe atoms may penetrate into the GaAs substrate during deposition, which is in agreement with STM images[171]. These Fe atoms substitute for Ga atoms in the second layer and displace them into an interstitial position. It was suggested that the Fe atoms inside the top As layer together with the top Fe layer could form Fe_2As compound. They did not comment on the thickness of the intermixing layer, but considering that a continuous film of Fe is formed after equivalent 3 atomic layers, the intermixing layer may be no thicker than 3 atomic layers, ~ 0.7 nm.

5.1.2 Stopping Distribution of $^8Li^+$ in Fe/GaAs Heterostructures

The $^8Li^+$ implantation profile (bottom panel of Figure 5.2) is simulated by SRIM-2006.02 [93]. The energy dependence of the implantation depth and width are shown in the inset of Figure 5.2 top panel. The $^8Li^+$ beam was injected into the sample in the external field of 2.2 T. Implantation energy was varied from 28 keV to 2 keV, making the average $^8Li^+$ depth vary from ~ 140 nm down to ~ 20 nm from the sample surface. The implantation depth in Fe/GaAs heterostructures is not substantially different from that in bare GaAs (Fig. 3.3), since the total thickness of the Au and Fe layers is only several nanometers.

As shown in the top panel of Fig. 5.2, the higher carrier density in the heavily doped n-type GaAs greatly narrows the Schottky barrier at the Fe and GaAs interface compared with that in the semi-insulating GaAs (see discussions in Section 1.3.1).

5.1.3 Current-Voltage (IV) Characteristics of Fe/n-GaAs Samples

Here I present the I-V characteristics of the Fe/n-GaAs (11-A1), which is directly related to the current injection measurements presented in Section
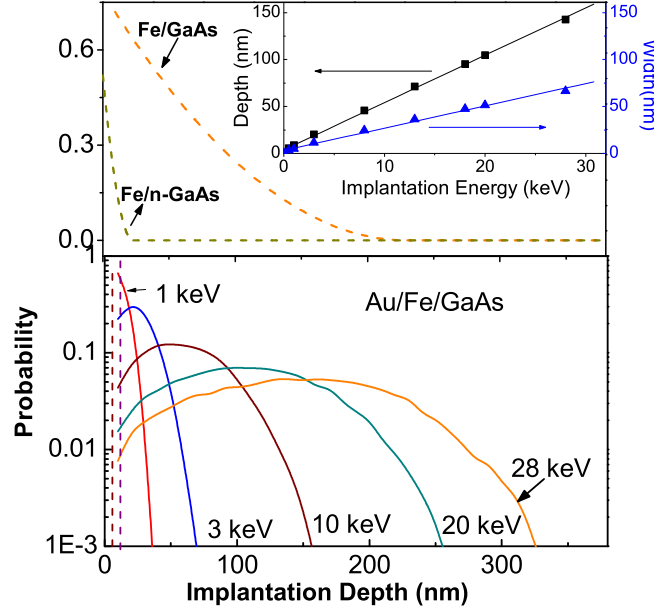
Figure 5.2: Top panel: The orange dashed line and the pale yellow dash-dot line are the Schottky barrier profiles in semi-insulating GaAs substrate and heavily doped n-type GaAs respectively[172]. The barrier width shrinks as the carrier density increases in the semiconductor. The inset is the energy dependent implantation depth and implantation distribution's width.
Bottom panel: Solid lines are the implantation profiles in Au/Fe/GaAs simulated by SRIM-2006.02 with different implantation energy (shown on a log scale). The red solid squares are the SRIM simulation in n-type GaAs with implantation energy at 28 keV, which is similar to that in the Au/Fe/GaAs sample at the same energy.
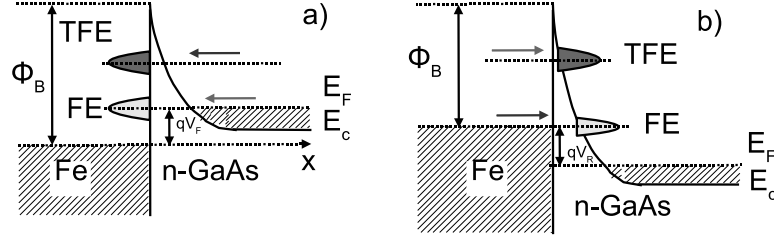
Figure 5.3: Field emission (FE) and thermoionic emission (TFE) tunneling through a Schottky barrier for forward (left) and reverse (right) bias on Fe/n-GaAs. Adapted from Ref. [172].

5.3.

As we discussed in Chapter 3, the Fermi level of the n-GaAs is above the bottom of the conduction band because of the high hoping level. In such heavily doped GaAs, the depletion region is very thin, therefore the current due to the tunneling of carriers through the barrier becomes the dominant transport process[172, 173].

Tunneling can occur in a Schottky barrier junction in two ways: field emission (FE) and thermionic field emission (TFE), which are shown in Fig. 5.3 for forward (left panel) and reverse (right panel) bias. Under forward bias, the I-V characteristic in the presence of tunneling in Fe/n-GaAs is[172]:

$$I = I_s \exp\left(\frac{eV}{E_o}\right) \tag{5.1}$$

where e is the electron charge, the saturation current I_s depends only weakly on voltage, and E_o is a tunneling constant and is given by:

$$E_o = E_{oo}\coth\left(\frac{E_{oo}}{k_{\mathrm{B}}T}\right) \tag{5.2}$$

with k_{B} the Boltzmann constant, and E_{oo} is an important parameter in tunneling, inherently related to material properties of the semiconductor, and can be expressed as:

$$E_{oo} = \frac{eh}{4\pi}\left(\frac{N_d}{m^*\epsilon\epsilon_o}\right)^{1/2} \tag{5.3}$$

where h is the Planck's constant, N_d is the doping concentration, close to the carrier concentration in our case, $m^* = 0.067m_e$ is the conduction band effective mass of GaAs (m_e is the electron mass), e is the electron charge and $\epsilon = 13.18$ is the relative dielectric permeability for GaAs (Section 1.3.1).

When E_{oo} is large or at low temperatures, $E_{oo} \gg k_{\mathrm{B}}T$. Under forward bias, electrons with energy close to E_{F} can tunnel from the semiconductor into the metal, in a process known as Field Emission (FE). $E_o \approx E_{oo}$, therefore the slope of the $\ln(I)vs.V$ plot is constant, independent of temperature T.

On the other hand, when E_{oo} is small or at higher temperatures, $E_{oo} \ll k_{\mathrm{B}}T$. A significant number of electrons can be thermally excited above Fermi level where the Schottky barrier is lower and thinner. These electrons thus can tunnel into the metal before reaching the top of the barrier. This tunneling of thermally excited electrons is known as Thermionic Field Emission (TFE). The slope of the $\ln(I)vs.V$ plot is $e/k_{\mathrm{B}}T$, inversely proportional to temperature T.

When a reverse bias is applied, the current is very small at low bias voltage. As the bias voltage increases, the current also has an exponential dependence on the applied bias. If field emission and/or thermionic field emission are the dominant conduction mechanisms under forward bias, they will also be the dominant mechanism for the reverse characteristics.

The I-V characteristic curve of the Fe/n-GaAs is shown in Fig. 5.4. The I-V curve was measured on a test sample made exactly in the same way as Sample 11-A1. The 77 K measurement was taken in 4-wire configuration. The other 2 data sets were obtained by 2-wire measurement in situ in the β-NMR experiment on Sample 11-A1, so they may have some contribution from the lead resistance's temperature dependence. Under positive voltage, the sample is forward biased with electrons flowing from the n-GaAs substrate to the Fe layer. The current grows exponentially with the bias voltage. In the right panel of Fig. 5.4, the slope of the $\ln(I)vs.V$ plot does not drastically vary with temperature, therefore the current transport through the Schottky barrier is mostly due to Field-Emission (FE). Under negative voltage, the structure was reverse biased. The current was initially small
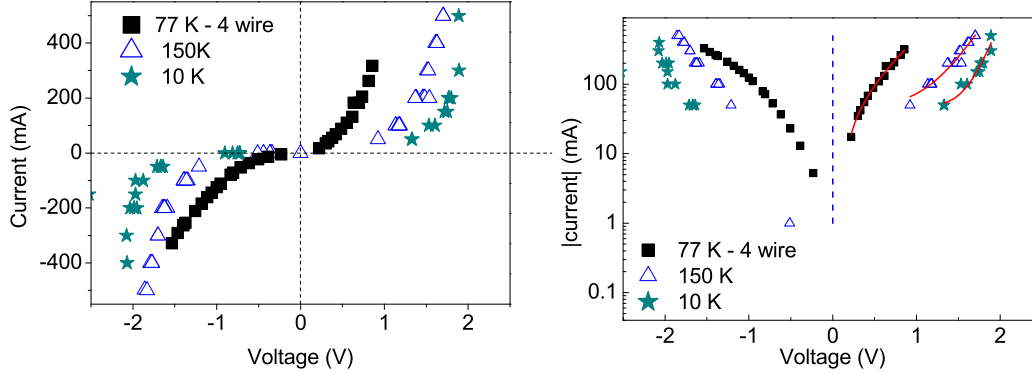
Figure 5.4: I-V characteristic curve of Fe/n-GaAs plotted in original (Left) and log (Right) scale. The I-V curve was measured using 4-wire measurement on a testing sample of Fe/n-GaAs which is made exactly the same as Fe/n-GaAs (11-A1). The Fe/n-GaAs structure is forward biased under positive voltage, and reversely biased under negative voltage. The right panel is plot in log scale. In the right panel, the absolute vale of current is plotted in log scale.

for small reverse biases, and increases exponentially when the reverse bias exceeds ~ 0.7 V. Under moderate reverse bias voltage, FE may occur in the heavily doped GaAs, resulting in the exponentially increasing current observed in Fig. 5.4. The Au/FeGaAs structure behaves as a Schottky barrier with highly non-linearly I-V characteristics.

5.1.4 Spin Current through Fe/GaAs Heterostructure Interface

At zero bias, the Schottky barrier at the interface between the Fe metal and the semiconductor results in a charged depletion region which has a large spatially varying electric field. This has important consequences on charge current flow at metal/semiconductor interfaces. Thus, it is expected that this energy barrier and depletion region also have important consequences on spin transport at these interfaces.

Theoretical calculations show that the Schottky barrier with a significant depletion region is highly undesirable for spin injection[174]. Spins are

injected into a high-resistive region of the semiconductor that is depleted of carriers. The presence of an energy barrier degrades the performance of the spin-injecting structure, and the current spin polarization strongly depends on the barrier height. The tunneling probability T^t of electrons from the magnetic Fe layer to the n-GaAs is proportional to the factor $\exp(-2\frac{\sqrt{2m_e(\phi_B-E)}}{\hbar}\omega)$ with m_e the electron mass, E the electron energy, ϕ_B and ω the Schottky barrier height and width, respectively. T^t strongly depends on the Schottky barrier width and height. The high barrier and wide depletion region make electrons tunneling nearly impossible. We expect tunneling in the Fe/SI-GaAs (09-A1) to be negligible at zero bias.

In contrast to the Fe/semi-insulating GaAs (09-A1), the Schottky barrier in Fe/n-GaAs (10-A1) is greatly narrowed to ~ 20 nm because of the heavy doping. The narrow barrier makes tunneling possible, although the tunneling rate with zero bias is small. Due to the spliting of the Fe conduction band, the current density j flowing from the magnetic Fe layer is split into $j_\uparrow$ and $j_\downarrow$ with $j = j_\uparrow + j_\downarrow$. The tunneling current density $j_{\uparrow,\downarrow}$ depends on the density of states on either side of the barrier[175, 176]:

$$j_{\uparrow,\downarrow} = \frac{4\pi e}{\hbar} \sum \int_{-\infty}^{\infty} dE [g_{\uparrow,\downarrow}^i(E)f(E)] T_{\uparrow,\downarrow}^t(E)[g_{\uparrow,\downarrow}^j(1 - f(E - eV))] \quad (5.4)$$

where carriers are tunneling from i to j, $g(E)$ is the density of states, $f(E)$ is the Fermi-Dirac distribution, and $T^t(E)$ is the barrier dependent tunneling probability. The sum is taken over all the transverse momentum k_x, k_y states. The polarization of the injected current density α_o is defined as

$$\alpha_o = \frac{j_\uparrow - j_\downarrow}{j_\uparrow + j_\downarrow} \quad (5.5)$$

α_o is explicitly dependent on $g_{\uparrow,\downarrow}^{i,j}$ available to tunneling, which can change with the applied voltage.

The spin diffusion length is defined as $l = \sqrt{D\tau_s}$ where D and τ_s are the electron diffusion coefficient and spin relaxation time, respectively. D can be evaluated by Einstein equation $D = \frac{\mu_e k_B T}{e}$ with μ_e the mobility of the conduction electron. In n-GaAs (09-B2), μ_e at room temperature is ~ 2300
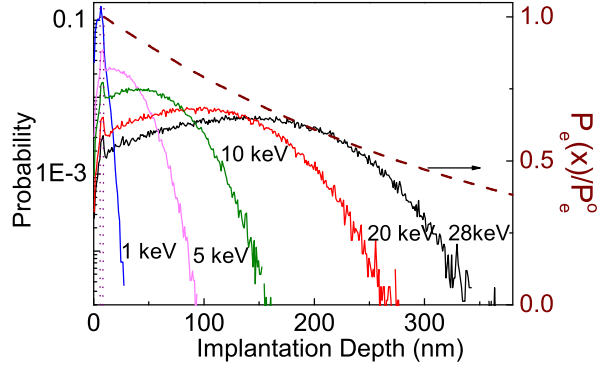
Figure 5.5: The spin polarization decay as a function of $\bar{z}$ (the dashed wine line), in comparison with the $^8\text{Li}^+$ stopping distribution simulated by SRIM.

$\text{cm}^2\text{V}^{-1}\text{s}^{-1}$. The spin lifetime of electrons in the conduction band of n-GaAs is known to be as long as ~ 100 ns in a small doping window around 10^{16} cm^{-3} at low temperature, falling off precipitously for higher dopings[177]. It is suggested that 15 ps $< \tau_s <$ 35 ps at room temperature for a heavily doped n-GaAs with the doping concentration of 2×10^{18} cm^{-3}[178]. The spin diffusion length l is thus estimated to be ~ 400 nm at 300 K. As temperature decreases, D decreases but τ_s, weakly dependent on T, slightly increases[14]. The spin diffusion length l depends on the competition between these two factors at low temperature. The electron spin polarization density $P_e = \frac{n_\uparrow - n_\downarrow}{n_\uparrow + n_\downarrow}$ decays exponentially with $\bar{z}$ the distance from the interface at a length scale of l[14]:

$$P_e(\bar{z})/P_e^o = \exp(-\bar{z}/l) \tag{5.6}$$

where P_e^o is the spin polarization at the interface. Fig. 5.5 shows the decay of the spin polarization density $P_e(\bar{z}) = \frac{n_\uparrow - n_\downarrow}{n_\uparrow + n_\downarrow}$ together with the $^8\text{Li}^+$ implantation distribution by SRIM simulation. The spin polarization is maximum P_e^o at the interface where the tunneling happens, and $^8\text{Li}^+$ would detect the strongest effect (via resonance shift and broadening). With full implantation energy, $\bar{z}$ is ~ 130 nm from the interface, and $P_e(\bar{z})$ decreases to $\sim 50\%$ of P_e^o. The resonance spectrum may be less shifted but more broadened compared with the resonance spectrum at low implantation energy.

Now we consider the case with nonzero injection current. When a bias voltage is applied, non-equilibrium spin polarization accumulates near the interface. The accumulation layer is either expanded or shrunk, depending on the direction of the bias voltage. Under reverse bias, electrons tunnel into GaAs from the Fe contact, and the accumulation layer is extended as drift and diffusion transport electrons into the bulk of the GaAs. As the bias voltage increases, the spin polarization density P_e increases as more polarized electrons are injected. However, the accumulation layer is also expanded to balance the increase in the total number of injected spins. Therefore the actual density of spin-polarized electrons P_e saturates for large reverse bias voltage. The time-averaged inhomogeneous magnetic field generated by the spin polarized injected electrons may be picked up by the resonance of $^8\text{Li}^+$ in the n-GaAs substrate, as shown in Fig. 5.5. The interaction between the $^8\text{Li}^+$ probe and the injected electrons should be affected by the density of spin-polarized electrons as was the case in $\text{Ga}_{1-x}\text{Mn}_x\text{As}$ (Chapter 4). Therefore we can expect the resonance taken at a certain penetration depth to shift as a function of the bias voltage and this shift should saturate at high reverse bias voltage.

Under forward bias, on the other hand, electrons are pushed towards the Fe layer, counter to the direction of spin diffusion, therefore the accumulation layer of polarized electrons shrinks. The resonance shift of $^8\text{Li}^+$ in GaAs may not be able to be detected at the same penetration depth.

5.2   β-NMR Study on Zero-Biased Fe/GaAs Heterostructures

As discussed in last section, a high Schottky barrier and the wide depletion region at the Fe/GaAs interface is detrimental to spin injection[174]. In Fe/SI-GaAs (09-A1), the wide Schottky barrier due to the low carrier density makes electron tunneling almost impossible at zero bias. Therefore, there is little chance to observe any thermal equilibrium injection from the iron layer into the SI-GaAs substrate. In Fe/n-GaAs (10-A1), the Schottky barrier is

greatly reduced to ~ 23 nm due to the high doping density, making the electron tunneling easier even at zero bias, but the tunneling probability may still be small. The spin diffusion length is estimated to be ~ 400 nm at room temperature. As long as the spin polarization is big enough at the interface, $^8Li^+$ should be able to detect it even with full implantation energy.

All β-NMR resonance measurements were taken in CW mode in 2.2 T. The $^8Li^+$ resonance spectra are fit to a single Lorentzian using Eqn. (2.16). The resonance shift is calculated with respect to the resonance frequency of $^8Li^+$ in MgO at 300 K by Eqn. (2.13), and corrected for demagnetization effect.

5.2.1 β-NMR on Fe/Semi-Insulating GaAs

In these preliminary experiments, measurements are all done with zero current. We use the narrow SI-GaAs resonance to detect changes in the local magnetic environment to map the depletion region. Following this line, we took implantation energy scans in 2.2 T at 240 K, 150 K, 60 K and 10 K, which are all far below the Curie temperature of Iron ($T_C = 1043$ K), and a temperature scan at the full implantation energy of 28 keV. As discussed in Chapter 2, any changes of the static local magnetic field would be detected by the ^8Li resonance for the Li stopping in the GaAs substrate.

Figure 5.6 shows the depth-dependent scans at 240 K, 150 K and 10 K, respectively. At 240 K and 150 K, the resonance does not shift, but it broadens as the implantation energy *decreases*, i.e. ^8Li stops closer to the interface. The energy dependence of the resonance changes below 150 K, *e.g.* at 10 K there is a significant resonance shift as a function of implantation energy, as shown in the bottom panel of Figure 5.6. The resonance is negatively shifted as the beam stops deeper in the GaAs substrate. With the full implantation energy (28 keV), the resonance is shifted by 1 kHz, corresponding to a field ~ 1.6 G lower than the external field. Comparing to the β-NMR resonance in the bare SI GaAs substrate (09-B1) (Section 3.3), the resonance position in Fe/SI-GaAs with the full implantation energy at 10 K shifts ~ -22 ppm to a lower frequency. At all temperatures, the baseline
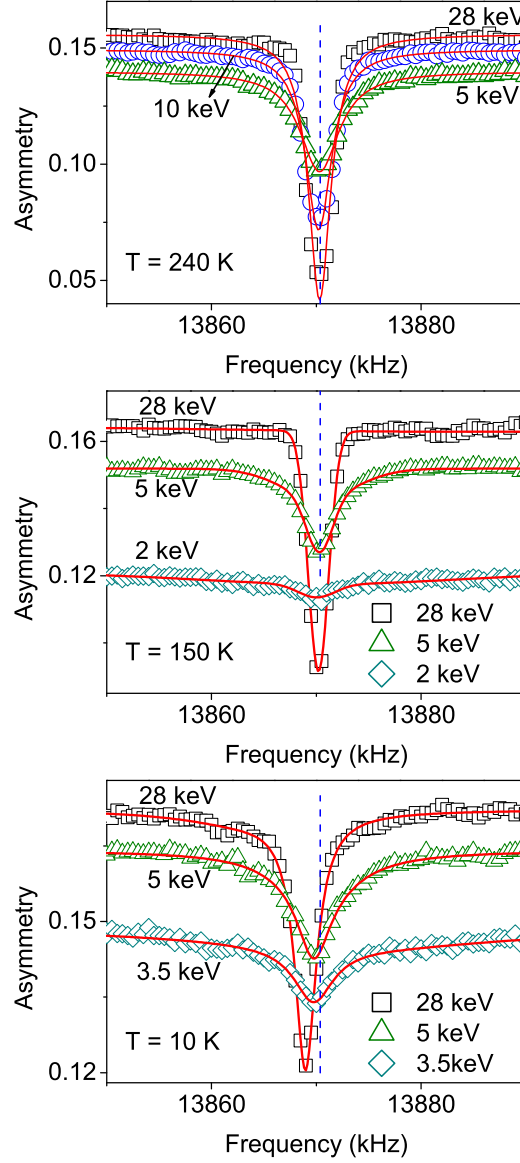
Figure 5.6: Implantation energy dependence of βNMR spectra in the sample Au/Fe/GaAs at 240 K (top), 150 K (middle) and 10 K (bottom) at zero injected current. At 240 K and 150 K, the resonance does not shift as a function of energy, but it broadens as the implantation energy decreases, i.e as the ^{8}Li$^+$ moves closer to the Fe interface. At 10 K, the resonance is negatively shifted as the beam stops deeper into the GaAs substrate. The blue dashed line indicates the position of the resonance in MgO.
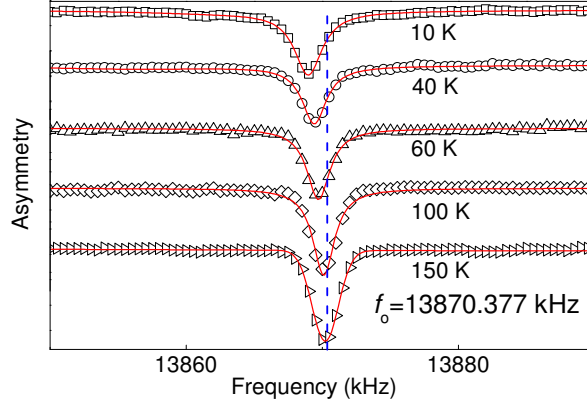
Figure 5.7:   Temperature dependence of β-NMR spectra in the sample Au/Fe/GaAs at the full implantation energy. The resonance shifts negatively as the temperature decreases and broadens slightly at low temperature. Spectra are offset for clarity.

asymmetry of the resonance systematically decreases as the implantation energy decreases.

The temperature-dependent spectra are shown in Figure 5.7. The resonance starts to shift to a lower frequency below 150 K and broadens as the temperature decreases. Similar temperature dependence was also observed in bare SI GaAs (09-B1) (Section 3.3), but the resonance shift in Fe/SI-GaAs (09-A1) is more negative than in the bare SI-GaAs substrate (09-B1).

The analysis of the spectra in Au/Fe/SI-GaAs (09-A1) is shown in Fig. 5.8, together with β-NMR results in the SI-GaAs (09-B1) and heavily doped n-type GaAs crystals (09-B2) (discussed in Section 3.3) for a direct comparison. All shifts have been corrected for the demagnetization effect[115]. In the left panel, the resonance shifts significantly below 150 K and increases as the beam stops deeper in the GaAs not only in the Fe/GaAs (09-A1) but also in the SI-GaAs (09-B1).

The temperature dependence of the shift and width is shown in the right panel of Figure 5.8. The Fe/SI-GaAs (09-A1) shows a temperature dependence similar to that in the bare SI-GaAs (09-B1), while the shift is slightly more negative, indicating that the temperature dependent shift *is*
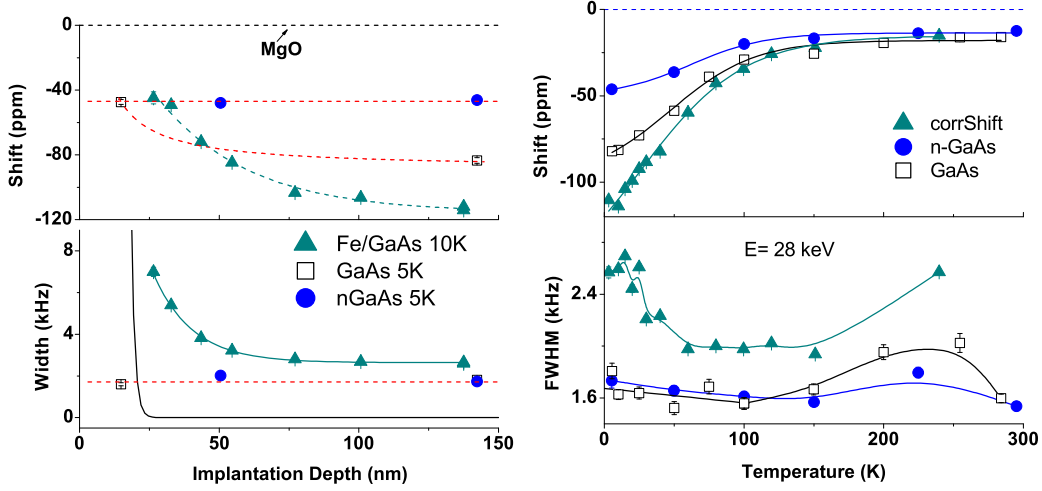
Figure 5.8: Implantation depth- (left panel) and temperature- (right panel) dependence of the frequency shift (top) and width (bottom) in Fe/GaAs (09-A1) (open black squares), SI-GaAs crystal (09-B1) (open blue circles) and n-type GaAs (09-B2) (solid red triangles).
Left: For both the Fe/GaAs and SI-GaAs, the resonance shift only appears below 150 K and increases as the beam stops further from the interface/surface. In contrast, the resonance shift is depth independent in the heavily doped n-GaAs. The resonance broadening observed in Fe/GaAs is slightly temperature dependent, while the resonance line shape in both SI-GaAs and n-type GaAs does not vary with the implantation energy.
Right: The spectra are measured with full implantation energy (28 keV). The shift appears to be characteristic to the GaAs, but the broadening does not.

intrinsic to GaAs. More discussion on the ^{8}Li$^+$ resonance in GaAs substrates was presented in Section 3.3.3.

5.2.1.1 *β-*NMR **Resonance Shift of ^{8}Li$^+$ in Fe/SI-GaAs (09-A1)**

As a function of temperature, at the full implantation energy of 28 keV, the resonance shift is qualitatively similar to the bare SI-GaAs (09-B1). Possible origins of this shift was discussed in Section 3.3.3. There is a significant difference in the shift only below 50 K, with the shift in the Fe capped sample being ∼ 20 ppm more negative. At low temperature (5 – 10) K, the

implantation depth dependence of the shift is also qualitatively similar to the bare substrate, though the data are sparse.

It is unlikely that the difference in the shifts is related to the magnetism of Fe, since the temperature and energy dependence are so similar to the bare SI-GaAs (09-B1).

Let's consider the possibility that the shift is due to a depletion region in the SI-GaAs. This requires that the bare substrate (SI-GaAs with its native oxide) have a similar interfacial behavior to the Fe/SI-GaAs heterostructure. As already discussed in Section 3.3.3, the surface states in the GaAs makes the energy band bend up near the GaAs surface, forming a surface barrier of the width similar to that in the Schottky barrier in Fe/SI-GaAs (09-A1) interface[117], so this is at least a reasonable possibility.

Such an interpretation would be consistent with the absence of a depth dependence in the heavily doped n-GaAs (see the solid blue circles in the left panel of Fig. 5.8) where screening limits electrostatic band bending effects to very near the interface.

Now let's consider whether the magnetic field due to the Fe layer could account for the shift. Inside the Fe layer, the net dipole field due to a thin Fe layer is just the demagnetization field B_{demag} discussed in Section 4.4.3. Outside of the Fe, at a distance much smaller than the transverse film dimension, this proximal field B_p is uniform and can be estimated as[115]:

$$B_p = \xi 4\pi M \tag{5.7}$$

where ξ is the aspect ratio of the film (thickness to transverse dimension), which is on the order of 3nm/4mm $\sim 10^{-6}$, and M is the magnetization of Fe. Considering that the 2.2 T is high enough to saturate its magnetization, we use $M_s = 1630$ emu/cm^3 the saturated magnetization value of Fe[179] to estimate B_p. The proximal field B_p inside the GaAs is: $B_p = 10^{-6} \times 4\pi \times 1630 \approx 0.02$ G, corresponding to a shift of ~ 1 ppm, which is too small for the observed extra shift. B_p is also independent of temperature since T_C of Fe is far above room temperature, so it can not explain the extra shift that is only observed below 150 K.

5.2.1.2 Resonance Broadening of ^{8}Li$^+$ Resonance in Fe/SI-GaAs (09-A1)

The resonance spectra of ^{8}Li$^+$ in both SI-GaAs (09-B1) and heavily n-type doped GaAs (09-B2) were taken in pulsed mode (Section 3.3) which is good to measure narrow resonance of only a few kHz wide, while the spectra in Fe/GaAs is CW mode suitable for wide resonance, which is power broadened by the rf field. Therefore the linewidths are substantially different as shown in Fig. 5.8.

In contrast to the shift, the energy-dependent broadening appears related to the Fe overlayer: it increases with decreasing energy and is absent in both the bare semi-insulating GaAs and the n-type GaAs. Such a broadening is likely the result of an inhomogeneous local magnetic field in the region sampled by ^{8}Li$^+$. As discussed in the last section, B_p is uniform outside the Fe layer if the film is perfectly flat. However, for a non-ideal film with interface roughness (right panel of Fig. 5.1), the dipole field can give rise to an inhomogeneous field outside the film. We can estimate the linewidth in the GaAs due to the Fe/GaAs interface roughness, assuming that the atomic terrace on the Fe/GaAs interface is approximately 3-4 nm wide on average[169]. In the high field of 2.2 T, the magnetization Fe layer is aligned parallel to the applied field. For a thin magnetic layer with a periodically corrugated magnetization, the broadening due to the interface roughness ($\sigma_{roughness}$) falls exponentially with $\bar{z}$ the distance away from the interface, depending on the transverse corrugation wavelength λ^c[115]:

$$\sigma_{roughness} \propto \exp(-\frac{2\pi\bar{z}}{\lambda^c}) \tag{5.8}$$

The rough interface can be related to the idealized periodic corrugation in the following way. Consider traversing the rough interface in a transverse direction, the magnetization will vary between the extremes of the saturation magnetization of the Fe ($M_S = 1630$ emu/cm^3[179]) and $\sim$ zero in the GaAs. While we do not expect a single wavelength for the interface roughness, there may be some characteristic length scale. In fact, the GaAs surface upon which the Fe is grown is a vicinal surface, meaning that it is constituted

120

of a set of unit cell high terraces that make the surface a shallow staircase with a direction slightly off the $\langle 100 \rangle$ crystal direction. Characterization during growth on similar samples reveals such terraces are $\lambda^c \sim 3 - 4$ nm wide. While this does not constitute a periodic transverse structure, it would perhaps correspond to a prominent Fourier component in the real interface roughness. We can thus coarsely estimate the interface as a sinusoid:

$$M(x) = M_s \cos(\frac{2\pi x}{\lambda^c}) \tag{5.9}$$

with x a direction in the plane of the film. In reality, the roughness will contain a broad range of Fourier components. With this approximation, the broadening $\sigma_{roughness}$ can be estimated as:

$$\sigma_{roughness} \approx \gamma M_s \exp(-\frac{2\pi \bar{z}}{\lambda^c}) \tag{5.10}$$

and shown in the bottom left panel of Fig. 5.8 (the black curve). It is large close to the interface, but falls very quickly to zero away from the interface. From this estimate, even at the lowest penetration depth of $^8Li^+$ in this experiment (~ 27 nm), $\sigma_{roughness}$ is negligible and much smaller than the observed broadening. There might be significant magnetic inhomogeneity in the Fe/GaAs interface on a length scale much longer than the terrace size, however, and we cannot rule this out as the origin of the broadening. However, such a broadening would be independent of temperature, since M_S is approximately constant below 300 K, in contrast to the observed width in Fig. 5.8.

The temperature dependence of the linewidth in Fe/SI-GaAs (09-A1) is typical for $^8Li^+$ in GaAs crystals (Section 3.2). The resonance narrows from 250 K to 150 K and broadens as temperature further decreases. With the implantation energy of 28 keV, $^8Li^+$ stop deep in the GaAs substrate, and feels less effect of the Fe layer. Therefore the temperature dependence of the line width (bottom right panel of Fig. 5.8) resembles pure GaAs[104]. The broadening is not likely due to the inhomogeneous hyperfine field as observed in Ref. [180]. The Schottky barrier in Fe/SI-GaAs (09-B1) is as wide as 100

nm because of the low carrier concentration. $^8Li^+$ even with 28 keV ($d \sim 140$ nm) stops in the barrier region where the conduction electrons are depleted. The lack of conduction electrons makes the hyperfine coupling impossible inside the Schottky barrier. There is no evidence of spin proximity effect observed in the Fe/SI-GaAs.

5.2.2   β-NMR on Fe/n-GaAs

As discussed in Section 5.2.1, the negative shift of the β-NMR spectra in Fe/GaAs is unrelated to the magnetic iron layer, but seems to be an intrinsic property of semi-insulating GaAs. To get rid of the wide Schottky barrier in the interface of Fe/SI-GaAs (09-A1), we could use the heavily doped n-type GaAs as a substrate, since the β-NMR resonance in the heavily doped n-type GaAs (09-B2) has been shown independent of depth in Section 3.3. Therefore, we tested a new sample with the same structure as the one discussed in Section 5.2.1, but using a heavily doped n-type substrate. The β-NMR resonance in Au/Fe/n-GaAs (10-A1) was measured as a function of implantation depth and temperature in CW mode. The corresponding bare substrate (10-B1) was also measured in CW mode as a control experiment. The implantation profile of the beam is shown in the bottom panel of Fig. 5.2, and the Schottky barrier is much narrower than the $^8Li^+$ implantation depth (the dark yellow dash-dot line in Fig. 5.2).

5.2.2.1   Results and Analysis

The implantation depth-dependence of the $^8Li^+$ resonance in Au/Fe/n-GaAs (10-A1) was measured at different temperatures in CW mode. Fig. 5.9 shows the resonance spectra in Fe/n-GaAs (left panel) and n-GaAs (right panel) at 300 K with various beam energies. Compared to the frequency in MgO, the resonance frequency in Fe/n-GaAs shifts to a lower frequency with full implantation energy. As the implantation energy decreases, $^8Li^+$ stop closer to the Fe/n-GaAs interface, and the resonance shifts more negatively and broadens. For comparison, the β-NMR resonance in the n-GaAs substrate (10-B1) at 300 K is shown in the right panel of Fig. 5.9. It nei-
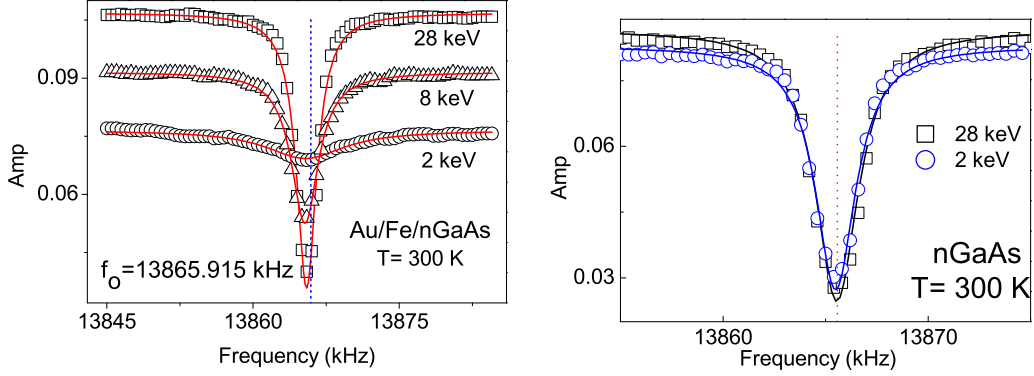
Figure 5.9: Energy dependence of the β-NMR spectra (in CW mode) in Au/Fe/n-GaAs (left panel) and n-GaAs (right panel) at 300 K in the external field of 2.2 T with no current injection. Left panel: The resonance in Fe/n-GaAs shifts more negatively and gets broadened as ^{8}Li$^+$ stops closer to the interface. Right panel: the β-NMR spectra in n-GaAs neither shifts nor broadens as the implantation energy decreases from 28 keV to 2 keV. The dotted lines in each panel indicates the resonance frequency in MgO.

ther shifts nor broadens as the implantation energy changes. This difference indicates that the resonance changes may be the results of the proximity effect of the Fe layer, NOT intrinsic to GaAs.

The analysis of the depth-dependent β-NMR is summarized in Fig. 5.10. As discussed in Sections 2.4.1.1 and 4.6.2, the amplitude of CW mode resonance is not a measure of the ^{8}Li$^+$ fraction, but is affected by both the linewidth and the baseline. We divide the amplitude by its baseline to account for the relaxation effect and multiply it by its linewidth to approximate the area under the resonance A_{norm}^{int} which is plotted in the bottom panel of Fig. 5.10.

In Fig. 5.10, the open blue circles represent the resonance in the n-GaAs substrate (10-B1) which is measured as a control experiment at 300 K with implantation energy of 28 keV and 2 keV. The resonance in the n-GaAs substrate (10-B1) does not vary with implantation energy. At 2 keV, there's no obvious resonance shift or broadening compared to 28 keV at room temperature, and the A_{norm}^{int} is ∼90% of its value at 28 keV. This

123
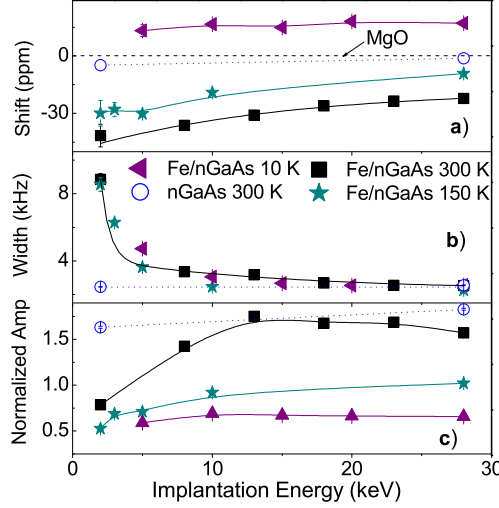
Figure 5.10: The analysis of β-NMR resonance in Fe/n-GaAs (10-A1) as a function implantation energy at different temperatures from single Lorentzian fits. The open blue circles represent β-NMR resonance in the bare n-GaAs substrate (10-B1) at 300 K. The solid symbols refer to the Fe/n-GaAs heterostructure. Curves are guides to the eye.

small reduction may be due to backscattering at lower energy (Section 2.3). Therefore, any resonance changes (shift or broadening) in the Fe/n-GaAs heterostructure (10-A1) can be attributed to the effect of the magnetic Fe layer.

As shown in the top panel of Fig. 5.10, the resonance shifts negatively as ^{8}Li$^+$ stop closer to the Fe/n-GaAs interface. When the temperature is reduced, the resonance moves to higher frequencies, and becomes less depth-dependent. The resonance width as a function of implantation energy is shown in the middle panel of Fig. 5.10. Compared to the resonance width in the n-GaAs substrate (10-B1) (open blue circles), the ^{8}Li$^+$ resonance in Fe/n-GaAs remains narrow when the implantation energy is above 13 keV (the average implantation depth $d \sim 70$ nm), and is substantially broadened at lower energies. The resonance broadening is also slightly temperature dependent. For example, at 5 keV, the resonance is slightly more broadened at 10 K (solid purple triangle) than that at 150 K (solid cyan star).
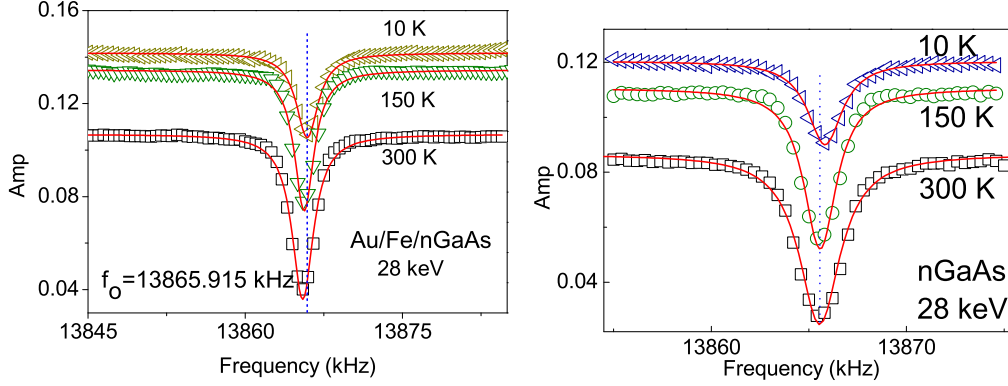
Figure 5.11: Temperature dependence of the β-NMR spectra (CW mode) in Au/Fe/n-GaAs (left panel) and n-GaAs (right panel) with full implantation energy (28 keV) in 2.2 T magnetic field. The dotted blue lines indicate the resonance frequency in MgO. In both panels, the resonance positively shifts and broadens as temperature decreases. The increasing baseline suggests a slower relaxation at lower temperatures, which is consistent with results of independent spin lattice relaxation (SLR) measurements[104].

A_{norm}^{int} is shown in the bottom panel of Fig. 5.10. At room temperature, it remains approximately constant when the implantation energy is above 13 keV ($d \sim 70$ nm). Then it starts to decrease with reduced implantation energy. At 2 keV ($d \sim 20$ nm), A_{norm}^{int} is only ~ 50 % of its value measured with full implantation energy. At low temperatures (for example 10 K, the purple triangles in the bottom panel of Fig. 5.10), the amplitude decreases with implantation energy, but the amplitude loss is much less than at room temperature.

Now we present the temperature dependence of the resonance. The T-dependent β-NMR spectra in Fe/n-GaAs (10-A1) (left panel) and in the n-GaAs substrate (10-B1) (right panel) are shown in Fig. 5.11 as a function of temperature with the implantation energy 28 keV. In both panels, the resonance shifts positively and broadens as temperature decreases. The increasing baseline indicates a decreasing relaxation rate of $^8Li^+$ at lower temperatures.

The results of the analysis of T-dependent β-NMR resonance in both
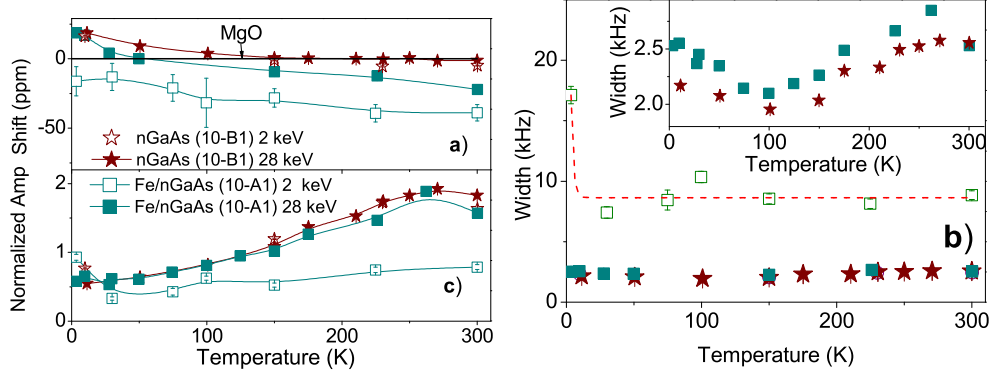
Figure 5.12: The temperature-dependence of the resonance shift (left panel) and width (right panel) of β-NMR spectra in Au/Fe/n-GaAs (blue squares) and n-GaAs (red stars). The lines are guides to the eye.

Fe/n-GaAs (10-A1) and the bare n-GaAs substrate (10-B1) are summarized in Fig. 5.12. The amplitude is again converted into A_{norm}^{int} by multiplying by the resonance width and diving by the baseline to account for different relaxation rates and linewidths(Section 2.4.1.1). The shift in the n-GaAs substrate (10-B1) differs from the results presented in Section 3.3.2.2. It moves positively as temperature decreases, which is in contrast to the shift in the other n-GaAs (09-B2) (Section 3.3.2.2), but the temperature dependence of the width resembles: slightly decreasing from 5 K to 100 K and broadening above 150 K. Note that unlike n-GaAs (09-B2) (from AXT Inc, USA), the substrate used in Fe/n-GaAs (10-A1) is from another provider (Wafer Technology Ltd., UK). The positive resonance shift may be sample-dependent. Comparing with the bare n-GaAs substrate (10-B1), the resonance in Fe/n-GaAs (10-A1) with full implantation energy shifts a little less positively and is slightly broader (inset of Fig. 5.12 right panel).

At 28 keV, $^8Li^+$ stop deep in the n-GaAs substrate. The influence of the Fe capping layer is observable, but small. The A_{norm}^{int} in Fe/n-GaAs (10-A1) is approximately the same as that in n-GaAs (10-B1) through all temperatures. When the implantation energy is 2 keV, $^8Li^+$ stop much closer to the interface ($d \sim 20$ nm). The effect of the magnetic Fe capping layer is more obvious with a more broadened resonance and the loss of the A_{norm}^{int}

126

(open cyan squares in Fig. 5.12). The resonance shifts slightly upwards as temperature decreases. The resonance width is approximately a constant from room temperature to 30 K and significantly broadened below 30 K. The A_{norm}^{int} is approximately a constant through all temperatures.

5.2.2.2 Discussion

Here we discuss the results in the Fe/n-GaAs heterostructures without any injected current that are presented above.

The change in the resonance shift could be possibly caused by a) the dipolar field of the Fe layer, b) the demagnetization field of Fe atoms diffused into the n-GaAs substrate, or c) the spin-polarized electrons tunneling from Fe into the n-GaAs substrate. Now we consider them separately.

As already estimated in last section (Section 5.2.1.1), the dipolar field generated by the magnetic Fe layer B_p is only ~ 0.02 G, negligible compared to the observed shift in the top panel of Fig. 5.10, so it cannot account for the observed shift.

We discussed in Section 5.1.1 that Fe may diffuse into GaAs forming a intermix layer. Any iron that diffuses into the n-GaAs substrates behaves as a paramagnetic impurity, like the Mn ions in GaAs (Chapter 4). Any $^8\text{Li}^+$ stopping close to it will feel its dipolar field likely resulting in a loss in A_{norm}^{int}. The primary effect of the dipolar fields of dilute random magnetic impurities is a broadening of the resonance (see Chapter 4). They can cause a shift, but only via their net demagnetization field, which is estimated above to be really small. Moreover, a broadening or shift from this source would follow a Curie Law with temperature unlike the data. Therefore, we can rule out this possibility as the main contribution of the observed shift.

Another possibility is that electrons are traversing the barrier spontaneously. With zero current, this means that the rate of electrons tunneling to the GaAs must equal the rate returning to the Fe. Such a process in a superconductor/normal metal system gives rise to the superconducting proximity effect, where the superconducting order is transferred to the normal metal by the exchange of electrons. In a similar way, we may find spin

polarization is transferred to the semiconductor.

As shown in Fig. 5.5, if there are electrons tunneling from the Fe layer, the spin polarized electrons could drift into the n-GaAs substrate and interact with ^{8}Li$^+$ stopping at different depths. It is possible that such electrons result in the depth dependence of ^{8}Li$^+$ resonance. The spin diffusion length l is estimated to be ~ 400 nm in n-GaAs at room temperature. The spin polarization density $P_e(\bar{z})$ decreases exponentially with $\bar{z}$ the distance from the interface (Eqn. (5.6)). The inhomogeneous magnetic field generated by the spin-polarized injection electrons scales with $P_e(\bar{z})$, leading to the shift changes exponentially with $\bar{z}$. We fit the depth-dependent resonance shift at room temperature (the solid black squares in the top panel of Fig. 5.10) to Eqn. (5.6), resulting a length scale $l = 57$ nm, which is much shorter than the spin diffusion length estimated above.

The temperature dependence of the resonance shift in Fe/n-GaAs (10-A1) is shown in Panel a) of Fig. 5.12. At 28 keV, the slight positive shift and the temperature dependence of the width appear to be the intrinsic properties of the n-GaAs substrate, rather than a result of the Fe layer. The decrease of A^{int}_{norm} in Fe/n-GaAs with temperature is also due to the n-GaAs substrate. The resonance shift in Fe/n-GaAs (10-A1) is approximately the same as in n-GaAs (10-B1). There is no sign of spin-polarized electrons tunneling from the Fe layer in the n-GaAs. At 2 keV, ^{8}Li$^+$ stop very close to the interface ($\bar{z} \sim 11$ nm). P_e is $\sim 0.96 P_e^o$ using Eqn. (5.6), significantly increasing the possibility that ^{8}Li$^+$ can detect the inhomogeneous field generated by the spin-polarized electrons, assuming that spin-polarized electrons could tunnel from the magnetic Fe layer into the n-GaAs substrate and be detected by the ^{8}Li$^+$. Since both the electron injection rate and diffusion length increases at low temperatures[12], the resulting inhomogeneous field should be larger and the resonance may shift more at low temperature. However, this is not the case in Fe/n-GaAs (10-A1). The resonance shift is approximately constant through all temperatures, and we have no evidence for spin polarized electrons from the Fe layer at the penetration depth of ~ 20 **nm**.

Now we turn to the resonance broadening observed in Fe/n-GaAs (10-

A1). Compared with the resonance in n-GaAs (10-B1), the additional broadening in Fe/n-GaAs (10-A1) (middle panel of Fig. 5.10 and left panel of Fig. 5.12) is due to the magnetic Fe layer.

There are several possible broadening mechanisms. One possibility is the Fe/GaAs interface roughness. As discussed in the last section, the broadening caused by the imperfect interface falls exponentially (Eqn. (5.10)) with a lengthscale determined by the transverse wavelengths of the roughness. The Fe/n-GaAs sample (10-A1) is fabricated in the same way as Fe/SI-GaAs (09-A1), and is likely similar in the interface roughness. We already showed that the roughness caused a broadening that falls too quickly to explain the observation if the length scale of the terrace size is relevant (Fig. 5.8).

Another possibility is the diffusion of Fe atoms into the n-GaAs substrate. Any Fe atom diffuses into GaAs substrate and takes the Ga site or interstitial site as a paramagnetic impurity much like the Mn^{2+} in Chapter 4, causing a distribution of local fields due to the varying distances of random $^8Li^+$ sites. In this case, the broadening scales with temperature as $1/T$, which is consistent with the data shown in Panel b) of Fig. 5.12 though the data are sparse. One could estimate the dipolar broadening due to dissolved dilute Fe atoms in GaAs as we did in Chapter 4, but one would need an estimate of its concentration and depth distribution that is beyond our abilities to establish at present.

Spin-polarized electrons tunneling from the Fe layer into the GaAs could also contribute to the resonance linewidth, *e.g.* an unresolved oscillatory response in metallic n-GaAs like in the Ag[180]. However, although the Fermi surface in the metallic n-GaAs is much smaller than that of Ag, which makes the oscillatory wavelength long, the carrier density is so low that the amplitude of the oscillation may be too small to detect compared with that of Ag[180].

In summary, no spin injection is observed in either Fe/SI-GaAs (09-A1) or Fe/n-GaAs (10-A1) at thermal equilibrium under zero bias. The Schottky barrier in the Fe/SI-GaAs interface makes the tunneling almost impossible. Although the high doping of n-GaAs substrate greatly reduces

Figure 5.13: "Edge-on" view on the sample with current contacts. Left: the geometry of the sample contacts labeled with the thickness of each layer. Right: the circuit setup. For positive current as shown, the current is flowing from the n-GaAs substrate to the Fe layer.

the Schottky barrier width, no strong evidence of spin polarization is found in the GaAs. The temperature- and depth- dependence of the resonance shift in both Fe/SI-GaAs (09-A1) and Fe/n-GaAs (10-A1) appear to be intrinsic properties of the GaAs substrates.

5.3 Spin-Polarized Current Injection Measurement

After carefully measuring β-NMR of ^{8}Li$^+$ in Fe/GaAs heterostructure with semi-insulating and heavily doped n-type GaAs substrate without any current, we are ready to inject current from the magnetic Fe layer into the semiconductor GaAs substrate to see if we can affect the resonance. As reviewed in Section 5.1.4, the Schottky barrier is crucial for efficient spin injection. So we used the sample Fe/n-GaAs, grown in the same way as the one used in Section 5.2.

5.3.1 Experimental

First I summarize the extra sample preparation required for the current injection experiments.

Two thick gold (Au) contacts were deposited onto the top and back side of the sample by thermal evaporation at UBC. The sample geometry and experiment setup are shown in detail in Appendix D. To help the 200 nm
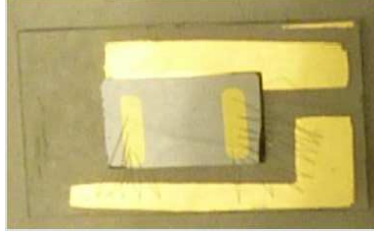
Figure 5.14: The beam view of the sample glued to the sapphire plate (8×15 mm $\times$ mm) using Ag paint. There are 2 Au pads on the surface of the sapphire plate to make electric connection of the sample.

Au contact at the back side of the substrate (see the left panel of Fig. 5.13) better bond to the n-GaAs substrate, a thin titanium (Ti) layer ~ 2 nm thick was thermally evaporated onto the n-GaAs substrate backside before the Au layer. The geometry of the sample contacts is shown in the left panel of Fig. 5.13. The sample is attached to a sapphire plate with two Au pads on top to complete the electric circuit. The Au pads on the sapphire plate are ~ 200 nm thick and also thermally evaporated. More details of sample preparation and experiment setup are given in Appendix D and Appendix C. A picture of the sample is also shown in Fig. 5.14.

The Au contacts are connected to a current source as shown in the right panel of Fig. 5.13. The positive current is defined as injected from the backside of the sample (the n-GaAs substrate) to the top surface (the Fe thin film) and accordingly the electrons move from the Fe layer to the n-GaAs substrate. In this case, the Au/Fe/n-GaAs junction is reverse biased, so that the Schottky barrier is highly resistive, like a diode under reverse bias. On the other hand, the current is defined negative when the structure is forward biased with electrons moving from the n-GaAs substrate to the Fe layer. In this case, the current increases quickly with the forward bias voltage. The I-V characteristic curve is shown in Fig. 5.4 and discussed in Section 5.1.3.

The equivalent resistor network of the Fe/n-GaAs (11-A1) with contacts is shown in Fig. 5.15. The solid arrow represents the direction of positive current under positive voltage and the big open arrow is the direction of the
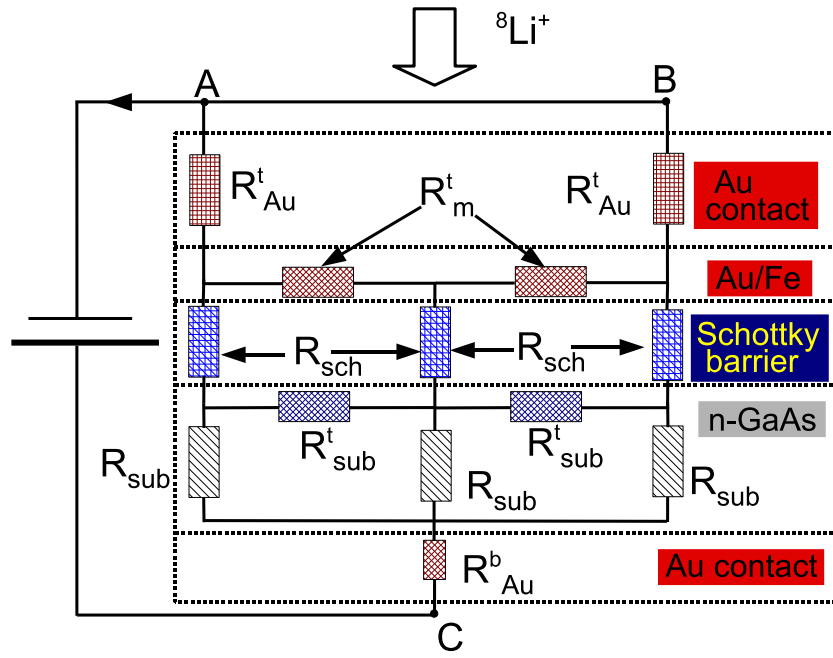
Figure 5.15: A diagram of the equivalent resistor network of the sample including contacts.

incident ^{8}Li$^+$ beam. Note that the sample with a positive current is actually reversely biased. R^t_{Au} and R^b_{Au} are the resistance of top and bottom gold contacts respectively, and are estimated to be on the order of 10^{-8} Ω using their dimensions and a standard value for the resistivity of Au. R^t_m is the resistance of the transverse gold and iron thin films, which is estimated to be $\sim$ 3 Ω. R_{sub} and R^t_{sub} are the vertical and transverse resistance of the n-GaAs substrate, respectively. The n-GaAs substrate is highly Si doped with a low resistivity of $\sim$ 2.8 $\times 10^{-3}$ Ωcm. Therefore R_{GaAs} is estimated to be on the order of 10^{-4} Ω and R^t_{GaAs} is about 0.08 Ω. All estimations are based on the resistivity of each material at room temperature. R_{sch} represents the resistance of the Schottky barrier, and is estimated to be $\sim$ 9Ω at 77 K from 4-wire measurement data shown in Section 5.1.3. Other sample resistance was measured with a multimeter at room temperature. The gold contact resistance is negligibly small, so there's no voltage drop on the gold contact. The resistance transverse through the film R_{AB} is $\sim$ 1.2 Ω, and the total resistance between Point A and Point C R_{AC} is $\sim$ 8.7 Ω, much higher than R_{AB}. So the current will be uniform over the whole sample area at the Schottky barrier.

The spin polarized electrons could tunnel through the reverse biased Schottky barrier or pass over it if the bias voltage is high enough. The applied current could be remotely controlled between $\pm$ 500 mA with a resolution of 1 mA supplied by the "0937 current source" built at TRIUMF. With the sample geometry shown, the current density $j \approx 2 \times 10^4$ A/m^2 at +500 mA. We expect that the injected electron spin polarization in the GaAs could be detected by the local probe ^{8}Li$^+$ via their effect on the time-averaged local magnetic field in the GaAs.

We carefully measured the ^{8}Li$^+$ spectra in Fe/n-GaAs (11-A1) as a function of injected current with the implantation energy of 20 keV and 10 keV, and also its temperature dependence with the implantation energy of 20 keV in CW mode at 2.2 T.
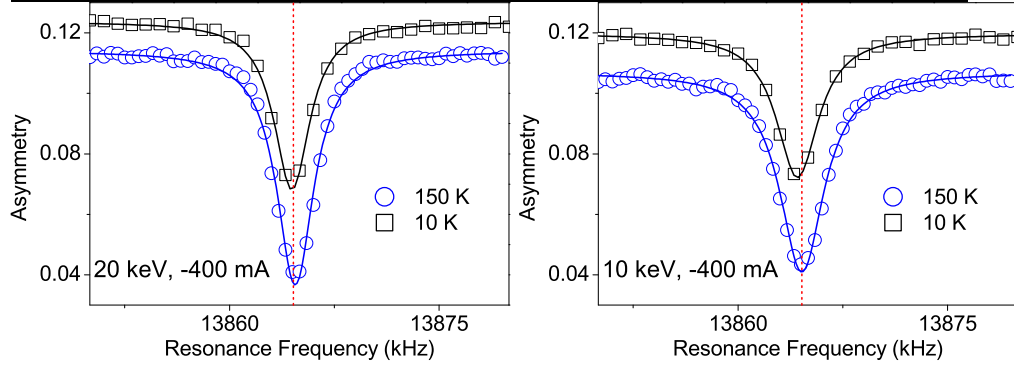
Figure 5.16: The temperature dependent ^{8}Li$^+$ spectra in the Au/Fe/n-GaAs heterostructure with the current of -400 mA and implantation energy of 20 keV (left) and 10 keV (right) in 2.2 T field. In both panels, the resonance at 150 K slightly shifts to a lower frequency and is broadened. The red dotted line indicates the resonance frequency of ^{8}Li$^+$ in MgO.

5.3.2 Temperature Dependence of ^{8}Li$^+$ Resonance in Fe/n-GaAs with Current Injection

For comparison, the ^{8}Li$^+$ spectra as a function of temperature are plotted in Fig. 5.16 with an applied current of -400 mA and the implantation energy of 20 keV (left panel) and 10 keV (right panel). In both panels, the spectrum at 10 K shifts negatively and slightly broadens compared to that at 150 K. We fit each scan in the spectrum to a single Lorentz function, and use the averaged ν_o as the resonance frequency. Its error is calculated as the standard deviation of the resonance frequency divided by the square root of the number of complete frequency scans in the run. The analysis of the spectra in CW mode is summarized in Fig. 5.17.

The resonance frequency stays approximately constant above 150 K, and negatively shifts as temperature decreases below 150 K. Compared to zero current (solid black squares in the left panel of Fig. 5.17), the resonance shifts negatively with positive current (reverse biased), and positively with negative current (forward biased). With zero current, the resonance width decreases from 10 K to 150 K and then increases up to room temperature, which is consistent with the results in GaAs[104]. But with the injected current (open red circles and blue triangles in the right panel of Fig. 5.17),

134
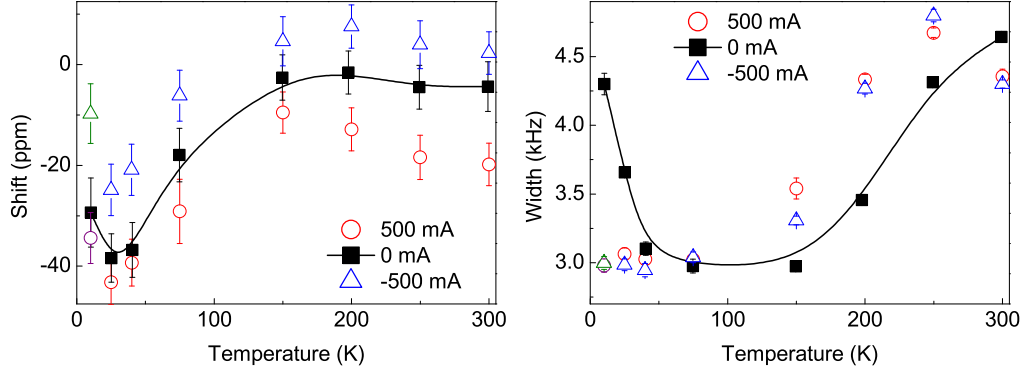
Figure 5.17: The temperature dependent resonance shift (left) and width (right) in Au/Fe/n-GaAs with 20 keV implantation energy with the current of -500 mA (open blue triangles), zero (solid black squares) and +500 mA (open red circles) in the field of 2.2 T. Curves are the guide to the eye.

the resonance linewidth is narrow below 150 K, and broadens above 150 K until 290 K above which it narrows again.

The distinct current dependence of the resonance linewidth below and above 150 K can be attributed to the resistive heating effect of the current. Without current, the width is minimal at about 150 K. Any heating results in a local temperature in the sample that exceeds the thermometer reading. Such a temperature increase will cause line broadening above 150 K. Below 150 K, for example 10 K, the ^{8}Li$^+$ resonance narrows if the sample is locally heated by the injected current.

With $I = -500$ mA current, U the voltage across the sample (between Point A and C in Fig. 5.15) is $\sim$ -1.832 V at 150 K measured *in situ*. The power generated by the current is estimated as $P = UI \sim 1.832\text{V} \times 0.5\text{A} = 0.916$ W. ~ 1 W of power is delivered to the sample by the current. The sample is glued to a sapphire plate with some silver paint at the backside. Although the sapphire plate is tightly bolted to the copper sample holder, and sapphire itself is a good thermal conductor, the power delivered by the current is still higher than the power dissipated through heat conduction to the cryostat. The electric power is dissipated along the sample according to the resistance distribution along the sample, mainly in the resistive Schottky

barrier region, and this heats the sample locally. The local heating results in a sample temperature higher than the temperature read by the thermometer. Note that the thermometers indicating the sample temperature are mounted on the copper enclosure and located on the coldest point of the cryostat which is an ultra-high vacuum (UHV) coldfinger, several centimeters away from the sample. Usually the thermometer reading is accurate within ~ 0.1 K when there is no current. The local resistive heating sets up a dynamic temperature gradient in the sample. At 10 K, by the observed width, the temperature at the $^8Li^+$ appears to be above 50 K with ± 500 mA current. As discussed in Section 3.3.2.2, the width in GaAs is minimal at 150 K and then increases from 150 K to 10 K. In combination with local heating, this characteristic dependence of the width explains the observed width with an applied current. A slightly enhanced width may also be the result of an inhomogeneous stray field due to the geometry of the lead wires (see Section 5.3.3).

5.3.3 Current Dependence of $^8Li^+$ Resonance in Fe/n-GaAs with Current Injection

The resonance spectra as a function of current are shown in Fig. 5.18 with implantation energy of 20 keV (left panels) and 10 keV (right panels) at 10 K (top panels) and 150 K (bottom panels) in 2.2 T. Contrary to expectations, there's only a very small frequency shift and the resonance linewidth changes only slightly as a function of current. The overlapping baselines with different current indicates that the spin relaxation rate does not change significantly with the current. At 10 K, the resonance is slightly narrowed with high injected current, while at 150 K the injected current broadens the resonance linewidth. This is consistent with sample heating effect as discussed above.

Fig. 5.19 shows the spectra as a function of the implantation energy at 10K (left panel) and 150 K (right panel) with -400 mA current. As mentioned in last section, lower implantation energy means $^8Li^+$ stops closer to the interface. The spectra taken with 10 keV (open symbols) are negatively
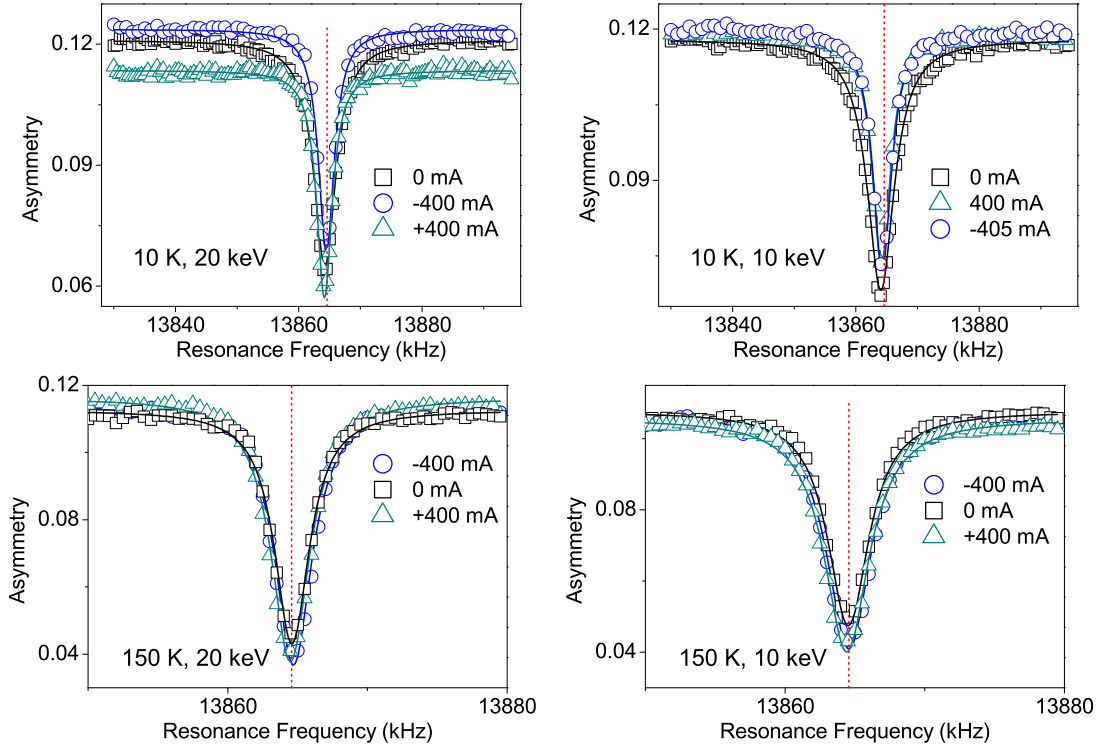
Figure 5.18: The resonance spectra as a function of the current with the implantation energy of 20 keV (left panels) and 10 keV (right panels) at 10 K (top panels) and 150 K (bottom panels) in 2.2 T. The dotted red line indicates the resonance frequency in MgO.
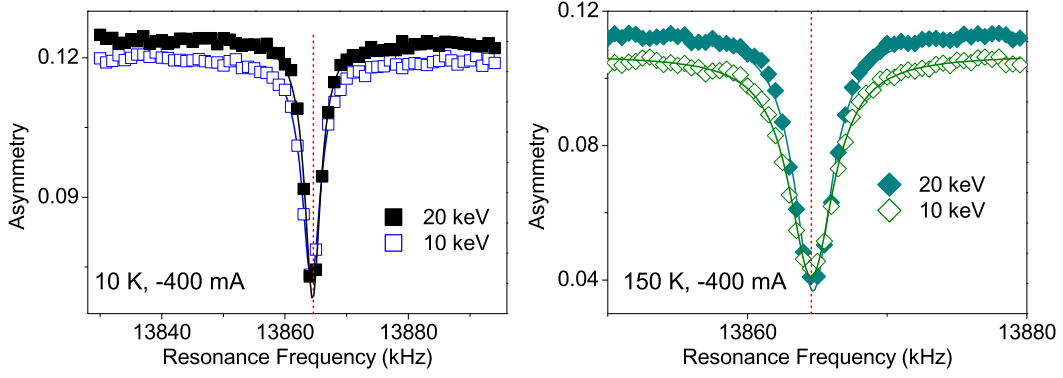
Figure 5.19: The β-NMR spectra in Au/Fe/n-GaAs with 2 implantation energies at 10 K (left) and 150 K (right) with the current of -400 mA in the field of 2.2 T.

shifted and broader than with 20 keV.

The analysis of the spectra in CW mode is the same as discussed in Section 5.3.2, and is summarized in Fig. 5.20. At either 150 K or 10 K, the resonance with 10 keV implantation energy (open squares in Fig. 5.20 left panel) shifts negatively compared to that taken with 20 keV implantation energy. There's only a very small frequency shift as a function of the current at either 150 K or 10 K. At 150 K, the small resonance shifts seems linearly proportional to the current. While at 10 K, the shift only linearly scales with negative current and remains constant with positive current though the error bars are large. Remember that the sample is reverse biased for positive current. That means that the resonance only shifts with current when the sample is forward biased and remains constant when reverse biased. This is different from our expectation. Based on the analysis in Section 5.1.4, we expected that the resonance shifts when reverse biased, and may remain constant when forward biased with full implantation energy.

The resonance shift at 150 K (squares and stars) was fit to a linear function of current with a shared slope, and the fit result is shown in Table 5.1. The shared slope is -0.0162 ± 0.0002 ppm/mA, corresponding to -0.35 ± 0.04 G/A. The y-intercepts, the shifts without any injected current, are -3.4 ± 0.1 ppm for 20 keV and -8.8 ± 0.1 ppm for 10 keV. The relative
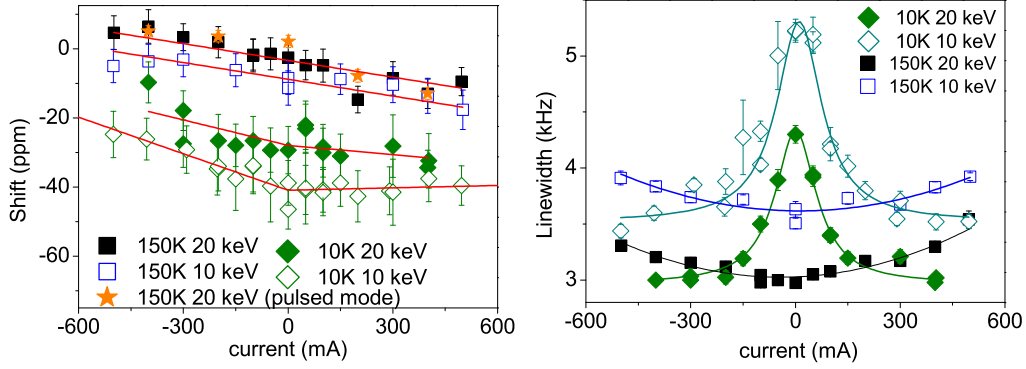
Figure 5.20: The resonance shift (left) and width (right) of $^8Li^+$ resonance as a function of current at 150 K (squares) and 10 K (diamonds) with the implantation energy of 20 kV (solid symbols) and 10 keV (open symbols) in the field of 2.2 T. The peak in the linewidth is attributed to the local heating effect of the current in the GaAs. The linear shift with current appears to be mostly the result of a small stray field.

T (K)	E (keV)	slope (ppm/mA)	constant (ppm)
150	10	-0.0162 ± 0.0002	-8.8 ± 0.1
150	20	-0.0162 ± 0.0002	-3.4 ± 0.1
10	10	-0.0352 ± 0.0006	-40.9 ± 0.1
10	20	-0.0246 ± 0.0009	-28.0 ± 0.2

Table 5.1: Fit results of the resonance shift as a linear relation to the current at 150 K and 10K.

shift between the two implantation energies is consistent with that extrapolated from the top panel of Fig.5.10 shown in Section 5.2.2. Shifts at 10 K (diamonds in Fig. 5.20) are fit to a linear function for negative current and a constant for positive current. The fit results are also shown in Table 5.1.

A simple and quick estimate shows that the current loop, formed due to the arrangement of the lead wires on the sample (Fig. 5.14), should generate a stray field on the order of 0.2 G with 500 mA current, corresponding to a shift of ~ 10 ppm, which linearly scales by the current. This likely explains the linear relation between the small shift and the current.

Fig. 5.21 shows the shift corrected by removing the stray-field effect of the current. After correction, the shifts at 150 K (squares and stars in Fig.
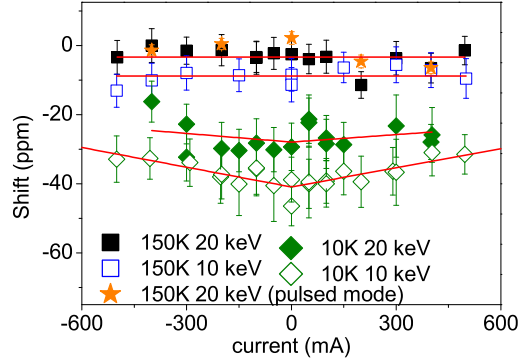
Figure 5.21: The current-dependent shift of ^{8}Li$^+$ resonance (CW mode) corrected for the stray-field effect of the current at 150 K (squares) and 10 K (diamonds) at the implantation energy of 20 keV (solid symbols) and 10 keV (open symbols) at 2.2 T. The stars are measured in pulsed mode at 150 K with 20 keV in 2.2 T.

5.21) are approximately constant at all currents, while at 10 K, the shift (diamonds in Fig. 5.21) increases with current both positively and negatively at approximately the same slope. This indicate contributions from mechanisms other than the stray field of the current. However, the symmetric shift with current is likely another consequence of the local heating effect. Note that the resonance is approximately constant above 150 K, and negatively shifts with temperature below 150 K (the left panel of Fig. 5.17). The injected current locally heats up the sample, resulting in different final local temperatures with the magnitude of the current. At 150 K, the resonance does not shift with current even though the final temperature may be different. At 10 K, the resonance shift is sensitive to the actually local temperature. Heating in combination with the intrinsically increasing shift at 10 K is consistent with the sign of the symmetric current effect.

The resonance width also shows different current dependence at 150 K and 10 K (Fig. 5.20, right panel). The resonance is symmetrically broadened with current injection (both positive and negative) at 150 K, while at 10 K, the injected current narrows the resonance linewidth. If there's any broadening due to the current-induced spin polarization, it may be on the same order as the shift, which is tiny in this case. The different current

dependence of the linewidth could also be attributed to the heating effect of the current.

The resonance width in GaAs changes monotonically with temperature below 150K (Section 3.3.2). Therefore the width itself could be used as an indication of local temperature to measure the heating effect of current at low temperature (below ~ 100 K). Alternatively it might be possible to install another thermometer close to the sample surface where the measurement is actually taken. This would require significant modification of the current sample holder.

5.3.4 Summary

We measured the ^{8}Li$^+$ resonance spectra (CW mode) in Fe/GaAs heterostructures with semi-insulating and heavily n-type GaAs, and with/without injection current. The Schottky barrier formed due to the contact of the ferromagnetic metal with a semiconductor turns out to be an important factor determining the electron tunneling over the barrier and transport in the semiconductor. Any effect of spin injection on the ^{8}Li$^+$ resonance is smaller than that of the stray field effect of the contacts, which is already small. The upper limit of the resonance shift due to spin injection is only ~ 10 ppm at 10 K with 500 mA current compared with zero current.

This negative result is surprising in light of other measurements that have found spin injection in similar Fe/GaAs heterostructures using other methods of detection[76, 77, 78, 80, 83]. One reason the effect may appear so small in our data is that the hyperfine coupling to the conduction electrons in GaAs for interstitial ^{8}Li$^+$ is very small, but this is not likely based on the results in Mn doped GaAs (Chapter 4).

Although the result is negative, we have made significant progress in establishing how to do such measurements and in measuring an upper limit on the effect.

Chapter 6

Summary and Future Work

6.1 Summary

In this work, we have applied β-NMR to study the local magnetic field in three spintronic materials: GaAs crystals, Mn doped GaAs and Fe/GaAs heterostructures. The behavior of ^{8}Li$^+$ probe in GaAs crystals is studied as control experiments, from which we can access the effects of ferromagnetic thin film heterostructures. Both Ga$_{1-x}$Mn$_x$As and Fe/GaAs heterostructures are in the form of thin films epitaxially grown on GaAs substrates. It's generally hard to detect such thin film samples by conventional NMR due to signal limitations. As a local probe, depth-controlled β-NMR provides a depth profile of the magnetic properties at the atomic level in both Ga$_{1-x}$Mn$_x$As and Fe/GaAs heterostructure and broadens our knowledge of the hyperfine interaction of the implanted probe (^{8}Li$^+$) in each host material.

6.1.1 β-NMR Study of GaAs Crystals

The high resolution measurements in the GaAs crystals by pulsed β-NMR provides more information on the magnetic properties of GaAs. We observed a small temperature-, depth- and doping- dependent shift of the resonance. The depth dependence is only observed in the semi-insulating GaAs crystal, which seems related to doping. In the heavily doped n-GaAs with much higher carrier density, the resonance does not shift with implantation energy. The resonance shift below 150 K in both semi-insulating and n-type GaAs, at ~ 100 ppm or less, is on the order of some smaller Knight shifts of ^{8}Li$^+$ in metallic hosts. Moreover, the shift in n-GaAs appears to be somewhat

sample dependent (Section 3.3.2.2 *vs.* 5.2.2). However, it neither behaves like a chemical shift or Knight shift, nor follows Curie's Law. The activated temperature dependence suggests the role of shallow impurities in giving rise to the temperature dependent shift, but there is no obvious mechanism for it, since the carrier density of so low particularly in the semi-insulating GaAs.

The shift is of interest in understanding the behavior of ^{8}Li$^+$ in semiconductors and forms the "baseline" behavior of the substrate for the current injection experiment, from which we can assess additional effects of spin injection.

6.1.2 β-NMR Study of Ga$_{1-x}$Mn$_x$As

Ga$_{1-x}$Mn$_x$As is the β-NMR study on a ferromagnetic material that follows its temperature dependence through ferromagnetic transition, therefore it is an important reference point to compare with other ferromagnets. We find both spin lattice relaxation and resonance signals of ^{8}Li$^+$ in Ga$_{1-x}$Mn$_x$As in the ferromagnetic state. Two resonances are clearly resolved from the nonmagnetic GaAs substrate and the magnetic Ga$_{1-x}$Mn$_x$As film. The latter is negatively shifted compared to the resonance in GaAs and this shift is linearly proportional to the external magnetic field. The substrate signal persists down to implantation energy as low as 5 keV – at this energy most ^{8}Li$^+$ stop in the magnetic Ga$_{1-x}$Mn$_x$As layer. The temperature dependence of the resonance position and the spin relaxation rate in the film is followed through T_C.

It has long been debated whether the delocalized holes in Ga$_{1-x}$Mn$_x$As originate from valence band or impurity band carriers (Section 4.1). β-NMR data may help to elucidate the properties of the itinerant carriers. Based on the temperature dependence of the resonance position in Ga$_{1-x}$Mn$_x$As the hole contribution to the magnetization scales with the macroscopic magnetization through T_C and only deviates below $\sim$40 K. Unexpectedly, the hyperfine coupling constant of ^{8}Li$^+$ in Ga$_{1-x}$Mn$_x$As is found to be negative, which may indicate the Femi level falls into a Mn derived impurity band.

To make this conclusion more firm, one would need to verify that the $^8\text{Li}^+$ hyperfine coupling constant A_{HF} to the valence band holes is of positive sign. One might be able to probe this experimentally by creating optically polarized holes in the valence band of pure GaAs by pumping with circularly polarized light[68, 181, 182]. Alternatively, electronic structure calculation may be able to predict the sigh of A_{HF} reliably (e.g. for $^8\text{Li}^+$ in ZnO[183]). However, calculation of such a low energy property is difficult to carry out convincingly even with the best modern electronic structure codes.

The spin relaxation rate λ is also studied to elucidate the origin of the delocalized holes. As a measure of the spectral density of transverse magnetic fluctuations at the NMR frequency, λ in homogeneous metallic[150] or semiconducting[154] ferromagnets usually peaks at T_{C} when the spin dynamics change dramatically through the formation of a static moment. The amplitude of λ in the magnetic $\text{Ga}_{1-x}\text{Mn}_x\text{As}$ layer is ~ 10 times larger than the rate in metallic Ag[141], but surprisingly shows a relatively weak temperature dependence through T_{C} with only a small enhancement at T_{C}. λ neither peaks at T_{C}, nor follows Korringa's Law, which is anticipated in such metallic alloy. It is, however, similar to what is found in doped non-magnetic semiconductors when the Fermi level lies in a narrow impurity band[155, 156, 157].

Another important problem is the possibility of magnetic phase separation in $\text{Ga}_{1-x}\text{Mn}_x\text{As}$ observed in some μSR measurements[50]. A careful analysis of the resonance spectra in $\text{Ga}_{1-x}\text{Mn}_x\text{As}$ shows a continuous change of amplitude through T_{C}. If the $\text{Ga}_{1-x}\text{Mn}_x\text{As}$ layer were magnetically phase separated, much $^8\text{Li}^+$ would be undetectable once the $\text{Ga}_{1-x}\text{Mn}_x\text{As}$ layer is in the ferromagnetic phase below T_{C} and we would expect to see a sharp and dramatic loss in amplitude in contrast to the results of the measurement. No evidence is found, in this sample, for the magnetic phase separation.

6.1.3 β-NMR Study of Fe/GaAs Heterostructures

Spin injection from the magnetic layer into semiconductor GaAs has been successfully demonstrated by other techniques[76, 83, 184]. The injected

144

spin polarization is generated and detected either optically[184] or electrically[83]. In such heterostructures, spin dynamics is influenced by the contact hyperfine interaction[185]. β-NMR provides a local depth-resolved probe to detect the injected spin polarization.

We have measured the ^{8}Li$^+$ resonance in Fe/GaAs heterostructure with semi-insulating and heavily doped n-type GaAs substrates, with and without injected current. The maximum penetration depth of ^{8}Li$^+$ in GaAs is $\sim$ 140 nm. The heterostructure on the semi-insulating GaAs substrate is unlikely to show spin injection due to the wide Schottky barrier formed at the interface (Section 5.1). With zero current, no effect of thermal equilibrium tunneling in the Fe/nGaAs is found.

In order to conduct current injection from the magnetic Fe layer into the n-GaAs substrate, we designed and setup a new current injection system in the existing β-NMR spectrometer. The system reliably gives electrical contact to the sample in the ultra-high vacuum (UHV) spectrometer without venting. We found effects of local Joule heating and a very small stray magnetic field caused by the injected current. However, we found no convincing evidence of injected spin polarization in either heterostructure for current densities up to $j \approx 2 \times 10^4$ A/m^2.

6.2 Future Work

We have successfully injected current into the sample in the UHV spectrometer. The current injection system has been tested and proven capable of biasing the Fe overlayer with respect to the GaAs. However, to minimize the (already small) stray magnetic field generated by the injection current, it is necessary to redesign the arrangement of the Au contacts and the wiring on the sample. A new design needs to consider the way the sample is connected to the current source and how to cancel the field generated by the leads. The center of the sample is reserved for accepting ^{8}Li$^+$ so that this area should be clear of wires or contacts. A more symmetric geometry is better to minimize the stray field. Since the sample used in β-NMR can not be very small, a large current is required to reach a current density com-

parable to that in reported experiments[76, 83, 184]. The resistive heating is inevitable. How to minimize the resistive heating and the temperature gradient is also a problem requiring serious consideration, *e.g.* to make a better thermal contact to the sample to reduce heating effect. Alternatively a sequence of carefully programmed current pulses could be used instead of the continuous current in order to lower the overall heating effect. To measure the heating effect requires a thermometer on the sample. This could be an actual thermometer very close to the sample surface, but not so close as to be in the beam, or we could use the resonance width in GaAs as a built-in thermometer after careful calibration. We could also make a thicker Au layer (*e.g.* 50 monolayer) to make the current distribution more uniform along the sample.

With a next generation design, the spin injection in FM/SC heterostructures could be further explored. We would then study the temperature, current, and depth dependence of the injected spin polarization. A better understanding of the hyperfine interaction in the heterostructure could be achieved by the local probe ^{8}Li$^+$. The ferromagnetic semiconductor Ga$_{1-x}$Mn$_x$As could be also used in the spin injection as a polarized spin source with the advantage that there's no Schottky-like barrier at the interface. EuO is another candidate spin polarization source with the advantage/disadvantage of T_C= 69 K. This may provide a new point of view on the spin injection from a ferromagnetic source to conventional semiconductors. Spin accumulation was successfully demonstrated in the interface of forwarded biased MnAs/GaAs structure[184]. MnAs, as a ferromagnetic metal with $T_C \approx 320$ K[186], could also be used as a spin source. The Schottky barrier in this case is similar to Fe/GaAs (~ 0.8 V)[184]. For all such structures, one should consider growing a layer of n-GaAs by MBE before depositing the magnetic thin films on commercial GaAs substrates to avoid variability in commercial GaAs wafers.

Another possibility is to produce spin polarization directly in a GaAs crystal by optical pumping with circularly polarized light and use the ^{8}Li$^+$ probe to study the behavior of optically generated spins in GaAs. This would allow an independent measure of the hyperfine coupling of ^{8}Li$^+$ to

the conduction band of GaAs.

There are many unresolved puzzles in $Ga_{1-x}Mn_xAs$ itself. The channeling effect in the $Ga_{1-x}Mn_xAs$/GaAs structure needs detailed exploration. Combined with the β-NMR results, reliable *ab initio* calculations of the hyperfine coupling of $^8Li^+$ to the valence band of GaAs and the Mn derived impurity band may distinguish the appropriate microscopic model for the delocalized carriers. A more complete picture will be obtained from a systematic study of $Ga_{1-x}Mn_xAs$ as a function Mn concentration and film thickness and also from the study on the effects of field and of the optical carrier excitation.

Bibliography

[1] M.A. Ruderman and C. Kittel. *Phys. Rev.*, 96:99, 1954.

[2] T. Kasuya. *Prog. Theor. Phys.*, 16:45, 1956.

[3] K. Yosida. *Phys. Rev.*, 106:893, 1957.

[4] J. Bardeen and W. H. Brattain. *Phys. Rev.*, 74:230, 1948.

[5] M.N. Baibich, J.M. Broto, A. Fert, F.Nguyen Van Dau, F. Petroff, P. Etienne, G. Creuzet, A. Friederich, and J. Chazelas. *Phys. Rev. Lett.*, 61:2472, 1988.

[6] G. Binasch, P. Grünberg, F. Saurenbach, and W. Zinn. *Phys. Rev. B*, 39:4828, 1989.

[7] S. Datta and B. Das. *Appl. Phys. Lett.*, 56:665, 1990.

[8] M.E. Flatté, Z.G. Yu, E. Johnston-Halperin, and D.D. Awschalom. *Appl. Phys. Lett.*, 82:4740, 2003.

[9] S. Sugahara and M. Tanaka. *Appl. Phys. Lett.*, 84:2307, 2004.

[10] J. Fabian, I. Žutić, and S.D. Sarma. *Appl. Phys. Lett.*, 84:85, 2004.

[11] K.C. Hall and M.E. Flatté. *Appl. Phys. Lett.*, 88:162503, 2006.

[12] D.D. Awschalom, D. Loss, and N. Samarth. *Semiconductor Spintronics and Quantum Computation*. Springer, 2002.

[13] R. Hanson, F.M. Mendoza, R.J. Epstein, and D.D. Awschalom. *Phys. Rev. Lett.*, 97:087601, 2006.

[14] I. Žutić. *Rev. Mod. Phys.*, 76:323, 2004.

[15] Neil W. Ashcroft and N. David Mermin. *Solid State Physics*. Thomson Learning Asia Pte Ltd, 1976.

[16] C. Kittel. *Introduction to Solid State Physics*. John Wiley & Sons, 2005.

[17] Robert M. White. *Magnetic Properties of materials*, volume 32 of *Springer Series in Solid-State Sciences*. Spinger, 2007.

[18] B.T. Matthias, R.M. Bozorth, and J.H. Van Vleck. *Phys. Rev. Lett.*, 7:160, 1961.

[19] T.R. McGuire and M.W. Shafer. *J. Appl. Phys.*, 35:984, 1964.

[20] H. Ohno, A. Shen, F. Matsukura, A. Oiwa, A. Endo, S. Katsumoto, and Y. Iye. *Appl. Phys. Lett.*, 69:363, 1996.

[21] L. Chen, X. Yang, F.H. Yang, J.H. Zhao, J. Misuraca, P. Xiong, and S. von Molnar. *Nano Lett.*, 11:2584, 2011.

[22] A.M. Nazmul, T. Amemiya, Y. Shuto, S. Sugahara, and M. Tanaka. *Phys. Rev. Lett.*, 95:017201, 2005.

[23] A.H. MacDonald, P. Schiffer, and N. Samarth. *Nature Materials*, 4:195, 2005.

[24] T. Dietl, H. Ohno, F. Matsukura, J. Cibert, and D. Ferrand. *Science*, 289:1019, 2000.

[25] T. Dietl, H. Ohno, and F. Matsukura. *Phys. Rev. B*, 63:195205, 2001.

[26] J. Blinowski and P. Kacman. *Phys. Rev. B*, 67:121204, 2003.

[27] K.M. Yu, W. Walukiewicz, T. Wojtowicz, J. Denlinger, M.A. Scarpulla, X. Liu, and J.K. Furdyna. *App. Phys. Lett.*, 86:R042102, 2005.

[28] T. Jungwirth, J. Sinova, J. Mašek, J. Kučera, and A.H. MacDonald. *Rev. Mod. Phys.*, 78:809, 2006.

[29] K.M. Yu, W. Walukiewicz, T. Wojtowicz, I. Kuryliszyn, X. Liu, Y. Sasaki, and J.K. Furdyna. *Phys. Rev. B*, 65:201303, 2002.

[30] V. Holý, Z. Matěj, O. Pacherová, V. Novák, M. Cukr, K. Olejník, and T. Jungwirth. *Phys. Rev. B*, 74:245205, 2006.

[31] T. Dietl. *Nature Materials*, 9:965, 2010.

[32] J.M. Tang and M.E. Flatte. *Phys. Rev. Lett.*, 92:047201, 2004.

[33] P. Mahadevan and A. Zunger. *Appl. Phys. Lett.*, 85:2860, 2004.

[34] T. Dietl, A. Haury, and Y.M. d'Aubigne. *Phys. Rev. B*, 55:R3347, 1997.

[35] C. Zener. *Phys. Rev.*, 81:440, 1951.

[36] E.O. Kane and T.S. Moss, editors. *Handbook on Semiconductors*, volume 1. Springer, 1982.

[37] S. Ohya, I. Muneta, P.N. Hai, and M. Tanaka. *Phys. Rev. Lett.*, 104:167204, 2010.

[38] F. Popescu, C. Sen, E. Dagotto, and A. Moreo. *Phys. Rev. B*, 76:085206, 2007.

[39] K. Hirakawa, S. Katsumoto, T. Hayashi, Y. Hashimoto, and Y. Iye. *Phys. Rev. B*, 65:193312, 2002.

[40] V.F. Sapega, M.Moreno, M. Ramsteiner, L. Däweritz, and K.H. Ploog. *Phys. Rev. Lett.*, 95:137401, 2005.

[41] K.S. Burch, D.B. Shrekenhamer, E.J. Singley, J. Stephens, B.L. Sheu, R.K. Kawakami, P. Schiffer, N. Samarth, D.D. Awschalom, , and D.N. Basov. *Phys. Rev. Lett.*, 97:087208, 2006.

[42] K. Ando, H. Saito, K.C. Agarwal, M.C. Debnath, and V. Zayets. *Phys. Rev. Lett.*, 100:067204, 2008.

[43] L.P. Rokhinson, Y. Lyanda-Geller, Z.Ge, S. Shen, X. Liu, M. Dobrowolska, and J.K. Furdyna. *Phys. Rev. B*, 76:161201, 2007.

[44] K. Alber, K.M. Yi, P.R. Stone, O.D. Dubon, W. Walukiewicz, T. Wojtowicz, X. Liu, and J.K. Furdyna. *Phys. Rev. B*, 78:075201, 2008.

[45] A. Richardella, P. Roushan, S. Mack, B. Zhou, D.A. Huse, D.D. Awschalom, and A. Yazdani. *Science*, 327:665, 2010.

[46] M. Dobrowolska, K. Tivakornsasithorn, X.Liu, J.K. Furdyna, M. Berciu, K.M. Yu, and W. Walukiewicz. *Nature Materials*, 11:444, 2012.

[47] D. Neumaier, M. Turek, U. Wurstbauer, A. Vogl, M. Utz, W. Wegscheider, and D. Weiss. *Phys. Rev. Lett.*, 103:087203, 2009.

[48] Y. Nishitani, D. Chiba, M. Endo, M. Sawicki, F. Matsukura, T. Dietl, and H. Ohno. *Phys. Rev. B*, 81:045208, 2010.

[49] S. Ohya, K. Takata, and M. Tanaka. *Nature Physics*, 7:342, 2011.

[50] V.G. Storchak, D.G. Eshchenko, E. Morenzoni, T. Prokscha, A. Suter, X. Liu, and J.K. Furdyna. *Phy. Rev. Lett.*, 101:027202, 2008.

[51] M. Sawicki, D. Chiba, A. Korbecka, Y. Nishitani, J.A. Majewski, F. Matsukura, T. Dietl, and H. Ohno. *Nature Physics*, 6:22, 2010.

[52] S.R. Dunsiger, J.P. Carlo, T. Goko, G. Nieuwenhuys, T. Prokscha, A. Suter, E. Morenzoni, D. Chiba, Y. Nishitani, T. Tanikawa, F. Matsukura, H. Ohno, F. Ohe, S. Maekawa, and Y.J. Uemura. *Nature Materials*, 9:299, 2010.

[53] M.D. Kapetanakis and I.E. Perakis. *Phys. Rev. Lett.*, 101:097201, 2008.

[54] P. Moriya and H. Munekata. *J. Appl. Phys.*, 93:4603, 2003.

[55] Y. Ohno, D.K. Young, B. Beschoten, F. Matsukura, H. Ohno, and D.D. Awschalom. *Nature*, 402:790, 1999.

[56] O. Gunnarsson. *J. Phys. F: Metal Phys.*, 6 (4):587, 1976.

[57] M. Shimizu. *Rep. Prog. Phys.*, 44:1981, 329.

[58] Jürgen Kübler. *Theory of itinerant Electron Magnetism.* Oxford University Press Inc., 2000.

[59] J.R. Waldrop. *J. Vac. Sci. Technol. B*, 2:445, 1984.

[60] R. Fiederling, M. Keim, G. Reuscher, W. Ossau, G. Schmidt, A. Waag, and L. W. Molenkamp. *Nature*, 402:787, 1999.

[61] P.R. Hammar, B.R. Bennett, M.J. Yang, and M. Johnson. *Phys. Rev. Lett.*, 83:203, 1999.

[62] G. Schmidt, D. Ferrand, and L.W. Molenkamp. *Phys. Rev. B*, 62:4790, 2000.

[63] Y.Y. Wang and M.W. Wu. *Phys. Rev. B*, 72:153301, 2005.

[64] J. C. Bruyère, G. Clerc, O. Massenet, R. Montmory, L. Néel, D. Paccard, and A. Yelon. *J. Appl. Phys.*, 36:944, 1965.

[65] J.J. Hauser. *Phys. Rev.*, 187:580, 1969.

[66] P. Grünberg, R. Schreiber, Y. Pang, M.B. Brodsky, and H. Sowers. *Phys. Rev. Lett.*, 57:2442, 1986.

[67] R.K. Kawakami, Y. Kato, M. Hanson, I. Malajovich, J.M. Stephens, E. Johnson-Halperin, G. Salis, A.C. Gossard, and D.D. Awschalom. *Science*, 294:2001, 2001.

[68] F. Meier and B. P. Zakharchenya. *Optical Orientation.* Elsevier Science Ltd., 1984.

[69] J.M. Kikkawa and D.D. Awschalom. *Science*, 287:473, 2000.

[70] G. Salis, D.T. Fuchs, J.M. Kikkawa, D.D. Awschalom, Y. Ohno, and H. Ohno. *Phys. Rev. Lett.*, 86:2677, 2001.

[71] J. Kikkawa and D.D. Awschalom. *Phys. Rev. Lett.*, 80:4313, 1998.

[72] J. Kikkawa and D.D. Awschalom. *Nature*, 397:139, 1999.

[73] R.J. Epstein, I. Malajovich, R.K. Kawakami, Y. Chye, M. Hanson, P.M. Petroff, A.C. Gossard, and D.D. Awschalom. *Phys. Rev. B*, 65:121202, 2002.

[74] S.F. Alvarado and P. Renaud. *Phys. Rev. Lett.*, 68:1387, 1992.

[75] B.T. Jonker, G. Kioseoglou, A.T. Hanbicki, C.H. Li, and P.E. Thompson. *Nature Physics*, 3:542, 2007.

[76] H.J. Zhu, M. Ramsteiner, H. Kostial, M. Wassermeier, H.P. Schönherr, and K.H. Ploog. *Phys. Rev. Lett.*, 87:016601, 2001.

[77] A.T. Hanbicki, B.T. Jonker, G. Itskos, G. Kioseoglou, and A. Petrou. *Appl. Phys. Lett.*, 80:1240, 2002.

[78] V.F. Motsnyi, P. van Dorpe, W. van Roy, E. Goovaerts, V.T. Safarov, G.Borghs, and J. de Boeck. *Phys. Rev. B*, 68:245319, 2003.

[79] S.A. Crooker, M. Furis, X. Lou, C. Adelmann, D.L. Smith, C.J. Palmstrøm, and P.A. Crowell. *Science*, 309:2191, 2005.

[80] X. Lou, C. Adelmann, M. Furis, S.A. Crooker, C.J. Palmstrøm, and P.A. Crowell. *Phys. Rev. Lett.*, 96:176603, 2006.

[81] O.M. van 't Erve, A.T. Hanbicki, M. Holub, C.H. Li, C. Awo-Affouda, P.E. Thompson, and B.T. Jonker. *Appl. Phys. Lett.*, 91:212109, 2007.

[82] M. Ciorga, A. Einwanger, U. Wurstbauer, D. Schuh, W. Wegscheider, and D. Weiss. *Phys. Rev. B*, 79:165321, 2009.

[83] G. Salis, A. Furhrer, and S.F. Alvarado. *Phys. Rev. B*, 80:115332, 2009.

[84] A. Schmehl, V. Vaithyanathan, A. Herrnberger, S. Thiel, C. Richter, M. Liberati, T. Heeg, M. Rockerath, L.F. Kourkoutis, S. Muhlbauer, P. Boni, D.A. Muller, Y. Barash, J. Schubert, Y. Idzerda, J. Mannhart, and D.G. Schlom. *Nature Mater.*, 6:882, 2007.

[85] G. Srajera, L.H. Lewis, S.D. Bader, A.J. Epstein, C.S. Fadley, E.E. Fullerton, A. Hoffmann, J.B. Kortright, Kannan M. Krishnan, S.A. Majetich, T.S. Rahman, C.A. Ross, M.B. Salamon, I.K. Schulle, T.C. Schulthess, and J.Z. Sun. *J. Magn. Magn. Mat.*, 307:1, 2006.

[86] C.D.P. Levy, M.R. Pearson, G.D. Morris, J. Lassen, K.H. Chow, M.D. Hossain, R.F. Kiefl, R. Labbé, W.A. MacFarlane, T.J. Parolin, L. Root, H. Saadaoui, M. Smadella, and D. Wang. *Physica B*, 404:1010, 2009.

[87] J. Govaerts, M. Kokkoris, and J. Deutsch. *J. Phys. G: Nul. Part. Phys.*, 21:1675, 1995.

[88] The ISAC β NMR HomePage. Optical polarization for β-nmr at isac.

[89] The ISAC β NMR HomePage. The high and low field spectrometers.

[90] The ISAC β NMR HomePage. Beamline optics and deceleration.

[91] J.F. Ziegler. *http://www.srim.org/SRIM/SRIM 08.pdf.*

[92] W. Eckstein. *Computer Simulation of Ion-Solid Interactions.* Springer, 1991.

[93] T.J. Jackson, T.M. Riseman, E.M. Forgan, H. Glückler, T. Prokscha, E. Morenzoni, M. Pleines, Ch. Niedermayer, G. Schatz, H. Luetkens, and J. Litterst. *Phys. Rev. Lett.*, 84:4958, 2000.

[94] M. Kokkoris, G. Perdikakis, R. Vlastou, C.T. Papadopoulos, X.A. Aslanoglou, M. Posselt, R. Grötzschel, S. Harissopulos, and S. Kossionides. *Nucl. Instrum. Methods in Phys. Research B*, 201:623, 2003.

[95] C.J. Andreen and R.L. Hines. *Phys. Rev.*, 159:285, 1967.

[96] H. Saadaoui. *Magnetic Properties Near the Surface of Cuparate Super-conductors Studied Using Beta-Detected NMR*. PhD thesis, University of British Columbia, 2009.

[97] C.D.P. Levy, A. Hatakeyama, Y. Hirayama, R.F. Kiefl, R. Baartman, J.A. Behr, H. Izumi, D. Melconian, G.D. Morris, R. Nussbaumer, M. Olivo, M. Pearson, R. Poutissou, and G.W. Wight. *Nucl. Instrum. Methods in Phys. Research B*, 204:689, 2003.

[98] W.A. MacFarlane, G.D. Morris, K.H. Chow, R.A. Baartman, S. Daviel, S.R. Dunsiger, A. Hatakeyama, S.R. Krietzman, C.D.P. Levy, R.I. Miller, K.M. Nichol, R. Poutissou, E. Dumont, L.H. Greene, and R.F. Kiefl. *Physica B*, 326:209, 2003.

[99] C.P. Slichter. *Principles of Magnetic Resonance*. Springer, 1990.

[100] D. Borremans, D.L. Balabanski, K. Blaum, W. Geithner, S. Gheysen, P. Himpe, M. Kowalska, J. Lassen, P. Lievens, S. Mallion, R. Neugart, G. Neyens, N. Vermeulen, and D. Yordanov. *Phys. Rev. C*, 72:044309, 2005.

[101] M. Garwood and L. DelaBarre. *J. of Mag. Res.*, 153:1577, 2001.

[102] Z. Salman, R.F. Kiefl, K.H. Chow, M.D. Hossain, T.A. Keeler, S.R. Kreitzman, C.D.P. Levy, R.I. Miller, T.J. Parolin, M.R. Pearson, H. Saadaoui, J.D. Schultz, M. Smadella, D. Wang, and W.A. MacFarlane. *Phys. Rev. Lett.*, 96:147601, 2006.

[103] C.S. Fuller and K.B. Wolestirn. *J. Appl. Phys.*, 33:2057, 1962.

[104] K.H. Chow, Z. Salman, W.A. MacFarlane, B. Campbell, T.A. Keeler, R.F. Kiefl, S.R. Kreitzman, C.D.P. Levy, G.D. Morris, T.J. Parolin, S. Daviel, and Z. Yamani. *Physica B*, 374.

[105] A. Ney, G. Jan, and S. S. P. Parkin. *J. Appl. Phys.*, 99:043902, 2006.

[106] K. H. Chow, Z. Salman, R.F. Kiefl, W.A. MacFarlane, C.D.P. Levy, P. Amaudruz, R. Baartman, J. Chakhalian, S. Daviel, Y. Hirayama,

A. Hatakeyama, D.J. Arseneau, B. Hitti, S.R. Kreitzman, G.D. Morris, R. Poutissou, and E. Reynard. *Physica B*, 340-341:1151, 2003.

[107] B. Ittermann, M. Fullgrabe, M. Heemeier, F. Kroll, F. Mai, K. Marbach, P. Meier, D. Peters, G. Welker, W. Geithner, S. Kappertz, S. Wilbert, R. Neugart, P. Lievens, U. Georg, M. Keim, and the ISOLDE Collaboration. *Hyp. Int.*, 129:423, 2000.

[108] G. Lindner, S. Winter, H. Hofsäss, S. Jahn, S. Blässer, E. Recknagel, and G. Weyer. *Phys. Rev. Lett.*, 63:179, 1989.

[109] U. Wahl. *Phys. Rep.*, 280:145, 1997.

[110] K.W. Kehr, D. Richter, and J.-M. Welter. *Phys. Rev. B*, 26:567, 1982.

[111] R.C. Vil ao, J.M. Gil, H.V. Alberto, J. Piroto Duarte, N. Ayres de Campos, A. Weidinger, M.V. Yakushev, and S.F.J. Cox. *Physica B*, 326:181, 2003.

[112] M. Wilkening, D. Bork, S. Indris, and P. Heitjans. *Phys. Chem. Chem. Phys.*, 4:3246, 2002.

[113] C. Wang and Q.M. Zhang. *Phys. Rev. B*, 70:35201, 2004.

[114] B. Ittermann, G. Welker, F. Kroll, F. Mai, K. Marbach, and D. Peters. *Phys. Rev. B*, 59:2700, 1999.

[115] M. Xu, M.D. Hossain, H. Saadaoui, T.J. Parolin, K.H. Chow, T.A. Keeler, R.F. Kiefl, G.D. Morris, Z. Salman, Q. Song, D. Wang, and W.A. MacFarlane. *J. Magn. Res.*, 191:47, 2008.

[116] T.J. Parolin, Z.Salman, K.H. Chow, Q. Song, J. Valiani, H. Saadaoui, A. OHalloran, M.D. Hossain, T.A. Keeler, R.F. Kiefl, S.R. Kreitzman, C.D.P. Levy, R.I. Miller, G.D. Morris, M.R. Pearson, M. Smadella, D. Wang, M. Xu, , and W.A. MacFarlane. *Phys. Rev. B*, 77:214107, 2008.

[117] W. Mönch. *Semiconductor Surfaces and Interfaces*. Springer, 2001.

[118] S. Makram-Ebeid and M. Lannoo. *Phys. Rev. B*, 25:6406, 1982.

[119] H.J. von Bardeleben, D. Stiévenard, D. Deresmes, A. Huber, and J.C. Bourgoin. *Phys. Rev. B*, 34:7192, 1986.

[120] T.S. Wang, K.I. Lin, H.C. Lin, M.H. Lee, Y.T. Lu, and J.S. Hwang. *Physica E*, 40:1975, 2008.

[121] A. Hudgens, M. Kastner, and H. Fritzsch. *Phys. Rev. Lett.*

[122] D.G. Andriano, Y.B. Muravlev, N.N. Solovev, and V.I. Fistul. *Sov. Phys. Semicond.*, 8:386, 1974.

[123] W.D. Hoffmann, D. Michel, I.G. Sorina, and E.V. Charnaya. *Phys. Solid State*, 40:1288, 1998.

[124] A.G. Milnes. *Deep Impurities in Semiconductors*. John Wiley and Sons, N.Y., 1973.

[125] J.G. Braden, J.S. Parker, P. Xiong, S.H. Chun, and N. Samarth. *Phys. Rev. Lett.*, 91:056602, 2003.

[126] K.S. Burch, D.D. Awschalom, and D.N. Basov. *J. Mag. Mag. Mater.*, 320:3207, 2008.

[127] G. Acbas, M.-H. Kim, M. Cukr, V. Novak, M.A. Scarpulla, O.D. Dubon, T. Jungwirth, J. Sinova, and J. Cerne. *Phys. Rev. Lett.*, 103:137201, 2009.

[128] Y. Nojiri, K. Ishiga, T. Onishi, M. Sasaki, F. Ohsumi, T. Kawa, M. Mihara, M. Fukuda, K. Matsuta, , and T. Minamisono. *Hyp. Interact.*, 121:415, 1999.

[129] K. Matsuta, M. Sasaki, T. Tsubota, S. Kaminaka, K. Hashimoto, S. Kudo, M. Ogura, K. Arimura, M. Mihara, M. Fukuda, H. Akai, and T. Minamisono. *Hyperfine Interact.*, 136:379, 2001.

[130] L.D. Landau and E.M. Lifshitz. *Statistical Physics Part 1.* Reed Education and Professional Publishing Ltd, 3 edition, 1980.

[131] R.M. Bozorth. *Ferromagnetism.* D. van Nostrand Company, Inc., 1951.

[132] A.S. Arrott. *J. Magn. Magn. Mat.*, 322:1047, 2010.

[133] S. Yu Dan'kov and A.M. Tishin. *Phys. Rev. B*, 57:3478, 1998.

[134] J. F. Ziegler, J. P. Biersack, and U. Littmark. *The stopping and Range of Ions in Matter.* Pergamon Press: New York, first edition, 1985.

[135] E. Morenzoni, H. Glucker, T. Prokscha, R. Khasanov, H. Luetkens, M. Birke, E.M. Forgan, C. Niedermayer, and M. Pleines. *Nucl. Instrum. Methods in Phys. Research B*, 192:254, 2002.

[136] T.R. Beals, R.F. Kiefl, W.A. MacFarlane, K.M. Nichol, G.D. Morris, C.D.P. Levy, S.R. Kreitzman, R. Poutissou, S. Daviel, R.A. Baartman, and K.H. Chow. *Physica B*, 326:205, 2003.

[137] E.H.C.P. Sinnecker, G.M. Penello, T.G. Rappoport, M.M. SantAnna, D.E. R. Souza, M.P. Pires, J.K. Furdyna, and X. Liu. *Phys. Rev. B*, 81:245203, 2010.

[138] Q. Song, K.H. Chow, R.I. Miller, I. Fan, M.D. Hossain, R.F. Kiefl, S.R. Kreitzman, C.D.P. Levy, T.J. Parolin, M.R. Pearson, Z. Salman, H. Saadaoui, M. Smadella, D. Wang, K.M. Yu, J.K. Furdyna, and W.A. MacFarlane. *Phys. Proc.*, 30:174, 2012.

[139] T.J. Parolin, Z. Salman, J. Chakhalian, Q. Song, K. H. Chow, M.D. Hossain, T.A. Keeler, R.F. Kiefl, S.R. Kreitzman, C.D.P. Levy, R.I. Miller, G.D. Morris, M.R. Pearson, H. Saadaoui, D. Wang, and W.A. MacFarlane. *Phys. Rev. Lett.*, 98:R047601, 2007.

[140] I. Fan, K.H. Chow, T.J. Parolin, M. Egilmez, M.D. Hossain, J. Jung, T.A. Keeler, R.F. Kiefl, S.R. Kreitzman, C.D.P. Levy, R. Ma, G.D. Morris, M.R. Pearson, H. Saadaoui, Z. Salman, M. Smadella, Q. Song, D. Wang, M. Xu, and W.A. MacFarlane. *Physica B*, 404:906, 2009.

[141] M.D. Hossain, H. Saadaoui, T.J. Parolin, Q. Song, D. Wang, M. Smadella, K.H. Chow, M. Egilmez, I. Fan, R.F. Kiefl, S.R. Kreitzman, C.D.P. Levy, G.D. Morris, M.R. Pearson, Z. Salman, and W.A. MacFarlane. *Physica B*, 404:914, 2009.

[142] J.A. Davies and P. Jespersgard. *Can. J. Phys.*, 44:1631, 1966.

[143] J.F. Ziegler, M.D. Ziegler, and J.P. Biersack. *Nucl. Instrum. Methods in Phys. Research B.*

[144] Q. Song, K.H. Chow, R.I. Miller, I. Fan, M.D. Hossain, R.F. Kiefl, S.R. Kreitzman, C.D.P. Levy, T.J. Parolin, M.R. Pearson, Z. Salman, H. Saadaoui, M. Smadella, D. Wang, K.M. Yu, J.K. Furdyna, and W.A. MacFarlane. *Physica B*, 404:892, 2009.

[145] T.J. Parolin, J. Shi, Z. Salman, K.H. Chow, P. Dosanjh, H. Saadaoui, Q. Song, M.D. Hossain, R.F. Kiefl, C.D.P. Levy, M.R.Pearson, and W.A. MacFarlane. *Phys. Rev. B*, 80:R174109, 2009.

[146] R.E. Walstedt and L.R. Walker. *Phys. Rev. B*, 9:4857, 1974.

[147] M.H. Julien, A. Campana, A. Rigamonti, P. Carretta, F. Borsa, P. Kuhns, A.P. Reyes, W.G. Moulton, M. Horvatić, C. Berthier, A. Vietkin, and A. Revcolevschi. *Phys. Rev. B*, 63:R144508, 2001.

[148] R.I. Miller, D. Arseneau, K.H. Chow, S. Daviel, A. Engelbertz, M.D. Hossain, T. Keeler, R.F. Kiefl, S. Kreitzman, C.D.P. Levy, P. Morales, G.D. Morris, W.A. MacFarlane, T.J. Parolin, R. Poutissou, H. Saadaoui, Z. Salman, D. Wang, and J.Y.T. Wei. *Physica B*, 374:30, 2006.

[149] K.H. Chow *et al.* . *the 150 G $T_1(T)$ measurement in pure GaAs*, page unpublished.

[150] M. Shaham, J. Barak, U. El-Hanany, and W.W. Warren Jr. *Phys. Rev. B*, 22:R5400, 1980.

[151] R.S. Title. *J. Appl. Phys.*, 40:4902, 1969.

[152] A. Yaouanc and J. Chappert. *Hyperfine Interact.*, 8:667, 1981.

[153] M. Hampele, D. Herlach, A. Kratzer, G. Majer, J. Major, H.-P. Paich, R. Roth, C.A. Scott, A. Seeger, W. Templ, M. Blanz, S.F.J. Cox, and K. F`urderer. *Hyperfine Interact.*, 65:1081, 1990.

[154] A. Comment, J.P. Ansermet, C.P. Slichter, H. Rho, C.S. Snow, and S.L. Cooper. *Phys. Rev. B*, 72:R014428, 2005.

[155] S.E. Fuller, E.M. Meintjes, and W.W. Warren Jr. *Phys. Rev. Lett.*, 76:R2806, 1996.

[156] E.M. Meintjes, J. Danielson, and W.W. Warren Jr. *Phys. Rev. B*, 71:R035114, 2005.

[157] M.J.R. Hoch and D.F. Holcomb. *Phys. Rev. B*, 71:035115, 2005.

[158] I. Kuryliszyn, T. Wojtowicz, X. Lin, J.K. Furdyna, W. Dobrowolsky, J.M. Broto, O. Portugall, H. Rakota, and B. Raquet. *Acta Phys. Polon.*, 102:649, 2002.

[159] A. Abragam. *Principles of Nuclear Magnetism.* Clarendon Press, Oxford, 1961.

[160] T. Jungwirth, J. Mǎsek, K.Y. Wang, K.W. Edmonds, M. Sawicki, M. Polini, J. Sinova, A.H. MacDonald, R.P. Campion, L.X. Zhao, N.R.S. Farley, T.K. Johal, G.van der Laan, C.T. Foxon, and B.L. Gallagher. *Phys. Rev. B*, 73:R165205, 2006.

[161] G.D. Morris, W.A. MacFarlane, K.H. Chow, Z. Salman, D.J. Arseneau, S. Daviel, A. Hatakeyama, S.R. Kreitzman, C.D.P. Levy, R. Poutissou, R.H. Heffner, J.E. Elenewski, L.H. Greene, and R.F. Kiefl. *Phys. Rev. Lett.*, 93:R157601, 2004.

[162] T.J. Parolin, Z. Salman, K.H. Chow, Q. Song, J. Valiani, H. Saadaoui, A. O'Halloran, M.D. Hossain, T.A. Keeler, R.F. Kiefl, S.R. Kreitzman, C.D.P. Levy, R.I. Miller, G.D. Morris, M.R. Pearson, M. Smadella,

D. Wang, M. Xu, and W.A. MacFarlane. *Phys. Rev. B*, 77:R214107, 2008.

[163] S.D. Mahanti and T.P. Das. *Phys. Rev. B*, 3:R1599, 1971.

[164] K.Terakura and J. Kanamori. *J. Phys. Soc. Jpn.*, 34:1520, 1973.

[165] H. Akai, M. Akai, S. Blugel, B. Drittler, H. Ebert, K. Terakura, R. Zeller, and P.H. Dederichs. *Prog. Theor. Phys. Suppl.*, 101:11, 1990.

[166] H. Alloul and P. Bernier. *Ann. Phys. (Paris)*, 8:169, 1974.

[167] B.J. Kirby, J.A. Borchers, J.J. Rhyne, K.V. O'Donovan, S.G.E. te Velthuis, S. Roy, Cecilia Sanchez-Hanke, T. Wojtowicz, X. Liu, W.L. Lim, M. Dobrowolska, and J.K. Furdyna. *Phys. Rev. B*, 74:245304, 2006.

[168] G. Wastlbauer and J.A.C. Bland. *Adv. in Phys.*, 54:137, 2005.

[169] B. Kardasz and B. Heinrich. *Phys. Rev. B*, 81:094409, 2010.

[170] B. Kardasz, J. Zukrowski, O. Mosendz, M. Przybylski, B. Heinrich, and J. Kirschner. *J. of Appl. Phys.*, 101:09.

[171] A. Ionescu, M. Tselepi, D.M. Gillingham, G. Wastlbauer, S.J. Steinmueller, H.E. Beere, D.A. Ritchie, and J.A.C. Bland. *Phys. Rev. B*, 72:125404, 2005.

[172] B.L. Sharma. *Metal-Semiconductor Schottky Barrier Junctions and Their Applications*. Plenum Press, 1984.

[173] F.A. Padovani and R. Stratton. *Solid State Electronics*, 9:695, 1966.

[174] J.D. Albrecht and D.L. Smiths. *Phys. Rev. B.*, 66:113303, 2003.

[175] W.F. Brinkman, R.C. Dynes, and J.M. Rowell. *J. Appl. Phys.*, 41:1915, 1970.

[176] W.A. Harrison. *Phys. Rev.*, 123:85, 1961.

[177] R.I. Dzhioev, K.V. Korenev, M.V. Lazarev, B.Ya. Meltser, M.N. Stepanova, B.P. Zakharchenya, D. Gammon, and D.S. Karzer. *Phys. Rev. B*, 66:245204, 2002.

[178] A.V. Kimel, F. Bentivegna, V.N. Gridnev, V.V. Pavlov, R.V. Pisarev, and T. Rasing. *Phys. Rev. B*, 63:235201, 2001.

[179] B. Kardasz, O. Mosendz, B. Heinrich, M. Przybylski, and J. Kirschner. *J. of Phys.:Conference Series*, 200:072046, 2010.

[180] T.A. Keeler, Z. Salman, K.H. Chow, B.Heinrich, M.D. Hossian, B. Kardasz, R.F. Kiefl, S.R. Kreitzman, C.D. P. Levy, W.A. MacFarlane, O. Mosendz, T.J. Parolin, M.R. Pearson, and D. Wang. *Phys. Rev. B*, 77:144429, 2008.

[181] Marcus Eickhoff, Stefanie Fustmann, and Dieter Suter. *Phys. Rev. B.*

[182] Kannan Ramaswamy, Stacy Mui, and Sophia E. Hayes. *Phys. Rev. B.*

[183] H. Kwak, M.L. Tiago, T.L. Chan, and J.R. Chelikowsky. *Chem. Phys. Lett.*

[184] J. Stephens, J. Berezovsky, J.P. McGuire, L.J. Sham, A.C. Gossard, and D.D. Awschalom. *Phys. Rev. Lett.*, 93:097602, 2004.

[185] G. Salis, A. Furhrer, and S.F. Alvarado. *Phys. Rev. B*, 81:205323, 2010.

[186] C.P. Bean and D.S. Rodbell. *Phys. Rev.*

[187] MPMS Application Note 1014-822. Verifying the absolute sensitivity in the mpms.

[188] MPMS Application Note 1014-202. Transverse detection system.

[189] MPMS Application Note 1014-213. Subtracting the sample holder background from dilute samples.

[190] MPMS Application Note 1014-819. Connecting a straw adapter to the standard transport rod.

[191] Quantum Design. *MPMS HP-150 OPERATING SYSTEM SOFT-WARE MANUAL.*

[192] Quantum Design. *MPMS Application Notes/Technical Advisories.*

[193] Ralph E. Williams. *Gallium Arsenide Processing Techniques.* Artech House, Inc.

Appendix A

List of Samples

A.1 $Ga_{1-x}Mn_xAs$

The $Ga_{1-x}Mn_xAs$ sample used in β-NMR experiment presented in Chapter 4 is shown in Fig. A.1. The sample is epitaxially grown by X. Liu and J.K. Furdyna in University of Norte Dame. The equilibrium solubility of Mn in GaAs is low ($\sim 10^{19}$ cm^{-3} at most). Therefore low temperature MBE growth was used to realize non-equilibrium growth, so that a larger amount of Mn atoms can be incorporated into the GaAs host. They used a semi-insulating (SI) GaAs as the substrate. First a GaAs buffer layer of ~ 400 nm was grown on the SI GaAs substrate at $T_{substrate} = 590°$C. Then a thin layer of GaAs (~ 2 nm) deposited at low temperature ($T_{substrate} = 275°$C). The 180 nm $Ga_{1-x}Mn_xAs$ film was epitaxially grown on top of the GaAs layers at low temperature ($T_{substrate} = 275°$C) with a slow rate ~ 0.76 MonoLayer (ML) per second. The sample was annealed after growth at 280°C for $\sim$ one hour. The transition temperature T_{C} after annealing is 72 K. The concentration of Mn is estimated from lattice constant of $Ga_{1-x}Mn_xAs$ measured by x-ray diffraction (XRD). The $Ga_{1-x}Mn_xAs$ sample was mounted on a sapphire plate when measured in the β-NMR spectrometer.

A.2   GaAs Crystals and Fe/n-GaAs Heterostructures

There samples were provided by B. Kardasz in the group of B. Heinrich at Simon Fraser University (SFU).

    The GaAs crystals presented in Chapter 3 are shown in Fig. A.2. The

Figure A.1: 180 nm $Ga_{1-x}Mn_xAs$ on semi-insulating GaAs mounted on an 8 mm by 10 mm sapphire plate.

semi-insulating(SI) GaAs crystal (09-B1) and the substrate of the sample Fe/SI-GaAs (09-A1) were cut from the same SI-GaAs wafer. The heavily doped n-type GaAs (09-B2) is provided by AXT, and was measured in β-NMR spectrometer to compare with SI-GaAs (09-A1).

Fig. A.3 shows the sample of Fe/semi-insulating GaAs (09-A1) Fe/n-GaAs (10-A1). The MBE growth of Fe on GaAs is reviewed in Section 5.1.1. β-NMR studies under zero bias is discussed in Section 5.2. The Fe/n-GaAs substrate (10-B1) (Fig. A.4) was measured as control experiment (See Section 5.2.2).

The sample Fe/n-GaAs (11-A1) used in the current-injection experiment is shown in Fig. A.5 left panel, and its substrate (11-B1) is shown in the right panel of Fig. A.5. Fe/n-GaAs (11-A1) was epitaxially grown in the same way as the sample Fe/n-GaAs (10-A1). Further sample preparation for the current injection experiment is detailed in Appendix C. We also measured its I-V characteristic, see discussions in Section 5.1.3.

Figure A.2: Top: 09-B1: Semi-insulating GaAs used as the substrate of Fe/SI-GaAs 09-A1. Bottom: 09-B2: heavily n-type GaAs.
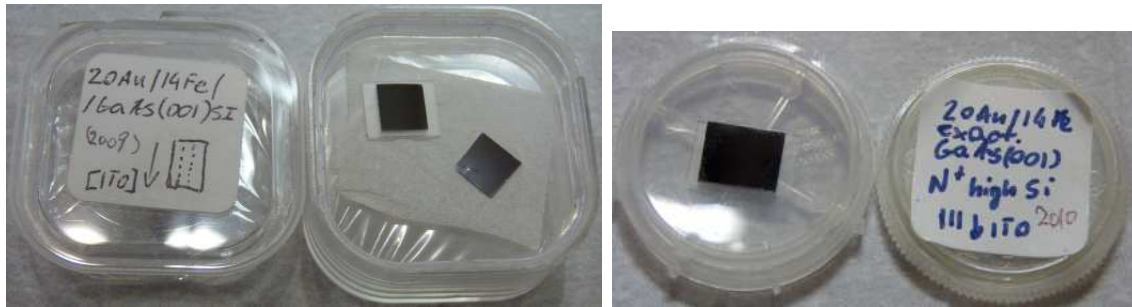

Figure A.3: Fe/GaAs samples used in β-NMR with zero bias. Left: Sample 09-A1: 20 Ml Au/14ML Fe/semi-insulating GaAs. Right: 10-A1: 20 ML Au/14ML Fe/heavily n-type GaAs.

Figure A.4: 10-B1: heavily Si doped n-type GaAs from Wafer Tech used as the substrate of 10-A1.
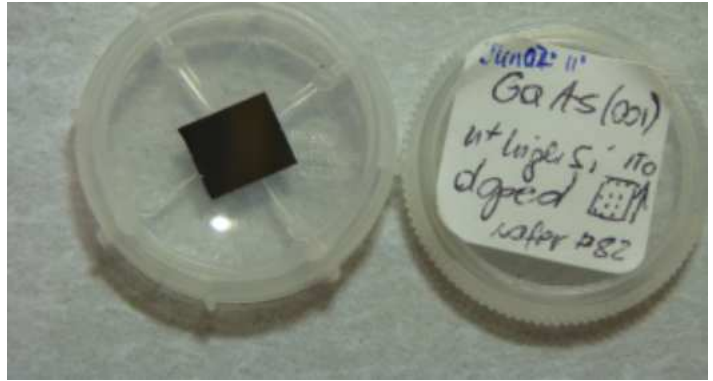

Figure A.5: Left: 11-A1: 20 Ml Au/14ML Fe/heavily n-type GaAs made in exactly the same way as 10-A1. It was used in the β-NMR current-injection experiment. Right: 11-B1: heavily Si doped n-type GaAs from Wafer Tech, from the same batch as 10-B1, and used as the substrate of 11-A1.

Appendix B

SQUID Measurements on Ga$_{1-x}$Mn$_x$As

B.1   SQUID at AMPEL and Sample Descriptions

β-NMR probes a material's magnetic properties which are closely related
to the magnetic susceptibility (as a function of temperature and magnetic
field). Therefore the temperature dependence of the overall "bulk" suscep-
tibility measured independently is of great importance in the analysis and
understanding of β-NMR experimental results. In such a measurement, the
entire sample with all its various components (such as the sample holder
and the substrate of a thin film) contributes to the signal. In contrast, for
a local probe like β-NMR the signal is usually strongly coupled only to a
subset of these components.

The Superconducting Quantum Interference Device (SQUID) is a very
sensitive magnetometer, providing a good measure of the sample magnetic
moment, down to quite small values. It does, however, have a sensitivity
limit. At low field, the magnetic moments can be routinely measured down
to the range of 10^{-7} emu, while the resolution is 10^{-6} emu at high field[187].
Using special care and procedures, it is possible to extend this minimum
down to the range of 10^{-8} emu.

The device we used in AMPEL is the Magnetic Property Measurement
System (MPMS) from Quantum Design. The temperature can be set to
the resolution of 0.01 K, and the field of the instrument's vertical solenoid
varies by only 0.19% within a 4 cm scan length. The device is an "extraction
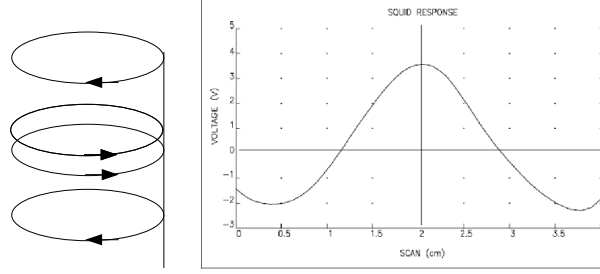SQUID", meaning that the sample is physically scanned with a stepper mo-

Figure B.1: Left: the diagram of the pick up coil to measure the longitudinal moment. Right: SQUID response.

tor in the vertical direction through a pickup coil (Fig. B.1 left panel)[188]) (centered in the high field solenoid) that is coupled to the SQUID itself. The SQUID response is then proportional to the magnetic moment within the pickup coil. Let the (vertical) scan direction be z. An ideal sample will have zero extent in z, and the scan will move the sample from well out of the pickup coil (below) to well out on the upper side. The resulting SQUID voltage (as a function of scan position) has a maximum when the sample is exactly in the coil surrounded by two symmetric (negative) minima (Fig. B.1 right panel)[188]). This characteristic signal may be inverted if the material is diamagnetic and represents the response for an ideal measurement where only the sample is moved. In reality the sample has some finite extent in the z direction, but more importantly for the samples under consideration here, the sample is held in a sample holder which itself may produce a response comparable to the sample itself. Subtracting a sample holder signal is possible during[189] or after the measurement.

For a thin film sample, the overall signal is proportional to the net magnetic moment m^{mag},

$$m^{mag} = m_{\text{film}}^{mag} + m_{\text{substrate}}^{mag} + m_{\text{holder}}^{mag} \tag{B.1}$$

At high fields, any material will have some magnetic response (even quartz or plastic, for example), i.e. the susceptibility χ is never exactly zero, and material surfaces may have additional magnetic response from either dirt or different surface structure and chemistry. The magnetic moments of the

various components all scale with mass and magnetic field, and because of mass differences, the last two terms in Eqn. B.1 may even dominate in the case of a thin film.

The ideal sample holder for an extraction SQUID is completely uniform along the z direction, light weight and made of a material that is minimally magnetic. Often a colourless plastic drinking straw is used for these reasons[190]. Such a holder would at most contribute a small (due to low mass and small χ) constant (independent of scan position z, due to uniformity) offset signal that would not interfere with the W-shaped signal from the sample. In this case, one could have m^{mag}_{holder} making a negligible contribution to m^{mag}.

In the experiments described here, we used 3 sample holders. The sample holder consists of one quartz tube and 2 quartz rods which can just slide inside the tube (Fig. B.2 left panel). It was found that the holder without the sample yielded a signal comparable to that with the sample above T_{C} in the paramagnetic state at 1.3 T. The holder signal is probably due to the ends of the two solid quartz rods (pistons) which are just adjacent to the sample. If this is the case, one can, to a first approximation, simply subtract an independently measured m^{mag}_{holder} to remove it. This assumes that the holder signal has the same shape in the squid response, i.e. that of an ideal zero-z-extent W-shaped signal, as would be the case if the holder signal is from the rod ends.

Another concern about the reproducibility and sensitivity of the measurement is magnet drift. Usually the MPMS magnet is operated in "no-overshoot mode" where the desired magnet current is approached monotonically from the initial magnet current without overshooting the final value. To the zeroth order, the current in the closed superconducting circuit is persistent (i.e. does not decay over time). However, the magnetic field can still drift as some trapped flux may leak out slowly. It's also possible to operate the MPMS in oscillating mode which means the final field is achieved through a series of decreasing amplitude oscillations. This effectively forces the magnet to relax during the charging operation by cycling it through a series of smaller and smaller hysteresis loops. One can also *check* for magnet
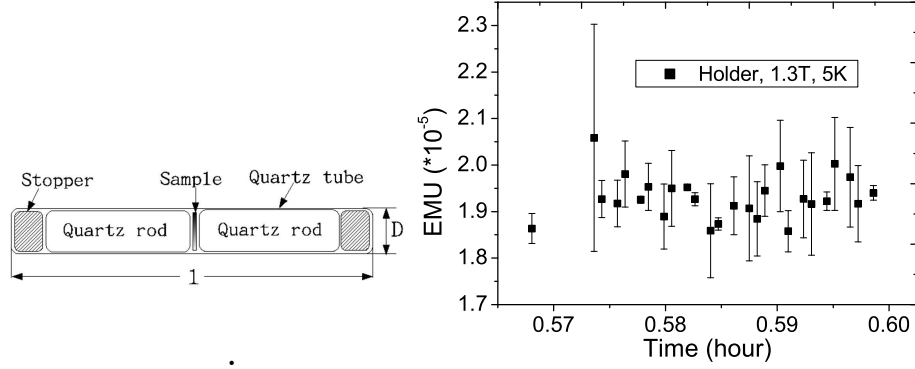
Figure B.2: Left: the diagram of the holder. Right: magnet drift: An empty holder is placed into the magnetic field of 1.3 T. Within the experiment period (45 minutes), there was no obvious drift of the small signal (not shown). Therefore we can conclude that magnet drift does not make a significant contribution to our measurement.

drift, by measuring the signal at a fixed temperature and field over time. In such a measurement, there's no sign of magnet drift at 1.3 T during the test time(Fig. B.2 right panel). For more details of the device and the operation instructions, please refer to Ref. [191, 192].

B.2   Samples

The sample (series number 11127a) is 180 nm thick $Ga_{1-x}Mn_xAs$ epitaxially grown on a layer of ~ 100 nm GaAs grown by MBE on semi-insulating (SI) (100) GaAs substrate and was annealed at 280 ^oC for 1 hour. The SQUID measurement done by the provider is summarized in Fig. B.3 to show the effect of annealing. Its growth and characterization can be found in Section 4.2.

Since we need a better measure of the bulk uniform susceptibility $\chi(q = 0, \omega = 0)$ for the correct interpretation of the β-NMR experimental results, we did a series of tests on the same sample Roger used. We polished the back side of the sample (Fig. B.4) to get rid of the Indium layer, broke it into 3 small pieces and later broke the largest piece into 2. The description
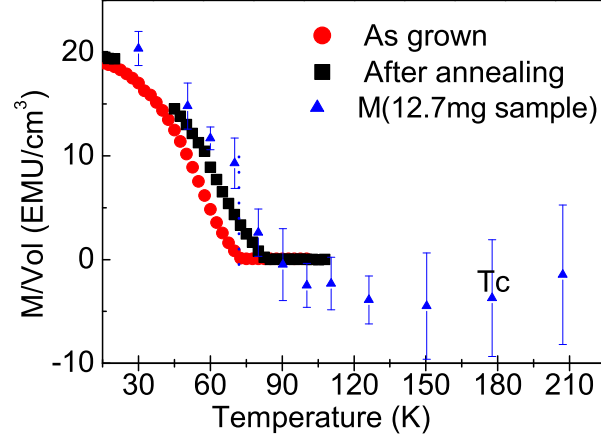
Figure B.3: The SQUID measurement done by the grower before and after annealing at the field of 10 G.

Sample	#1	#2	#3	#4
mass (mg)	37.3±0.1	2.3±0.1	7.7±0.1	12.7±0.1
thickness (mm)	0.41	0.41	0.41	0.41
area (mm×mm)	4.05×4.42	0.84×1.40	2.76×1.42	2.91×2.07
m_{GaAs}^{mag} of the same mass in 1.3 T ($\times 10^{-5}$ emu)	-11.16	-0.688	-2.3	-3.8
Estimated m_{Mn}^{mag} ($\times 10^{-5}$ emu)	19.97	1.18	3.93	6.05

Table B.1: Samples used in the SQUID measurements

Figure B.4: Left: Back side of $Ga_{1-x}Mn_xAs$ sample before polishing. There is some In (silvery) dots on the rough surface. Middle: Sample backside after sanded on a piece of rough paper. Not much of In is removed. There are still some silvery parts. Right: Sample backside after sanding with 6000 sanding paper. No shiny dots are observable and the surface is smoother.

of the resulting samples can be found in Table B.2.

B.3   Summary of SQUID Measurements

The $Ga_{1-x}Mn_xAs$ thin film is ferromagnetic below T_C while it exhibits paramagnetism at higher temperature. The pure GaAs substrate is diamagnetic with a room temperature susceptibility χ of -3.33×10^{-5} cm^3/mole[121], and is very weakly temperature dependent.[1] The magnetic moment contributed by the pure GaAs substrate in 1.3 T can be estimated (taking the largest sample (37.3 mg) as an example) by:

$$
\begin{aligned}
m_{GaAs}^{mag} &= n_{mol}\chi_{mol}H \qquad\qquad\qquad\qquad\qquad\qquad (B.2)\\
&= \frac{\chi_{mol}}{Mass_{mol}} \times H \times m\\
&= \frac{-3.33 \times 10^{-5}\ \ \text{cm}^3/\text{mol}}{144.64\ \ \text{g/mol}} \times 13000\ \ \text{G} \times 0.037\ \ \text{g}\\
&= -1.116 \times 10^{-4}\ \ \text{emu}.
\end{aligned}
$$

We can also estimate the saturated magnetic moment of Mn, m_{Mn}^{mag} in each sample. Assume that every Mn atom contributes 5 μ_B in 1.3 T. m_{Mn}^{mag} (an

---

[1] The variation of χ with temperature $\frac{\partial \chi}{\partial T}$ is 1.2×10^{-7} cm^3/(mol*K), and the experimental temperature range is $\Delta T = 300K$. Then χ only varies $1.2 \times 10^{-7} \times 300 = 3.6 \times 10^{-7}$ cm^3/mol, i.e. a change of $\sim 1\%$ from room temperature value (-3.33×10^{-5} cm^3/mol)[105].

upper limit at any finite temperature) can be estimated as:

$$m_{Mn}^{mag} = \frac{\rho s d_{film}}{Mass_{mol}} x N_A (5\mu_B).$$

with ρ the density of GaAs=5.32 g/cm^3, s the sample area, d_{film} the film thickness=180 nm, $Mass_{mol}$ the molar mass of GaAs=144.64 g/mol, N_A the Avogadro number, and μ_B Bohr Magneton=9.27×10^{-21} emu. We then calculated the signals expected from each GaAs substrate and each saturated Mn moment (Table B.2), and compared them with the measured signals collected by the SQUID.

We measured the magnetic moment of all four pieces and the corresponding empty holders except for the 37.3mg sample. A piece of GaAs of 12.1 mg was also measured for comparison. The SQUID measurements are all done at 1.3 T and summarized in Fig. B.5. The temperature dependent term that comes up below 100 K is clearly due to the Mn doped film and comparable to previous measurements in Fig. B.3. However, the signal above T_C is paramagnetic, and varies significantly from run to run and from sample to sample. And the signal is nearly always paramagnetic (positive moment), rather than the diamagnetic moment expected from the GaAs substrate (see horizontal dashed lines in Fig. B.5.) For these reasons, we conclude that there is a rather large, apparently temperature-independent, paramagnetic contribution coming from the sample holder (m_{holder}^{mag}). This is confirmed, for example, from runs using the same holder, with and without the sample. This m_{holder}^{mag} must exist in all the data, and the data that yields a near zero moment simply has the combination $m_{holder}^{mag} + m_{substrate}^{mag}$ just nearly canceling.

We converted the magnetization to volume susceptibility χ by dividing the signal by the film volume and the field. The results of measurements on 37.3 mg sample and 12.7 mg sample are stacked in Fig. B.6 together with the GaAs sample of 12.1 mg. For the Ga$_{1-x}$Mn$_x$As sample of 12.7 mg and the GaAs sample of 12.1 mg, the holder signal is removed and the resulting magnetization contributed only by the sample is converted to volume susceptibility. Take the measurement of the 12.7 mg Ga$_{1-x}$Mn$_x$As sample at 90K
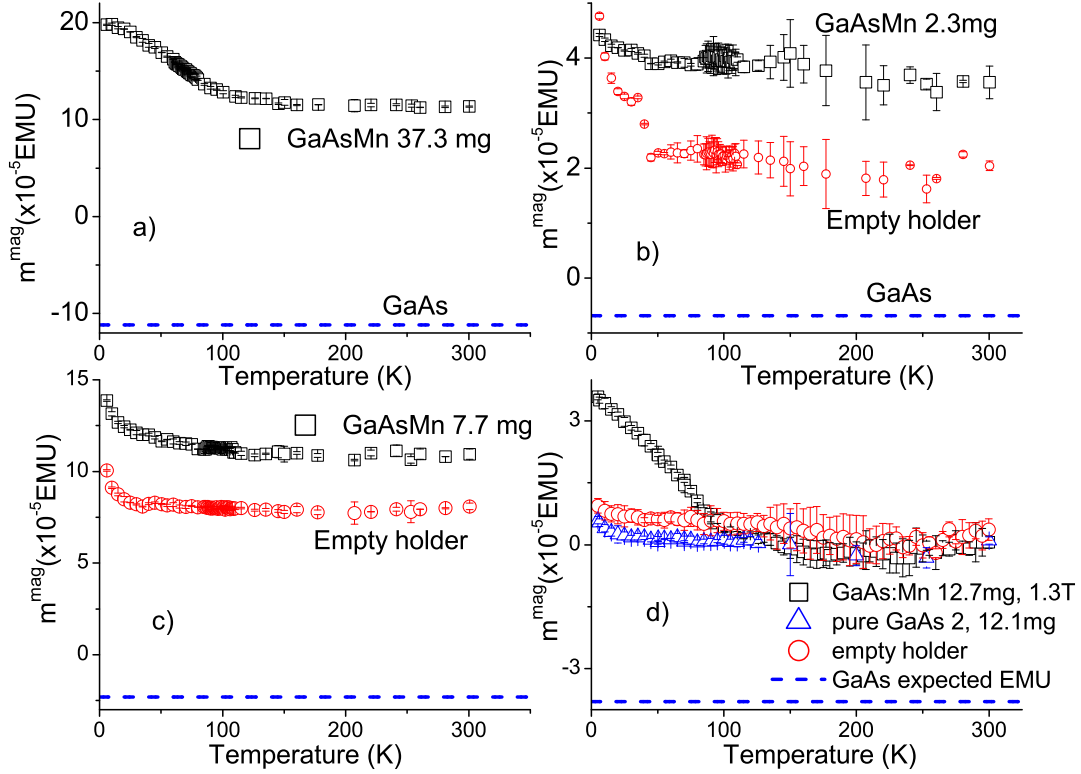
174

Figure B.5: SQUID measurements of various samples at 1.3 T. The open black squares, open red circles, open blue triangles are signals from sample+holder,empty holder, and pure GaAs substrate, respectively, while the blue dashed line is the expected GaAs magnetization at 1.3 T calculated with the susceptibility from Ref. [105].
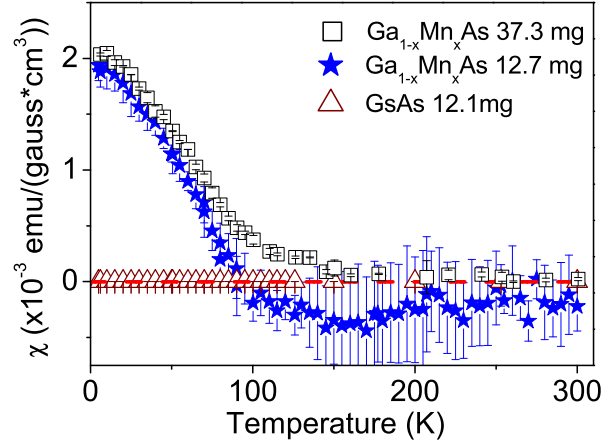
Figure B.6: The signal of the holder is removed, then the magnetization only due to the sample itself is converted into volume susceptibility. The dashed red line indicate the volume susceptibility expected for GaAs.

for an example. The sample signal m_{sample}^{mag} is $(7.425 \pm 0.515) \times 10^{-6}$emu, and the holder signal m_{holder}^{mag} is $(5.82439 \pm 3.62) \times 10^{-6}$ emu. The sample volume V is calculated using the sample mass (12.7 mg), film thickness($d_{film} = 180$ nm) and substrate thickness($d_{sub} = 0.41$ mm), assuming that the density of the Mn doped overlayer is the same as that of the GaAs substrate ($\rho = 5.32$ g/cm^3):

$$
\begin{aligned}
V &= \frac{m}{\rho} \frac{d_{film}}{d_{sub}} \\
&= \frac{0.0127 \text{ g}}{5.32 \text{ g/cm}^3} \frac{0.18 \ \mu\text{m}}{410 \ \mu\text{m}} \\
&= 1.048 \times 10^{-6} \text{ cm}^3
\end{aligned}
$$

The volume susceptibility at 90K in the field of 13000 gauss is calculated as:

$$
\begin{aligned}
\chi &= \frac{m_{sample}^{mag} - m_{holder}^{mag}}{H \times V} \\
&= \frac{7.425 \times 10^{-6} - 5.8243 \times 10^{-6}}{13000 \times (1.048 \times 10^{-6})}
\end{aligned}
$$

176

$$= 1.1749 \times 10^{-4} \text{ emu/(gauss*cm}^3)$$

Note that since there is no holder information for the 37.3 mg sample, it is corrected by removing the nonzero baseline at high temperature to calculate the volume susceptibility (open black squares in Fig. B.6). The volume susceptibility resulting from two samples nearly overlap, confirming the reproducibility of our measurements. Taking the S/N ratio into consideration, we would use the data set measured with 37.3 mg sample to calculate the volume susceptibility of the $Ga_{1-x}Mn_xAs$ film in the β-NMR experiments.

In the ferromagnetic state, since the relation $M = \chi H$ does not hold (due to hysteresis), it is more appropriate to consider simply the magnetization, M in the 1.3 T field-cooled measurement. This is exactly the condition of the β-NMR experiment, so it should be directly comparable. For example, at 30K, the sample signal m_{sample}^{mag} is $(18.50 \pm 0.06) \times 10^{-5}$ emu, and the high temperature baseline m_{base}^{mag} is $(11.25 \pm 0.04) \times 10^{-5}$ emu. Then the magnetization is calculated as:

$$
\begin{aligned}
M &= \frac{m_{sample}^{mag} - m_{base}^{mag}}{V} \\
&= \frac{(18.50 - 11.25) \times 10^{-5}}{3.22 \times 10^{-6}} \\
&= (22.5 \pm 0.2) \text{ emu/cm}^3 \\
&= (22.5 \pm 0.2) \text{ gauss}
\end{aligned}
$$

And the demagnization field is:

$$
\begin{aligned}
H_{demag} &= -NM \\
&= -4\pi M \\
&= -4\pi \times 22.5 \text{ gauss} \\
&= -282.74 \text{ gauss}
\end{aligned}
$$

The corresponding frequency is:

$$
\begin{aligned}
\gamma H_{demag} &= -0.63015 \; \frac{\text{kHz}}{\text{gauss}} \times 4\pi \times 22.5 \; \text{gauss} \\
&= -178.2 \; \text{kHz}
\end{aligned}
$$

As a comparison, the frequency shift at 30 K, observed in the β-NMR experiment, of the broadened resonance in the overlayer is -8.51 kHz with respect to the sharp resonance in GaAs substrate (Fig. 4.7). The demagnetization effect is much larger in this case (Section 4.4.3).

Appendix C

Current Injection
Experimental Setup

To carry out the current injection experiment, a new current injection system was needed to allow the application of electrical current to a sample during a β-NMR run under ultra-high vacuum (UHV) and cryogenic conditions. This requires 1) a new sample holder which enables the application of a current and is compatible with the existing apparatus; 2) a system which allows current injection and does not interfere with the use of the original sample holder when current injection is not required; 3) the careful selection of materials of each part (e.g. UHV compatible, non-magnetic, etc.).

The new system consists of three main components: sample holder, sample clamp and socket (Fig. C.1). The sample holder is made of Oxgen-free copper, because it is non magnetic, UHV compatible and of high thermal conductivity. Both the clamp and the socket are used to help make the electric connection but insulate the current from the grounded copper holder. Therefore DuPont Vespel^{TM} SP–1 was selected for its low outgassing, cryogenic compatibility, low ware for long lifetime, and similar thermal expansion coefficient to copper (50 μm/m/K) for Vespel). The current is carried by contact springs made of 0.01 inch thick beryllium copper (BeCu) strips, which is of high strength, good electrical conductivity, UHV compatible, springy and, more importantly, non magnetic.

The new sample holder is adapted from the original sample holder (Fig. C.2). The top part is unchanged, and compatible with the existing apparatus. The flat surface works as a key to align the sample when the sample is loaded into the cryostat. The sample (usually glued to a sapphire plate)
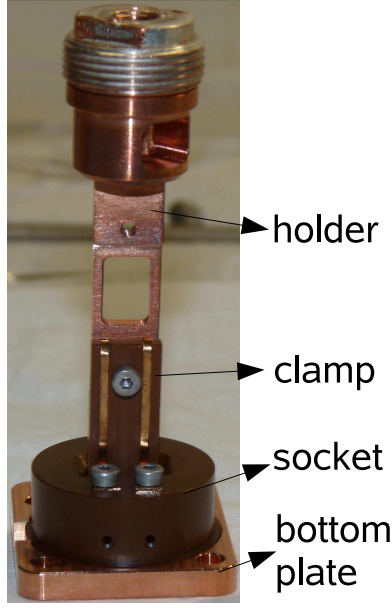
Figure C.1: Three main components of the current injection system: sample holder, sample clamp, and socket.

is held in a recess with a window behind to minimize the thermal mass and also β electron absorption. Compared to the original holder, the recess is extended vertically to allow space for electrical contacts. There is a lip and a recess at the bottom for the sample clamp (attached with a M2 screw) which is designed to provide clamping force on the sample and make electric connection when screwed down to the holder. Two metallic BeCu springs are held in the recesses on the clamp to carry current to the sample (Fig. C.3 Left panel). The springs are wrapped around the clamp and make electrical contact with both the sample and the socket below.

The socket assembly engages the holder assembly with the clamp when they are inserted to make the electric connection. Two BeCu strips, carrying current to the springs on the clamp, are held in the socket with screws from both top and bottom. The strips are connected to a current source through the strip bottom by lead wires. The through screw holes are vented from the side of the socket to maintain the UHV environment required by the β-NMR
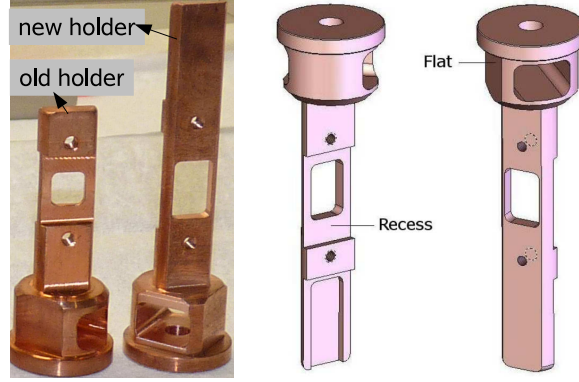
Figure C.2: Left: original and new sample holders. Right: Details of new sample holder

experiment. Two additional holes opposite the BeCu strips are reserved for the rf antenna, a diagnostic device for the spectrometer. The socket is attached by a bottom copper plate to the copper sample enclosure. A small cut-away in both the socket and the plate ensures the correct orientation of the socket.

Fig. C.4 shows the assembled current injection system with a sample in the cryostat. The limited space inside the copper housing constrains the dimension of the current injection system. The spacing of the coils determines the maximum width of the sample holder and the clamp, less than 9 mm. The height of the socket is limited by the position of the Helmholtz coil. However, the socket height is kept even lower to minimize the thermal load on the cryostat. All screws used in this system are titanium M2 screws which are non magnetic.

The two lead wires to the socket are Kapton insulated UHV copper leads (KAP3) from MDC that begin at SHV feedthroughs on the cryostat. These existing feedthroughs were then adapted to standard RCA bananaplug connectors. The total resistance of twol lead wires including the banadaplug is 1.3 Ω at room temperature. The 0937 current source is made at TRIUMF. The range of the current source is (-500 mA, +500 mA) with the resolution of 1 mA.
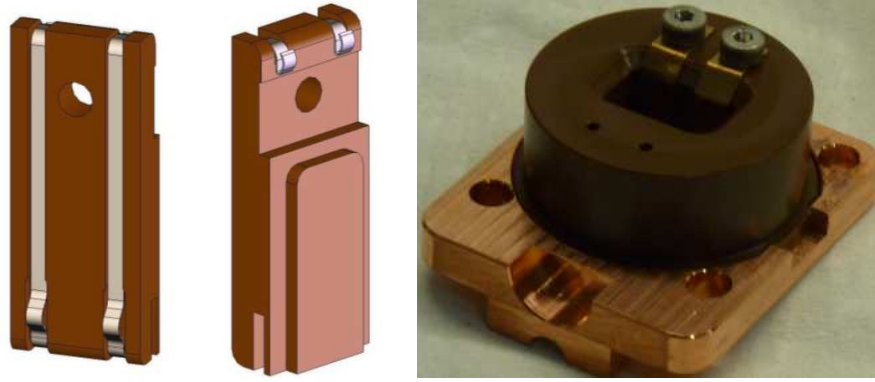
Figure C.3: Left: the front and back side of the vespel clamp with two BeCu springs. Right: the vespel socket sitting on the bottom plate of the Copper housing. Two BeCu strips are bolted to the vespel socket with titanium M2 screws.
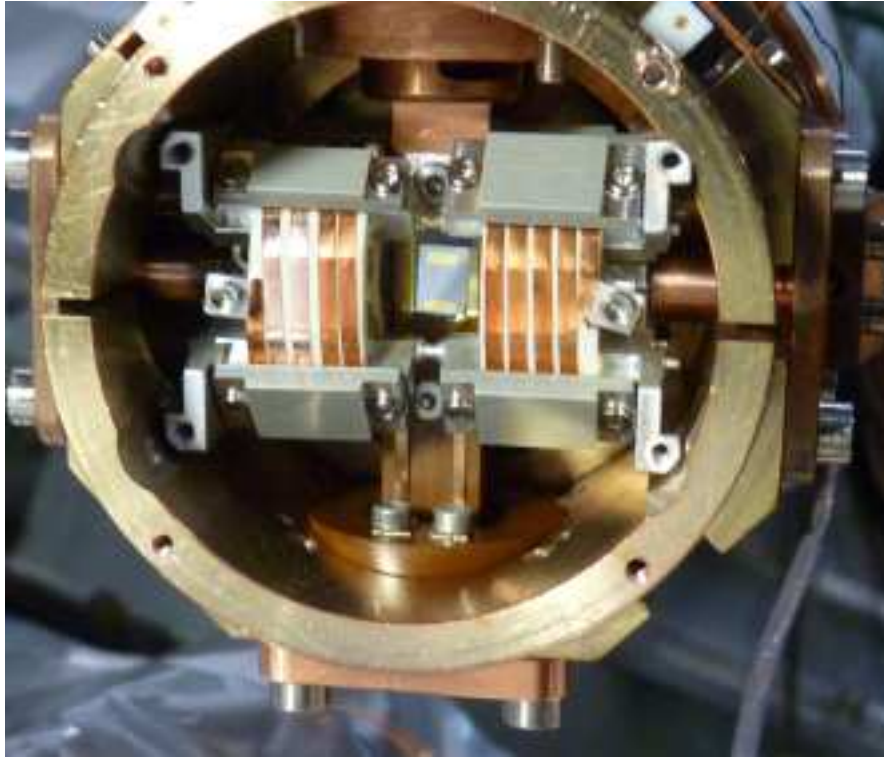

Figure C.4: The assembled current injection system with a sample in the cryostat.

Appendix D

Sample Preparation for Current Injection Experiment

This section describes how the samples were prepared for the in-situ current injection experiments detailed in Chapter 5. Gold (Au) pads for making electrical contact were thermally deposited on both sides of the Au/Fe/nGaAs sample by the thermal evaporator in the cleanroom at AMPEL, UBC. The evaporator is capable of depositing 4 types of thin films once the sample is loaded inside the chamber. Fig. D.1 shows the geometry of the contacts on the front (left panel) and back (right panel) side. All contacts were deposited at room temperature in high vacuum ($\sim 5 \times 10^{-6}$ Torr).

Inside the thermal evaporator, the sample was arranged upside down to face the Au source below to deposit the contacts on the front side. In order to protect the thin MBE heterostructure, we made a special holder with a set of
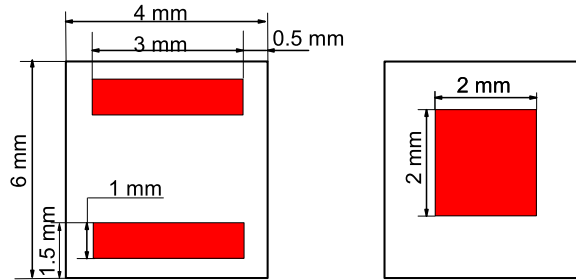

Figure D.1: The geometry of gold contacts on the front (left) and back (right) side of Au/Fe/nGaAs sample.
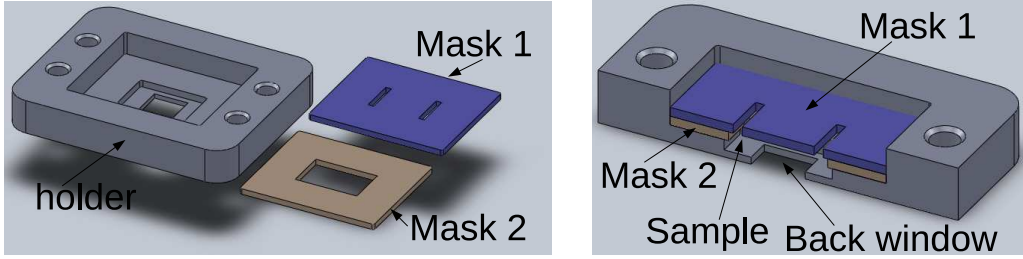
Figure D.2: Left: the sample holder and masks for the termal evaporation. Right: The section view of the assembled thermal evaporator sample holder.

masks(Fig. D.2) under the help of P. Dosanjh from UBC. When it is loaded into the evaporator, the front surface is supported and protected by Mask 2 only touching the sample edges and leaving the center area untouched (Fig. D.2). On the front side of the sample is the 20 ML thick Au layer to protect the Fe layer from oxidation. The Au pads were deposited directly on the MBE Au layer and had a thickness ∼194 nm estimated by a quartz crystal thickness monitor.

There is a window on the backside of the evaporation sample holder, which is used as the mask when evaporating the Au contacts on the *backside* of the sample (Fig. D.2). Before the backside Au contact is made, a very thin layer of Ti (∼ 3 nm) was deposited. Because Au does not stick to GaAs very well, a direct deposition of Au onto GaAs would not result a long-lasting Au layer. Ti helps to smooth the unpolished GaAs backside, and improves the contact bond to GaAs[193]. Right after the Ti layer was evaporated, the back Au contact (∼195 nm) was deposited without breaking the evaporator chamber vacuum.

Between the copper β-NMR sample holder and the Au/Fe/nGaAs sample, there is a $8 \times 15 \times 0.5$ mm^3 sapphire plate (one-side polished) to insulate the electrically biased sample from the conductive sample holder and connect the sample to the current source. To conduct current to the sample, a layer of gold (∼195 nm) is also thermally evaporated on the polished side of the sapphire plate. A thin layer of Ti (∼3 nm) was deposited prior to the Au layer to help gold better bond to the sapphire. The pattern of the
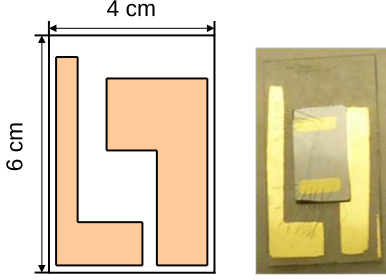
Figure D.3: Left: the geometry of the gold contacts on the sapphire plate. Right: The sample assembled on the sapphire plate.

gold contacts pads on the sapphire is shown in left panel of Fig. D.3. The right pad is bonded to the back contact of the sample with UHV compatible silver paint (cured at room temperature), and the left pad is connected to the sample front pads via fine gold wires (0.001" in diameter). The fine gold wires were installed by a gold wire bonder in the lab of J. Folk from UBC with the assistance of M. Studer. The BeCu springs make contact with the gold pads when the sample is clamped down to the holder, making electrical contact. Therefore a small gap at the bottom of the gold pattern is required so that the gold will not be short-circuited by contacting with the copper sample holder. A picture of the sample assembled on the sapphire plate is shown in the right panel in Fig.D.3.